

Momentum and scalar transport in vegetated shear flows

by

Marco A. Ghisalberti

Submitted to the Department of Civil and Environmental Engineering
in partial fulfillment of the requirements for the degree of

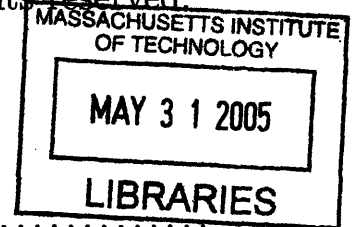
Doctor of Philosophy in the field of Environmental Fluid Mechanics


at the

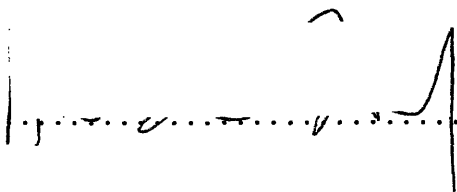
MASSACHUSETTS INSTITUTE OF TECHNOLOGY

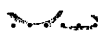
June 2005

© Massachusetts Institute of Technology 2005. All rights reserved.



Author 
Department of Civil and Environmental Engineering
March 28, 2005

Certified by 
Heidi M. Nepf
Professor of Civil and Environmental Engineering
Thesis Supervisor

Accepted by 
Andrew J. Whittle
Chairman, Departmental Committee on Graduate Studies

ARCHIVES



Momentum and scalar transport in vegetated shear flows

by

Marco A. Ghisalberti

Submitted to the Department of Civil and Environmental Engineering
on March 28, 2005, in partial fulfillment of the
requirements for the degree of
Doctor of Philosophy in the field of Environmental Fluid Mechanics

Abstract

Environmental aquatic flows are seldom free of vegetative influence. However, the impact of submerged vegetation on the hydrodynamics and mixing processes in aquatic flows remains poorly understood. In this thesis, I present the results of laboratory experiments that describe the salient hydrodynamic and transport features of vegetated flows. Flume experiments were conducted with dowels and buoyant polyethylene strips used to mimic rigid canopies and flexible seagrass meadows respectively.

Although traditionally treated as rough boundary layers, vegetated shear flows more closely resemble mixing layers. Specifically, vertical velocity profiles contain an inflection point, yielding the flow unstable to a street of Kelvin-Helmholtz vortices. These vortices dominate transport through the shear layer, such that the rate of mixing of both mass and momentum is shown to scale upon their size and rotational speed. However, mass is mixed approximately twice as rapidly as momentum. The spread of a scalar plume is shown to be a function of the number of vortex cycles experienced by the plume, irrespective of the canopy characteristics or flow speed.

In contrast to mixing layers, the vortices in a vegetated shear layer grow only to a finite size, often not penetrating fully to the bed. This separates the canopy into an upper zone with rapid, vortex-driven transport and a lower zone where mixing occurs on the much smaller scale of the stem wakes. Vortex growth is shown to cease once the shear production of vortical energy is balanced by the drag dissipation of that energy by the canopy. The mixing length of momentum scales upon the final vortex size, allowing closure of a one-dimensional Reynolds-averaged Navier-Stokes model.

Finally, canopy flexibility has a significant impact on the hydrodynamics of vegetated flows. The oscillating velocity field associated with the vortex street drives a coherent waving of the canopy, whose geometry changes rapidly over time. Using the height of a waving plant as an indicator of phase in the vortex cycle, synchronized velocity records show that the turbulence structure at the top of the canopy consists of a strong sweep at the front of the vortex, followed by a weak ejection at its rear.

Thesis Supervisor: Heidi M. Nepf

Title: Professor of Civil and Environmental Engineering

Acknowledgments

Firstly, I would like to thank The University of Western Australia and the National Science Foundation for their financial support of this research.

Secondly, many thanks must go to the people who worked with me in the laboratory. Through the MIT UROP program, the assistance of **Paula Deardon** and **Constantinos Tsoucalas** was invaluable. **Peter Israelsson** helped me immensely by configuring his particle tracking model for my use. **Leah Kaplan** deserves special thanks for her selflessness in helping me with the most mundane of tasks. Outside of my research, my friends in the Parsons Lab have each made my time here all the more enjoyable and memorable.

Lastly, I would like to thank members of my thesis committee, **Eric Adams** and **Ole Madsen**, for their remarkable insight into my work. For their equipment tutorials, advice, questions and musings, I am also grateful to fellow members (past and present) of the **Nepf research group**, namely Chin Wu, Paul Fricker, Hrund Andradottir, Laura DePaoli, Brian White, Molly Palmer, Anne Lightbody, Yukie Tanino and Enda Murphy. Finally, and foremost, my thesis advisor **Heidi Nepf** deserves special thanks for her boundless generosity in sharing her expertise and time. Her enthusiasm for the acquisition and sharing of knowledge has made my time at MIT a truly outstanding one.

Contents

1	Introduction	15
1.1	Thesis structure	17
2	The limited growth of vegetated shear layers	19
2.1	Introduction	19
2.2	Shear layer hydrodynamics	22
2.3	Experimental methods	25
2.4	Experimental results	28
2.4.1	Basic properties of velocity profiles	28
2.4.2	Vertical profiles of eddy viscosity and mixing length	31
2.4.3	Drag coefficient of a submerged array	35
2.4.4	Behavior of the stability parameter	38
2.5	Numerical model of vegetated shear flow	39
2.5.1	Comparison between the model and experimental data	42
2.5.2	Extension of the model to field conditions	44
2.6	Conclusion	45
3	Mass transport in vegetated shear flows	47
3.1	Introduction	47
3.2	Methodology	49
3.2.1	Image analysis	51
3.2.2	Experiments	54
3.3	Results	56

3.3.1	Two-box model	60
3.3.2	Flux-gradient model	64
3.3.3	Similarity of plume behavior	67
3.4	Particle tracking model	68
3.5	Conclusion	71
4	The impact of vegetation on transport in open channels	75
4.1	Vertical profiles of velocity and diffusivity	75
4.2	Longitudinal dispersion	78
4.2.1	Unvegetated channels	78
4.2.2	Vegetated channels	79
4.3	Conclusion	84
5	The effect of plant flexibility on vertical transport	85
5.1	Experimental methods	85
5.2	Mixing layer analogy	89
5.3	Correlation between the flow field and plant motion	92
5.4	Conclusion	95
A	Profiles of mean velocity and Reynolds stress	99
B	The drag coefficient of submerged arrays as compared to individual cylinders	103
C	Extension of hydrodynamic model outside the experimental range	105
D	Behavior of the Strouhal number along the canopy	107
E	Concentration profiles	109

List of Figures

1-1	Time series of streamwise velocity and vertical momentum transport taken at the top of a flexible experimental canopy.	16
2-1	Mean velocity profile of a flow with submerged, flexible vegetation. . .	21
2-2	Side view of the laboratory flume.	26
2-3	Vertical profiles of U and $\overline{u'w'}$ for Runs H and J.	29
2-4	The correlation between the normalized shear ($\Delta U/U_h$) and the dimensionless plant density (ad).	30
2-5	Vertical profiles of eddy viscosity (ν_T) throughout the shear layers. . .	32
2-6	Vertical profiles of mixing length (l) throughout the shear layers. . . .	33
2-7	Vertical profiles of η , the ratio of the observed drag coefficient to the theoretical value predicted by considering array density and Reynolds number effects.	37
2-8	The invariability of the stability parameter Ω	39
2-9	A comparison between observed and predicted profiles of mean velocity for Runs B, C and H.	42
2-10	The comparison between observed values of ΔU and those predicted by the model.	43
2-11	Demonstration of model sensitivity to the chosen value of U_1	44
3-1	Side view of dye injection in the flume.	49
3-2	Plan view of the calibration used to determine the validity of the Beer-Lambert Law in these experiments.	52

3-3	The relationship observed between absorbance ($A = \log(I_0/I)$) and bC for three dye solutions in the triangular tank.	53
3-4	Sample evaluation of an instantaneous concentration profile in Run E.	56
3-5	Steady-state concentration profiles and velocity profile of Run I.	57
3-6	Evidence of the lateral heterogeneity in vegetated shear flows.	58
3-7	The importance of Kelvin-Helmholtz vortices in vertical transport in vegetated shear flows.	59
3-8	Definitive diagram of the two-box and flux-gradient models used to describe vertical transport.	60
3-9	The exponential decay of normalized in-canopy concentration (C^*) over distance.	63
3-10	The direct proportionality between the exchange velocity, k , and the total shear, ΔU	64
3-11	The collapse of D_{tz} , when normalized by $\Delta U t_{ml}$, across the range of plant densities and the vertical profile of the turbulent Schmidt number ($Sc_t = \nu_{tz}/D_{tz}$) in the shear layer.	66
3-12	The collapse of the decay curves of in-canopy concentration when plotted against a dimensionless distance, \hat{X}	68
3-13	The longitudinal variation of normalized best-fit diffusivity, γ	70
3-14	The good agreement between the experimental concentration profiles of Run E and those predicted by the LPTM.	72
4-1	Comparison of the profiles of velocity and vertical diffusivity in the two archetypal channels.	77
4-2	The two limiting regimes of longitudinal dispersion in vegetated shear flows.	79
4-3	The values of the dispersion coefficient (K_x), calculated by considering vertical shear only, as a function of ψ for the eleven experimental runs.	81
4-4	The behavior of $K_x^*(\psi)$ and $K_x^{**}(\psi)$ in Run H.	82
5-1	The flexible model vegetation of this study.	86

5-2	Profiles of mean velocity and Reynolds stress in a mixing layer and in shear flows over a rigid canopy, a still, flexible canopy and a waving, flexible canopy.	90
5-3	The oscillation of the velocity profile and plant height during the <i>mon-ami</i> cycle.	94
5-4	The fluctuation of the two-dimensional flow field as a function of phase bin.	96
A-1	Vertical profiles of mean velocity with rigid canopies.	100
A-2	Vertical profiles of Reynolds stress with rigid canopies.	100
A-3	Vertical profiles of mean velocity with flexible canopies.	101
A-4	Vertical profiles of Reynolds stress with flexible canopies.	101
B-1	The comparison between the vertical profile of η in the experimental arrays and those for a single cylinder with $h/d = 19$, a single cylinder with $h/d = 2$ and the downstream cylinder of a pair in tandem with $\Delta S = 5d$	104
C-1	The power dependence of $\Delta U/U_h$ on ad	106
D-1	The decrease in the Strouhal number and vortex frequency along the flexible canopy.	108
E-1	Vertical profiles of C^* at measurement location 1.	110
E-2	Vertical profiles of C^* at measurement location 2.	110
E-3	Vertical profiles of C^* at measurement location 3.	111
E-4	Vertical profiles of C^* at measurement location 4.	111
E-5	Vertical profiles of C^* at measurement location 5.	112
E-6	Vertical profiles of C^* at measurement location 6.	112

List of Tables

2.1	Summary of experimental conditions and vegetated shear flow parameters.	27
2.2	Summary of modeling equations in Zone 1.	40
3.1	Summary of experimental conditions and vegetated shear flow parameters.	50
5.1	Key parameters of the six experimental flows with flexible vegetation.	88
A.1	Values of ΔU and U_1 for all runs with rigid and flexible canopies. . .	99

Chapter 1

Introduction

Environmental aquatic flows are seldom free of vegetative influence. From coastal sea-grass meadows and kelp forests to river grasses to watermilfoils, pondweeds and worts in lakes and wetlands, submerged vegetation is a ubiquitous presence in many flows of interest. Therefore, to begin to predict flow conveyance in vegetated channels, wave attenuation and shore protection by vegetated coastal beds or flow patterns in lakes and wetlands, one must first appreciate the hydrodynamic impact of submerged vegetation. Furthermore, submerged vegetation plays an important role in the chemistry and biology of aquatic systems. Through the direct uptake of nutrients and heavy metals (Kadlec and Knight [31]), the capture of suspended sediment (Palmer *et al.* [49]) and the production of oxygen, submerged vegetation can dramatically improve water quality. Submerged canopies also provide habitats for macrofauna (Edgar [15]) and settlement sites for larvae (Grizzle *et al.* [27]). Despite the impact of vegetation on both the hydrodynamics and ecological function of aquatic systems, the structure of vegetated aquatic flows is not well understood. In this thesis, I describe the salient hydrodynamic features of flows with submerged vegetation and their impact on mass transport.

The underlying theme of this thesis is that flows with submerged vegetation should be patterned upon a mixing layer, rather than a rough boundary layer (as first presented by Raupach *et al.* [52]). The inflection point in velocity profiles of both mixing layers and these vegetated flows yields them inherently unstable to the Kelvin-

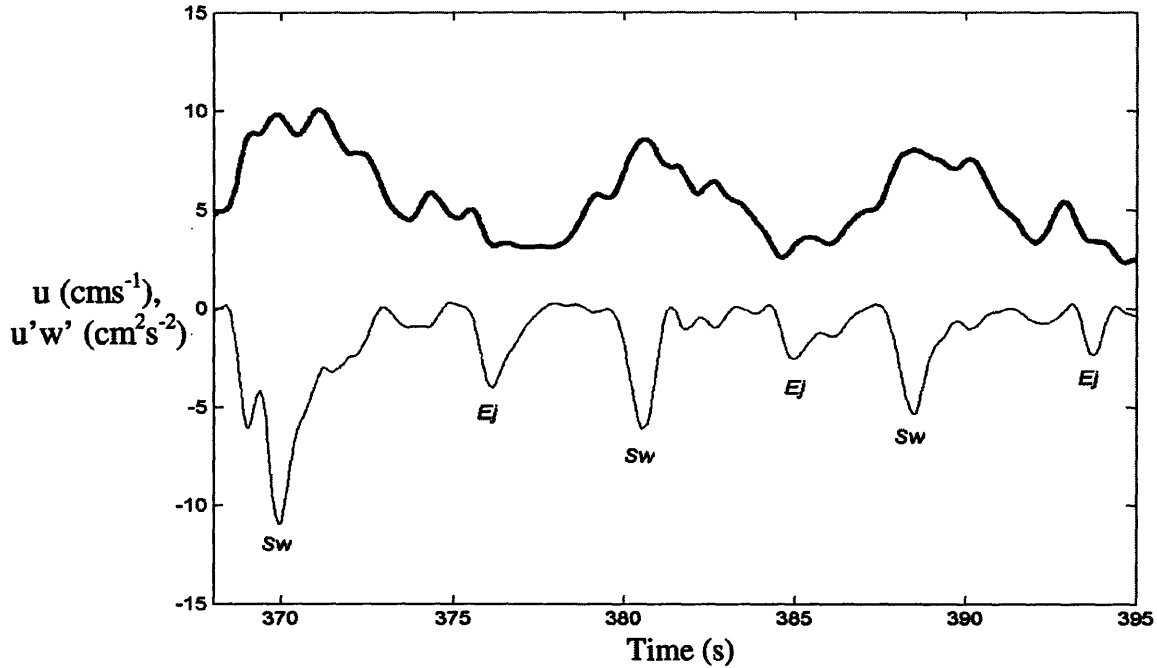


Figure 1-1: Time series of streamwise velocity (u , thick line) and vertical momentum transport ($u'w'$, thin line, where w is vertical velocity, positive upward) taken at the top of a flexible experimental canopy (Ghisalberti and Nepf [24]). Both signals oscillate at the frequency of vortex passage, approximately 0.11 Hz. In the time series of momentum transport, a strong sweep (Sw, $u' > 0, w' < 0$) is followed by a weak ejection (Ej, $u' < 0, w' > 0$).

Helmholtz vortex instability (see, e.g., Brown and Roshko [4], Ikeda and Kanazawa [29]). The vortex street generated in flows with submerged vegetation results in strongly periodic flow and transport. This is demonstrated in Figure 1-1 (taken from Ghisalberti and Nepf [24]), which shows streamwise velocity and vertical momentum transport at the top of a model canopy oscillating at the vortex passage frequency of approximately 0.11 Hz. Vertical momentum transport is highly structured in these flows, with a strong sweep into the canopy preceding a weak ejection. In this thesis, I show that the rates of vertical transport of both momentum and scalars in vegetated shear flows are directly dependent upon the size and rotational speed of these coherent vortices. The oscillatory flow generated by the vortices also drives the *monami*, a progressive, coherent waving of flexible aquatic canopies in strong currents. The terrestrial equivalent of this waving, the *honami*, is most commonly observed as waving

fields of wheat.

Flows with submerged vegetation are just one example of obstructed shear flows. Other examples include environmental flows (both aquatic and aerodynamic) over porous media, boulder beds, urban landscapes and agricultural and forest canopies, as well as industrial flows such as those through heat exchangers and wind farms. In particular, an understanding of the turbulent exchange of heat, mass and momentum between terrestrial canopies and their surroundings is fundamental in the description of global carbon dioxide and hydrologic cycles, and has attracted much scientific attention (see, for example, the excellent summary by Finnigan [16]). The framework developed in this thesis is expected to be qualitatively applicable to the suite of obstructed shear flows.

1.1 Thesis structure

This thesis is presented as a series of distinct chapters, some of which have been submitted for publication, followed by appendices that contain auxiliary data. Chapter 2 is a paper published as Ghisalberti and Nepf [23]. It presents a description of the stability of obstructed shear layers, which explains the cessation of shear layer growth, and describes the applicability of a constant mixing length model for Reynolds stress closure. This closure is then used in a one-dimensional Reynolds-averaged Navier-Stokes model to predict the velocity profiles of the experimental flows. Data from this chapter also appear in an article submitted to the *Journal of Fluid Mechanics* as H. Nepf, M. Ghisalberti and B. White, “A scale constraint for shear-layers generated in canopies and other obstructed flow”. Chapter 3 is a paper submitted to *Environmental Fluid Mechanics*. In this chapter, a novel experimental technique is used to evaluate the spread of scalar plumes in vegetated shear layers in the laboratory. The rate of scalar transport is characterized by the size and rotational velocity of the vortices and is shown to be much greater than the rate of momentum transport evaluated in Chapter 2. The spread of a scalar plume is shown to be almost solely a function of the number of vortex cycles experienced by the plume. In Chap-

ter 4, some simple scaling arguments are used to characterize the theoretical rate of longitudinal dispersion in vegetated shear flows. By contrasting vegetated channels with their unvegetated counterparts, this chapter also highlights the impact of submerged vegetation on mixing processes. Chapter 5 explores the influence of plant flexibility, specifically the *monami* phenomenon, on the hydrodynamics described in previous chapters. An emphasis is placed upon description of the vortex structure and the strongly oscillatory nature of obstructed shear flows, which in turn drives the oscillatory motion of the plants.

Chapter 2

The limited growth of vegetated shear layers¹

Abstract

In contrast to free shear layers, which grow continuously downstream, shear layers generated by submerged vegetation grow only to a finite thickness. Because these shear layers are characterized by coherent vortex structures and rapid vertical mixing, their thickness controls exchange between the vegetation and the overlying water. Experiments conducted in a laboratory flume show that the growth of these obstructed shear layers is arrested once the production of shear-layer-scale turbulent kinetic energy (SKE) is balanced by dissipation of SKE within the canopy. This equilibrium condition, along with a mixing length closure scheme, was used in a one-dimensional numerical model to predict the mean velocity profiles of the experimental shear layers. The agreement between model and experiment is very good, but field application of the model is limited by a lack of description of the drag coefficient in a submerged canopy.

2.1 Introduction

Aquatic macrophyte communities, which include the plants as well as the plankton, benthic flora and epiphytic organisms that live among them, depend on a supply of nutrients from the surrounding water column (e.g., Short *et al.* [58]; Taylor *et al.* [61]). In turn, these communities play an important role in maintaining the water quality

¹This chapter has been published as Ghisalberti and Nepf [23].

of coastal regions by filtering nutrients from the water column (Short and Short [57]). Submerged macrophytes also provide an important habitat for invertebrate larvae (e.g., Phillips and Menez [50]). Settlement and recruitment of larvae to this habitat depend not only on organism behavior but also on hydrodynamic processes at many scales in and around the canopy (as reviewed in Butman [7], also in Eckman [14]; Duggins *et al.* [12]; Gambi *et al.* [21]; Grizzle *et al.* [27]). The drag exerted by the vegetation promotes sediment accumulation by reducing the near-bed stress (Lopez and Garcia [38]) and this is also expected to strongly influence the vertical transport of chemicals released by the sediment. This paper presents predictive models for key aspects of the canopy-scale hydrodynamics, described below.

The dominant hydrodynamic feature of flow with submerged macrophytes is a region of strong shear at the top of the canopy, created by the vertical discontinuity of the drag (Gambi *et al.* [21]; Nepf and Vivoni [44]). Figure 2-1 shows the vertical profile of mean velocity for a flow with submerged, flexible vegetation (data taken from Ghisalberti and Nepf [24]). The shear layer contains an inflection point, making it dynamically analogous to a mixing layer, with vertical transport through the layer dominated by coherent, shear-scale, Kelvin-Helmholtz (KH) vortices (Raupach *et al.* [52]; Ikeda and Kanazawa [29]; Ghisalberti and Nepf [24]). These vortices therefore control the exchange of nutrients, larvae and sediment between a submerged canopy and the overlying water. In an unobstructed mixing layer, the vortices grow continually downstream (e.g., Brown and Roshko [4]). In a vegetated mixing layer, however, the vortices grow to a finite size a short distance from their initiation (Ghisalberti and Nepf [24]). In many instances (as in Figure 2-1), the final vortex size, and the region of rapid exchange it defines, extends to neither the water surface nor the bed. This segregates the canopy into an upper region of rapid exchange and a lower region with more limited water renewal (Nepf and Vivoni [44]).

The goal of this paper is to explain the dynamic equilibrium that arrests the growth of vortices formed in a vegetated shear layer. Once established, this equilibrium condition can be used, with simple turbulence closure, to predict the vertical velocity profile within and above submerged canopies. Previous studies have shown

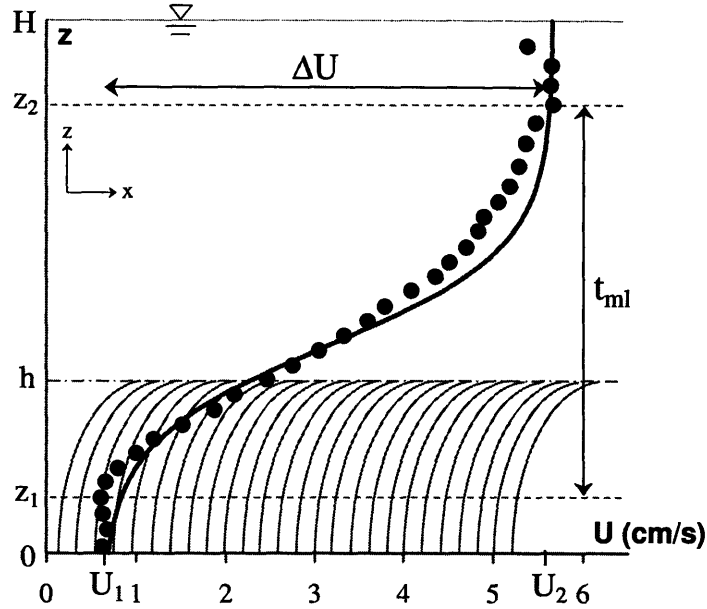


Figure 2-1: Mean velocity profile of a flow with submerged, flexible vegetation of height h (data taken from Ghisalberti and Nepf [24]). The shear layer is defined by the limits z_1 (where the mean velocity is U_1) and z_2 (U_2), and has a thickness t_{ml} . The total shear across the layer is ΔU ($= U_2 - U_1$). The velocity profile contains an inflection point near the top of the vegetation. Despite its asymmetry, the profile qualitatively resembles the hyperbolic tangent profile (solid line) of a mixing layer.

that the velocity profile above a vegetated boundary follows a logarithmic form, with velocity scale (u_*) defined by the turbulent stress at the top of the canopy and roughness scale (z_o) defined by canopy morphology (e.g., Thom [62]; Shi *et al.* [56]; Nepf and Vivoni [44]). However, the logarithmic form begins a full canopy height (h) above the actual top of the canopy (i.e. at $z = 2h$). The velocity profile within the canopy is often assumed to be uniform, resulting from a balance of vegetative drag and hydraulic gradient. The in-canopy and above-canopy profiles are then matched using semi-empirical relations (e.g., Kouwen *et al.* [35]; Kouwen and Unny [34]). Numerical models that use turbulence closure schemes in which the canopy elements are both a sink of mean flow energy and a source of turbulent energy have also been employed to predict velocity profiles in vegetated flows (e.g., Burke and Stolzenbach [6]; Lopez and Garcia [39]; Neary [42]). These models, however, do not predict the cessation of shear layer growth.

2.2 Shear layer hydrodynamics

This paper presents a one-dimensional approximation to a three-dimensional flow. The fully-developed mean flow is assumed to be steady, parallel and uniform in x and y (with coordinate directions defined in Figure 2-1). Using the standard Reynolds decomposition (i.e. $u_i = U_i + u'_i$) and an overbar to denote temporal averaging, the streamwise momentum equation takes the form

$$gS = \frac{\partial \overline{u'w'}}{\partial z} + \frac{1}{2}C_D a U^2, \quad (2.1)$$

where a represents the frontal area of the vegetation per unit volume, C_D the drag coefficient of the canopy and S the surface slope ($= -dH/dx$). We note that vegetated shear flow is horizontally inhomogeneous at several scales (see, e.g., Finnigan [16]), but in this analysis the inhomogeneity is removed by spatial averaging. Specifically, all velocity statistics presented in this paper, including those in (2.1), represent averages over the horizontal plane of local temporal means. In (2.1), we assume that the canopy is sufficiently dense that bed drag is negligible in comparison to canopy drag and the ‘dispersive flux’ (which arises from spatial averaging) is negligible in comparison to the turbulent flux (see, e.g., Brunet *et al.* [5]).

There are two dominant turbulence scales in the flow, the shear (KH vortex) scale and the wake-scale. The turbulent kinetic energy budget can be separated into these two distinct eddy scales, such that the canopy acts as a sink of shear-scale turbulent energy but as a source of wake-scale turbulent energy. As the KH vortices dominate vertical transport and govern shear layer growth, only the budget for shear-scale turbulent kinetic energy (SKE) will be considered here. Following Shaw and Seginer [55], the budget for SKE in a vegetated shear layer can be written as

$$\frac{D\overline{k_s}}{Dt} = \underbrace{-\overline{u'w'}}_{(I)} \frac{\partial U}{\partial z} - \underbrace{\frac{\partial \overline{w'k_s}}{\partial z}}_{(II)} - \underbrace{\frac{1}{\rho} \frac{\partial \overline{w'p'}}{\partial z}}_{(III)} - \underbrace{\widetilde{W}}_{(IV)} - \underbrace{\varepsilon_s}_{(V)} \quad (2.2)$$

where ρ is the fluid density, p the pressure and k_s the instantaneous SKE. The terms

on the right-hand side of (2.2) are shear production (I), turbulent transport of SKE (II), pressure transport (III), dissipation by canopy drag (IV) and viscous dissipation of SKE (V). The canopy dissipation, \widetilde{W} , represents the conversion of shear-scale turbulence into wake-scale eddies by the canopy elements. Similarly to Finnigan [16],

$$\widetilde{W} \approx \frac{1}{2} C_D a U \left(2\overline{u'^2} + \overline{v'^2} \right), \quad (2.3)$$

where here it is expected that, because of cylinder geometry, the dissipation of horizontal turbulent motions by the canopy will be much more pronounced than that of vertical turbulent motions. We assume that there is no export of SKE outside the shear layer. This assumption is supported by velocity spectra, which exhibit a clear peak at the vortex frequency inside the shear layer (Ghisalberti and Nepf [24]), but not outside. If the pressure transport term in (2.2) is assumed to be due predominantly to shear-scale pressure fields (as in Zhuang and Amiro [69]), then integration of (2.2) between the lower and upper limits of the shear layer (z_1 and z_2 , respectively, as shown in Figure 2-1) eliminates the transport terms. Furthermore, we expect that drag dissipation of the shear-scale structures will dominate viscous dissipation (see, e.g., Wilson [68]). Therefore, for a fully-developed vegetated shear layer ($D\overline{k_s}/Dt = 0$),

$$\int_{z_1}^{z_2} -\overline{u'w'} \frac{\partial U}{\partial z} dz = \int_{z_1}^h \frac{1}{2} C_D a U \left(2\overline{u'^2} + \overline{v'^2} \right) dz, \quad (2.4)$$

where h is the canopy height. We postulate that the growth of vegetated shear layers ceases once SKE production is countered exactly by canopy drag dissipation within the shear layer, much as bottom friction impedes the growth of shallow, horizontal shear layers (see, e.g., Chu and Babarutsi [10]). We prove this using experimental observations.

The integral conservation of SKE described in (2.4) can be simplified with the assumption of an appropriate eddy viscosity, ν_T . As the length scale of vertical transport (i.e. the vortex scale) is not significantly smaller than the distance over which the curvature of the mean shear changes appreciably, a flux-gradient model is

not strictly valid (Corrsin [11]). However, many turbulent transport problems violate this condition, yet are modeled successfully with an eddy viscosity. Therefore, the assumption of an eddy viscosity was deemed reasonable, if not strictly fundamentally valid. The eddy viscosity can be regarded as the product of a vertical turbulent length scale (which will scale upon the thickness of the shear layer, t_{ml}) and a vertical turbulent velocity (which will scale upon the total shear, ΔU). Although the turbulent length scale is expected to be constant throughout the shear layer, the turbulent velocity is not; the vortices create much stronger vertical velocity fluctuations along their centerline than at their edges. Thus, ν_T will be maximized at the vortex center, in the middle of the shear layer. So, we may define

$$\nu_T = \frac{-\overline{u'w'}}{\partial U / \partial z} = C_1 \Delta U t_{ml} f(z^*), \quad (2.5)$$

where C_1 is a constant and $z^* = ((z - z_1) / t_{ml})$ is the fractional distance above the shear layer bottom. The shape function $f(z^*)$ is expected to peak in the middle of the shear layer, at $z^* = 0.5$.

Within shear layers created by model aquatic vegetation, the vertical profile of $-\overline{u'w'} / (2\overline{u'^2} + \overline{v'^2})$ is similar across a wide range of canopy conditions (data taken from Dunn *et al.* [13], $ad = 0.002 - 0.016$). This ratio increases from zero at $z^* = 0$ to a maximum at the top of the canopy, $z^* = (h - z_1) / t_{ml}$ (as also shown in Nepf and Vivoni [44] and by our own unpublished data). Note that the ratio $(h - z_1) / t_{ml}$ represents the fraction of the shear layer that lies within the canopy and will henceforth be denoted by α . If we assume that the vertical profile of $-\overline{u'w'} / (2\overline{u'^2} + \overline{v'^2})$ has the same form as $f(z^*)$ but peaks at $z^* = \alpha$ rather than $z^* = 0.5$, then within the canopy

$$-\frac{\overline{u'w'}}{2\overline{u'^2} + \overline{v'^2}} = \frac{C_2 f(z^*)}{(\alpha / 0.5)}, \quad (2.6)$$

where C_2 is a constant. With (2.5) and (2.6), (2.4) becomes

$$\int_0^1 \left(\frac{\partial U}{\partial z^*} \right)^2 f(z^*) dz^* = \frac{t_{ml} \alpha}{C_2} \int_{z_1}^h C_D a U \frac{\partial U}{\partial z} dz. \quad (2.7)$$

Because unbounded vegetated shear layers have no externally imposed length scale, it is reasonable to assume an approximate self-similarity of velocity profiles (as is done for all free shear flows). Furthermore, we will assume that $f(z^*)$ has a single, universal form in vegetated shear layers. Under these two assumptions, the left-hand side of (2.7) will scale upon $(\Delta U)^2$. So, if $(C_D a)$ is assumed to be constant through the canopy, then (2.7) becomes

$$(\Delta U)^2 \sim (h - z_1) C_D a (U_h^2 - U_1^2), \quad (2.8)$$

where U_h and U_1 are the mean velocities at the top of the canopy and at the bottom of the shear layer respectively. Recall that the scaling relationship in (2.8) holds if the production and drag dissipation of SKE are equal. As we postulate that shear layer growth ceases once this equality is satisfied, it is expected that the stability parameter

$$\Omega = \frac{1}{(h - z_1) C_D a} \left(\frac{(\Delta U)^2}{U_h^2 - U_1^2} \right) \quad (2.9)$$

will be a universal constant for fully-developed vegetated shear flows. At the beginning of shear layer development, SKE production outweighs dissipation and Ω (a scaled ratio of production to dissipation) will be high. The resulting increase in SKE is manifest as vortex growth, and thus an increase in $(h - z_1)$, such that Ω will decrease along the canopy until reaching its equilibrium value. SKE production and dissipation will then be equal and shear layer growth will cease. The following experiments were conducted to confirm the universal constancy of Ω in fully-developed vegetated shear layers.

2.3 Experimental methods

Laboratory experiments were conducted in a 24-m-long, glass-walled recirculating flume with a width (b) of 38 cm (Figure 2-2). A constant flow depth (H) of 46.7 cm was employed. Smooth inlet conditions were created using a dense array of emergent cylinders to dampen inlet turbulence and a flow straightener to eliminate swirl. Model

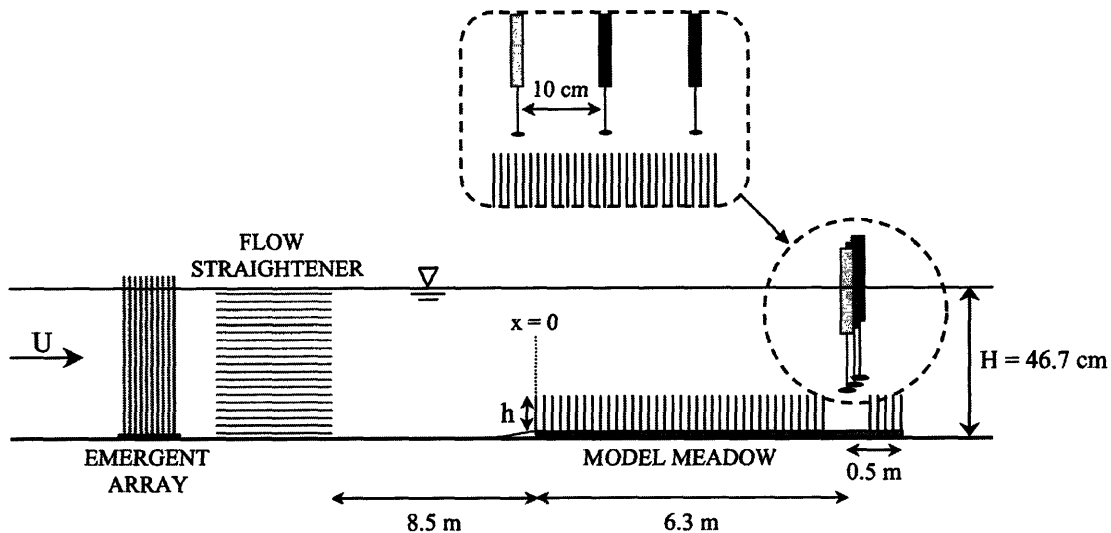


Figure 2-2: Side view of the 38-cm-wide laboratory flume (note the vertical exaggeration). Smooth inlet conditions were created using a dense array of emergent cylinders to dampen inlet turbulence and a flow straightener to eliminate swirl. Vertical profiles of ten-minute velocity records were taken with three 3-D acoustic Doppler velocimeters at 25 Hz.

canopies consisted of circular wooden cylinders ($d = 0.64$ cm) arranged randomly in holes drilled into 1.26-m-long Plexiglas boards. Five boards were used, creating a model meadow 6.3 m in length. The packing density (a) was varied between 0.025 cm^{-1} and 0.08 cm^{-1} , as described in Table 2.1. The range of dimensionless plant densities ($ad = 0.016 - 0.051$) is representative of dense aquatic meadows (see, e.g., Chandler *et al.* [8]). The average height of the canopy (h) was 13.8 or 13.9 cm (Table 2.1), changing slightly as dowels were added.

Velocity measurements (u, v, w) were taken simultaneously by three 3-D acoustic Doppler velocimeters (ADV), separated laterally by 10 cm (Figure 2-2). Velocity statistics from the three probes were averaged to obtain the spatial mean, as discussed earlier. All probes were located within the central 30 cm of the flume, outside of the sidewall boundary layers (Nepf and Vivoni [44]). Vertical profiles consisting of 32 ten-minute velocity records were collected at a sampling frequency of 25 Hz. Due to the configuration of the ADV probes, the uppermost 7 cm of the flow could not be sampled. A 8-cm-long slice of dowels (equivalent to 1.6 – 2.8 times the inter-cylinder spacing, ΔS) was removed across the channel to allow probe access. As shown in

Table 2.1: Summary of experimental conditions and vegetated shear flow parameters.

Run	A	B	C	D	E	F	G	H	I	J	K
Q ($\times 10^{-2} \text{cm}^3 \text{s}^{-1}$)	48	17	74	48	143	94	48	143	94	48	17
h (cm)	13.9	13.9	13.9	13.9	13.8	13.8	13.8	13.8	13.8	13.8	13.8
a (cm^{-1})	0.025	0.025	0.034	0.034	0.040	0.040	0.040	0.080	0.080	0.080	0.080
S ($\times 10^5$) [†]	0.99	0.18	2.5	1.2	7.5	3.2	1.3	10	3.4	1.3	0.26
t_{ml} (± 1.0 cm)	32.8	25.3	31.4	30.7	35.4	33.5	28.8	33.9	32.7	28.5	21.8
U_1 (cms^{-1})	1.3	0.50	1.7	1.1	3.5	2.4	1.1	2.7	1.7	0.77	0.27
U_h (cms^{-1})	2.5	1.0	3.5	2.4	6.7	4.6	2.3	6.3	4.0	2.1	0.93
ΔU (cms^{-1})	3.2	1.3	4.9	3.5	9.5	6.0	3.3	11	7.4	3.9	1.7
$h - z_1$ (± 0.5 cm)	12.5	9.0	11.7	11.3	11.3	10.9	10.5	10.6	9.6	8.3	6.4
α	0.38	0.36	0.37	0.37	0.32	0.32	0.36	0.31	0.29	0.29	0.29
Re_{ml} ($\times 10^{-4}$)	1.1	0.34	1.7	1.1	3.7	2.2	1.0	3.8	2.4	1.1	0.36
Re_d	170	68	230	150	460	320	160	400	250	130	57
C_{Dh}	1.2	1.4	1.1	1.1	0.95	0.99	1.1	0.79	0.84	0.92	1.1

[†]The uncertainty of S , which was obtained through least squares regression, was estimated as roughly 5%. Likewise, U_1 , U_h and ΔU represent lateral averages that approximate the horizontal mean with estimated uncertainties of 5%, 10% and 2% respectively.

Ikeda and Kanazawa [29], the removal of canopy elements over a short length ($7\Delta S$ in their study) has little impact upon the measured velocity statistics. All velocity profiles were measured at $x = 6.0$ m. Fully-developed flow (i.e. $\partial/\partial x = 0$) was established well before this sampling point; e.g., t_{ml} and ΔU changed by less than 1% between $x = 4.6$ m and $x = 6.0$ m in Run G.

Eleven flow scenarios with varying values of discharge, Q , and a were examined (Table 2.1). The hydraulic radius Reynolds number ($Re_{Rh} = Q/\{\nu(2H + b)\}$) varied between 1250 (transitional) and 11800 (fully turbulent). However, as discussed in Ghisalberti and Nepf [24], the nature of vegetated flows is likely to be much more dependent upon the mixing layer Reynolds number ($Re_{ml} = \Delta U t_{ml}/\nu$). In unobstructed mixing layers, the transition from laminar to turbulent conditions is characterized by the development of small-scale turbulence superimposed upon the coherent vortical structures. This transition occurs over the range $Re_{ml} \approx 6 \times 10^3 - 2 \times 10^4$ (Koochesfahani and Dimotakis [33]). As shown in Table 2.1, the flow scenarios of this study encompass values of Re_{ml} less than, within, and greater than the critical range.

The surface slope, S , along the meadow was too small to be accurately measured by surface displacement gauges. Therefore, S was estimated as

$$S = \frac{1}{g} \left[\frac{\overline{\partial u'w'}}{\partial z} \right], \quad h < z < z_2 \quad (2.10)$$

in accordance with (2.1). This method provided good estimates of the measured surface slope in the flume of Dunn *et al.* [13] and (in a previous study) the flume used here (Nepf and Vivoni [44]). As shown in Figure 2-3, the vertical profile of $\overline{u'w'}$ within $h < z < z_2$ is clearly linear, allowing easy estimation of S . Above $z = z_2$, secondary circulation appears to significantly affect the vertical gradient of $\overline{u'w'}$ (see Dunn *et al.* [13]).

2.4 Experimental results

2.4.1 Basic properties of velocity profiles

The parameters defining the vegetated shear layer in each experiment are listed in Table 2.1. In this table, the cylinder Reynolds number has been evaluated using the velocity at the top of the canopy (i.e. $Re_d = U_h d / \nu$). The limits of the shear layer (i.e. z_1 and z_2) were taken as an average of the estimated locations of zero shear and of zero Reynolds stress.

The vertical profiles of mean velocity and Reynolds stress for Runs H and J ($a = 0.08 \text{ m}^{-1}$ for both) are shown in Figure 2-3. Below the mixing layer ($z < z_1$), the Reynolds stress and velocity shear are both negligible. The value of $|\overline{u'w'}|$ increases upward through the canopy to approximately $0.02 (\Delta U)^2$ at the canopy top and then decreases linearly above the canopy to a value of zero at $z \approx z_2$. The maximum shear occurs not at the drag discontinuity but an average of 1.2 cm ($\approx 2d$) below the top of the canopy. This is presumably due to a greatly reduced drag coefficient near the free end of the cylinders, as will be shown in §2.4.3. The Reynolds stress, however, is maximized exactly at the top of the canopy, providing the first indication of a reduction in the rate of vertical turbulent transport within the canopy. Figure 2-3 highlights the following trend shown in Table 2.1. For a given value of a (0.08 cm^{-1} in Figure 2-3), increasing the surface slope ($S = 1.3 \times 10^{-5}$ and 1.0×10^{-4} for Runs J and H respectively) increases the shear layer thickness (t_{ml}) and the shear layer penetration into the canopy ($h - z_1$). This is due predominantly to the reduction in

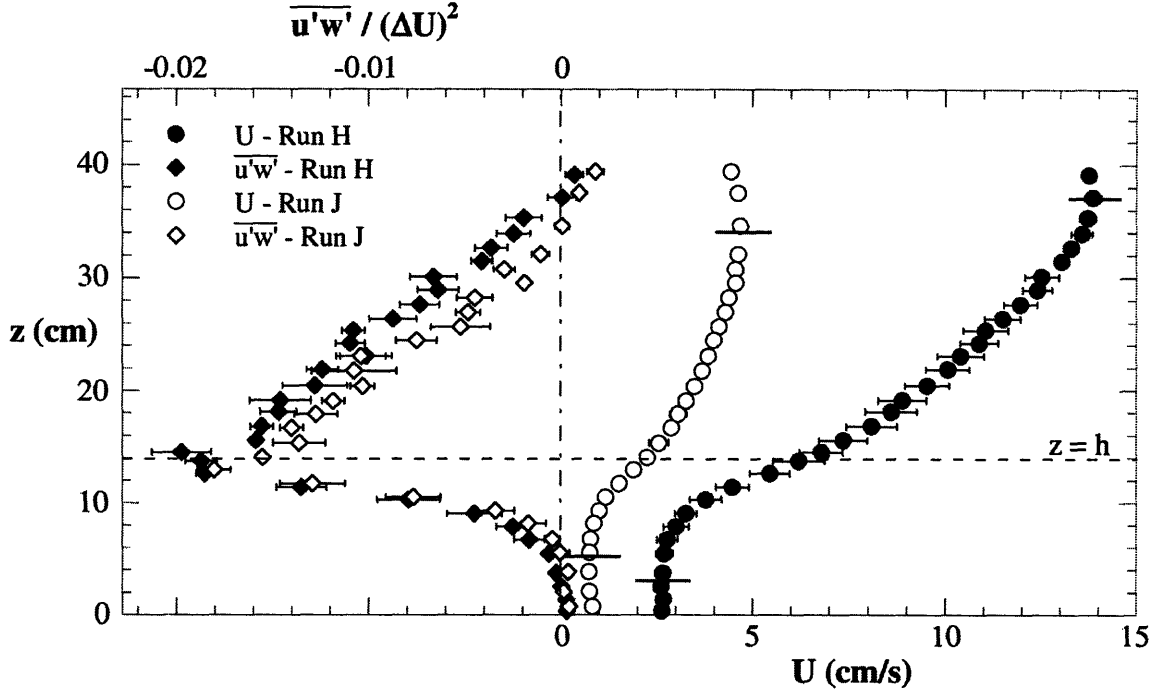


Figure 2-3: Vertical profiles of U and $\overline{u'w'}$ for Run H ($S = 1.0 \times 10^{-4}$) and Run J ($S = 1.3 \times 10^{-5}$). An increase in surface slope causes a slight increase in shear layer thickness and penetration. The value of $|\overline{u'w'}|$ is approximately $0.02 (\Delta U)^2$ at the top of the canopy and decreases linearly above the canopy to a value of zero at $z \approx z_2$. The thick horizontal lines indicate the limits of the shear layers. The thin horizontal bars represent the standard uncertainties in the lateral means of U and $\overline{u'w'}$. In some instances, this measure is smaller than the marker.

drag coefficient with increasing cylinder Reynolds number. Table 2.1 also shows an inverse correlation ($r^2 = 0.8$) between a (the packing density) and α (the fraction of the shear layer within the canopy). That is, denser arrays act as a stronger sink of vortex energy and thus allow less vortex penetration therein.

A distinct correlation was observed between the normalized shear ($\Delta U/U_h$) and the dimensionless plant density (ad) (Figure 2-4), namely

$$\frac{\Delta U}{U_h} \approx 16(ad) + 1, \quad 0.016 < ad < 0.081. \quad (2.11)$$

While it is not surprising that denser arrays generate more shear, it is curious that $\Delta U/U_h$ is not proportional to C_D . The data clearly bear out no dependence upon the drag coefficient; considering the $ad = 0.051$ data, the observed values of $\Delta U/U_h$ vary

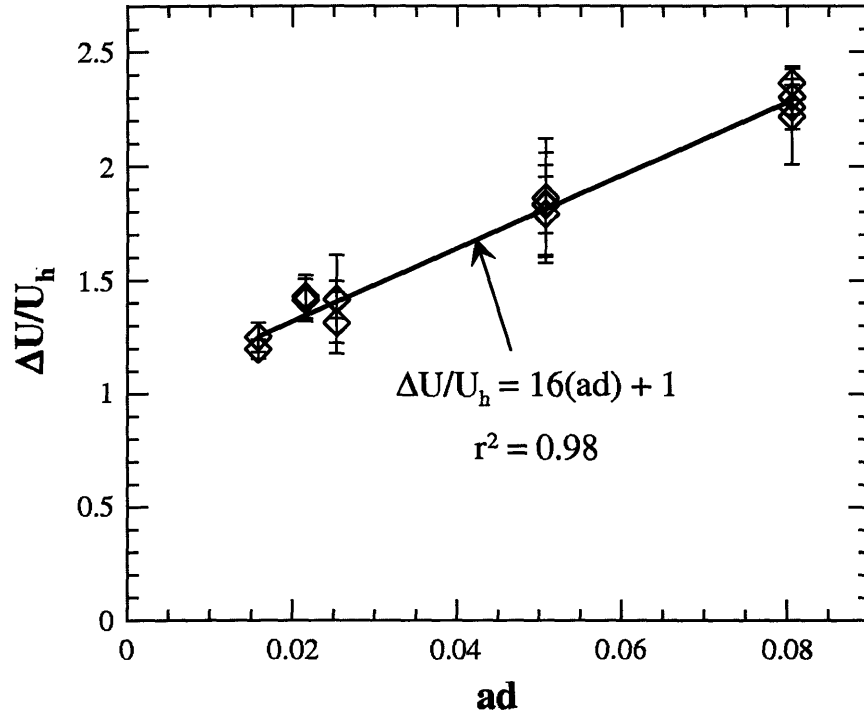


Figure 2-4: The correlation between the normalized shear ($\Delta U/U_h$) and the dimensionless plant density (ad). The $ad = 0.081$ data comes from experiments in which the shear layers penetrated to the bed ($d = 0.64$ cm, $h = 7.1$ cm, provided by M. Ghisalberti, unpublished data, 2002). The vertical bars represent the standard uncertainty in the lateral mean of $\Delta U/U_h$.

by only 4%, despite a 35% variation in a representative drag coefficient, C_{Dh} , defined in §2.4.4 and listed in Table 2.1. It is important to note that (2.11) is only valid within the experimental range $0.016 < ad < 0.081$. We currently have insufficient data from sparse canopies to speculate on the behavior of the curve below $ad = 0.016$. In extremely sparse canopies where the canopy contribution to drag is much less than the bed contribution, the mixing layer analogy will break down completely and the scaling in Figure 2-4 will be invalid.

As shown in Figure 2-3, the flow above the shear layer cannot be described by the one-dimensional momentum balance in (2.1). This is likely the result of secondary currents. As described by Ghisalberti and Nepf [24], the shear layer vortices have a finite width ($b_v \approx t_{ml}/2$) and the flow is divided laterally into several sub-channels of this width. Each channel contains a vortex street that is out of phase with those in

neighboring channels. It is expected that cellular secondary currents develop within each sub-channel, much as secondary currents are generated in sub-channels between neighboring longitudinal bedforms in rivers (see Nezu and Nakagawa [47]). We suggest that these secondary currents are not generated by the flume walls, but rather are inherent to flows with submerged vegetation. This assertion is supported by the fact that vegetated shear layers generated in a wide flume ($2.3 < b/H < 5.5$, Dunn *et al.* [13]) exhibit the same growth behavior as the shear layers in this study ($b/H = 0.8$, see White *et al.* [66]).

2.4.2 Vertical profiles of eddy viscosity and mixing length

This section examines the vertical profiles of eddy viscosity (ν_T) and specifically the validity of the critical assumption that $f(z^*)$ ($= \nu_T(z^*)/C_1\Delta Ut_{ml}$, from (2.5)) has a universal form in vegetated shear layers. Firstly, point estimates of $\partial U/\partial z$ were obtained using central differencing. Then, the vertical profiles of both $\partial U/\partial z$ and $\overline{u'w'}$ were smoothed using a weighted, 5-point moving average. The smoothed values of $\partial U/\partial z$ and $\overline{u'w'}$ were used in (2.5) to estimate ν_T . With the data grouped according to their value of ad , Figure 2-5 depicts the profiles of eddy viscosity (normalized by ΔUt_{ml}) in the shear layers. Note that the vertical scale in this figure is z^* , the distance from the bottom of the shear layer (z_1) normalized by the shear layer thickness (t_{ml}). Due to the differencing and smoothing processes, only values within the range $0.1 \leq z^* \leq 0.9$ could be determined. The data from Runs B and K were not included in this analysis, because the measured values of $|\overline{u'w'}|$ within the shear layer ($O(10^{-2} \text{ cm}^2\text{s}^{-2})$) were not significantly greater than the noise levels of the ADV probes ($O(10^{-2} \text{ cm}^2\text{s}^{-2})$) (Voulgaris and Trowbridge [63]). The collapse of the profiles of ν_T (normalized by ΔUt_{ml}) is excellent, validating the assumption of a singular form of $f(z^*)$ in vegetated shear layers. As expected, the eddy viscosity takes a maximum value (of roughly $0.012 \Delta Ut_{ml}$) in the center of the shear layer ($z^* = 0.5$), irrespective of α .

The validity of a constant mixing length model was also examined, as this will be used in §2.5 to predict the velocity profile. The vertical mixing length, l , is defined

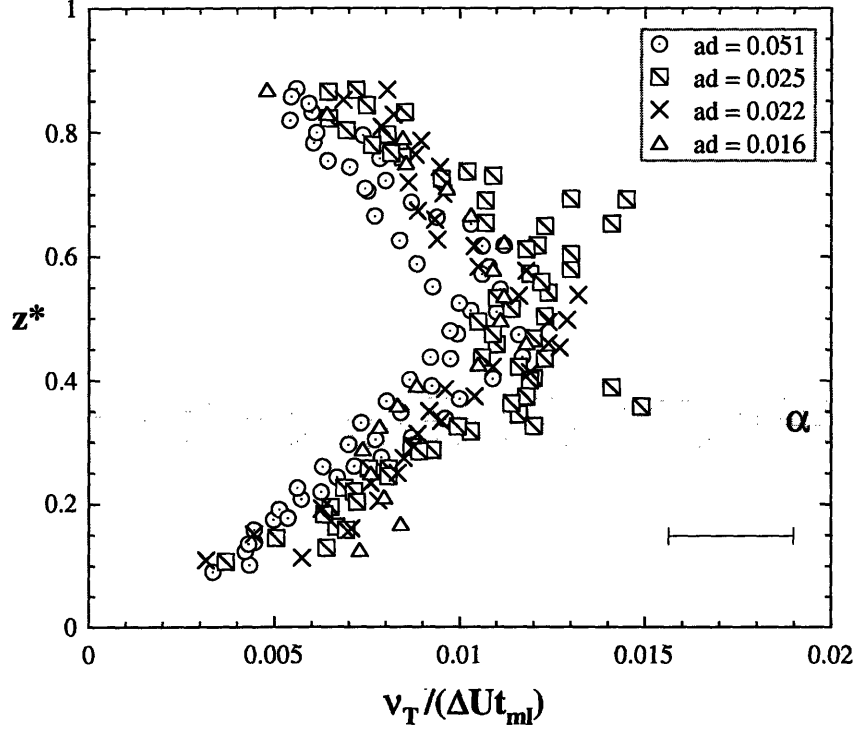


Figure 2-5: Vertical profiles of eddy viscosity (ν_T) throughout the shear layers. The data have been normalized by $\Delta U t_{ml}$ and are grouped according to their value of ad . The vertical scale, z^* , represents the distance from the bottom of the shear layer (z_1) normalized by the shear layer thickness (t_{ml}). The shaded area represents the range of locations of the canopy top ($z^* = \alpha$). The collapse of the profiles of $\nu_T / \Delta U t_{ml}$ is excellent, validating the assumption of a universal form of $f(z^*)$ in vegetated shear layers. The horizontal bar is representative of the standard uncertainty in each data point.

by

$$l^2 = \frac{-\overline{u'w'}}{(\partial U / \partial z)^2} \quad (2.12)$$

and would be expected to scale upon t_{ml} . Figure 2-6 depicts the vertical profiles of l/t_{ml} . The assumption of a constant mixing length throughout the shear layer is quite reasonable as the standard deviation of all values is less than 20% of the mean. In the upper half of the mixing layer, the mixing length is constant ($(0.10 \pm 0.01)t_{ml}$) and the collapse of the data is excellent. Below this region, there is a smooth transition to a minimum value just below the canopy top (located at $z^* = \alpha$). It is worth noting that similarly depressed values are observed near the top of canopies that are more dense ($ad = 0.081$, provided by M. Ghisalberti, unpublished data, 2002) and less

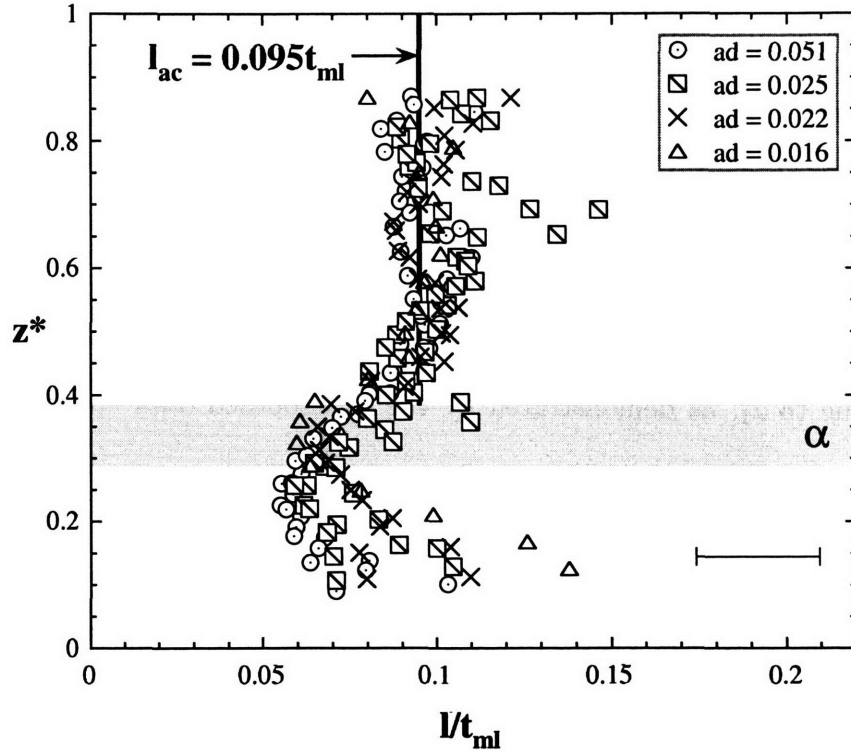


Figure 2-6: Vertical profiles of mixing length (l) throughout the shear layers. The data have been normalized by t_{ml} and are grouped according to their value of ad . The vertical scale is as in Figure 6. The shaded area represents the range of locations of the canopy top ($z^* = \alpha$). The mixing length varies little throughout the shear layer; the standard deviation of all values is less than 20% of the mean. For modeling purposes, the mean mixing length above the canopy (l_{ac}) is $0.095t_{ml}$. The horizontal bar is representative of the standard uncertainty in each data point.

dense ($ad = 0.007$, from Lopez and Garcia [38]) than those employed in this study. For modeling purposes, the mean mixing length above the canopy (l_{ac}) is $0.095t_{ml}$.

Moving downward into the canopy, l increases and takes significantly larger values in the sparser arrays. It was initially thought that the profile of l within the canopy arose from the vertical variation in C_D (as will be discussed in §2.4.3). However, even with C_D assumed constant in a k - ϵ model, Lopez and Garcia [38] predicted that l reaches a local maximum within the canopy and then tends towards zero at the bottom of the shear layer. Examination of the unsmoothed statistics of this study, as well as experiments in which the shear layers penetrated to the bed ($h = 7.1$ cm, $ad = 0.081$, provided by M. Ghisalberti, unpublished data, 2002), reveals that all vertical

profiles of l (with the exception of Run J) do indeed exhibit local maxima deep within the canopy. That the maxima occur at a fairly consistent distance ($0.10 \pm 0.03 t_{ml}$) from z_1 , and not the bed (1–8 cm), suggests that boundary effects are not responsible. Finally, the values of l at the limits of the shear layer make physical sense. At z_1 , all vortical motion has been dissipated by the canopy elements, so l should approach zero. Above the canopy there is no drag dissipation, so l is expected to maintain its constant value to z_2 , as demonstrated by the unsmoothed data and by Lopez and Garcia [38].

For modeling purposes, the slight vertical variation of l within the canopy will be ignored. The mean in-canopy mixing length (l_c) for each run was taken as the average of the unsmoothed values, where a linear extrapolation from the local maximum to zero at $z = z_1$ was applied. The mean normalized in-canopy mixing length (l_c/t_{ml}) correlates well with the penetration ratio (α). Considering all nine runs in Figure 2-6,

$$\frac{l_c/t_{ml}}{\alpha} = 0.22 \pm 0.01. \quad (2.13)$$

This indicates that the destruction of vortical motion by the canopy decreases the in-canopy mixing length and the extent of vortex penetration to the same degree. In an infinitely sparse array (for which we would expect $\alpha = 0.5$), the mean mixing length based on (2.13) approaches the value observed well above the canopy ($0.1t_{ml}$), as expected.

An approximately constant mixing length in vegetated aquatic shear layers contrasts sharply with the terrestrial analogue, in which vertical turbulent length scales increase with height (see, e.g., Raupach *et al.* [52]). Terrestrial vegetated shear layers are, however, embedded within an atmospheric boundary layer of a much larger scale. The height-dependence of vertical length scales is indicative of the extent to which boundary-layer-scale turbulence impacts transport within terrestrial vegetated shear layers. In aquatic flows, the general absence of an extensive overlying boundary layer should allow an approximately constant mixing length (that scales upon the vortex size) throughout the shear layer, irrespective of the canopy density.

2.4.3 Drag coefficient of a submerged array

While characterization of the drag coefficient (C_D) for arrays of submerged cylinders was not a focus of this study, it is a necessary step toward evaluating Ω (2.9) and modeling the flow. As a framework, we first consider established relationships for the drag coefficient from previous studies. The drag coefficient of an isolated, infinite, smooth cylinder (C_{DC}) is well known, its dependence on Reynolds number (Re_d) having the form

$$C_{DC} \approx 1.0 + 10.0(Re_d)^{-2/3}, \quad 1 < Re_d < 2 \times 10^5 \quad (2.14)$$

(White [67], p. 210).

For an array of submerged cylinders, however, wake interactions and finite cylinder length will both impact the drag coefficient (C_D). Unfortunately, these effects have not been comprehensively evaluated. The turbulence of upstream wakes delays separation on downstream cylinders, resulting in a lower drag (Zukauskas [70]). Although the transition to a turbulent wake structure within a sparse ($ad < 0.1$), emergent array is expected to occur at $Re_d \geq 200$ (Nepf [46]), the shear-layer-scale turbulence sweeping through submerged arrays may trigger wake turbulence at lower local Reynolds numbers. Bokaian and Geoola [3] quantitatively described the suppression of the drag coefficient of a cylinder when in the wake of an upstream cylinder and its dependence upon the relative positions of the two cylinders. Using this information, Nepf [46] conducted a numerical experiment to evaluate the bulk drag coefficient of an emergent array, by assuming that the reduction in the drag coefficient of an individual cylinder is due entirely to the wake of the nearest upstream cylinder. The author found that the bulk drag coefficient (C_{DA}) of a random, emergent array of cylinders at high Reynolds number decreases with increasing cylinder density (ad), according to the best-fit polynomial

$$C_{DA} = \frac{C_{DC}}{1.16} \{1.16 - 9.31(ad) + 38.6(ad)^2 - 59.8(ad)^3\} \quad (2.15)$$

for $ad < 0.1$. The agreement between experimental data from random, emergent arrays with $Re_d > 200$ and the expression in (2.15) is very good (Nepf [46]).

The free end of a cantilevered circular cylinder generates strong longitudinal vortices near the tip which cause considerable disturbance to the wake structure. The effect of this free-end disturbance is to increase the wake pressure, leading to a reduction in drag, as compared to an infinitely long cylinder. For a single cylinder with a large aspect ratio ($h/d > 13$) at high Reynolds number ($Re_d \approx 4 \times 10^4$), the magnitude of drag coefficient suppression is independent of aspect ratio and is confined to a region that extends $20d$ from the free end (Fox and West [20]). In such cases, the minimum drag coefficient is roughly $0.7C_{DC}$.

The data of Luo *et al.* [40] show that a submerged cylinder ($h/d = 8$) placed a distance $5d$ immediately behind another submerged cylinder has a mean drag coefficient roughly equal to that predicted by combining upstream proximity and free-end effects. However, shear-scale turbulence in the free-stream of vegetated shear flows will undoubtedly alter these effects and the interaction between them. Because no previous studies enable accurate prediction of $C_D(z)$, an empirical form was sought in these experiments for subsequent use in the numerical model.

For each experimental run, the vertical profile of the drag coefficient within the canopy was evaluated using (2.1), i.e.

$$C_D(z) = \frac{2(gS - \partial(\overline{u'w'})/\partial z)}{aU^2(z)}. \quad (2.16)$$

The vertical gradient of $\overline{u'w'}$ was evaluated using a central difference. The ratio of the observed drag coefficient to that for an infinite cylinder array (C_{DA} , evaluated using the depth-specific velocity), will be defined as

$$\eta(z) = \frac{C_D(z)}{C_{DA}(z)}. \quad (2.17)$$

This parameter explicitly describes the effects of the free end on the drag coefficient of the array. The vertical profiles of η for the experimental arrays are shown in Figure 2-

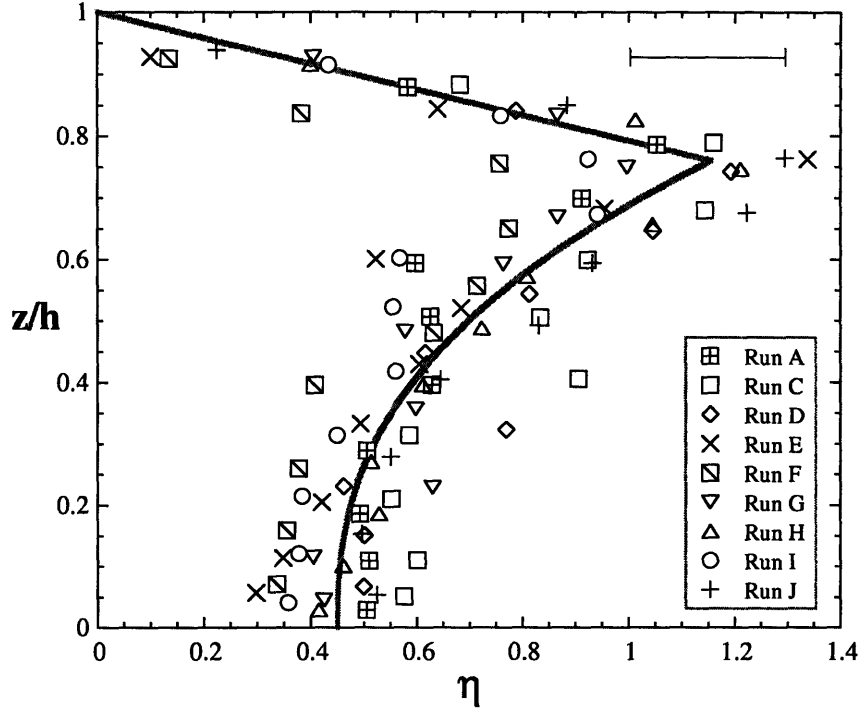


Figure 2-7: Vertical profiles of η , the ratio of the observed drag coefficient to the theoretical value predicted by considering array density and Reynolds number effects. The solid line is a best-fit curve through all points, and has the form shown in 2.18. The horizontal bar is representative of the standard uncertainty in each data point.

7. As in §2.4.2, Runs B and K were not included in this analysis because of uncertainty in recorded values of $\overline{u'w'}$. The collapse of η is good across all flow conditions, with no discernible dependence upon Re_d or ad . From a value of roughly 0.45 at the bed, η increases towards the free end, taking a maximum value of approximately 1.2 at $z/h \approx 0.76$. Above this point, η decreases steadily to zero at the top of the cylinders. The collapsed profiles of η are in fair qualitative agreement with the data of Dunn *et al.* [13] ($ad = 0.002 - 0.016$). The best-fit curve shown in Figure 2-7 takes the form

$$\eta = \left\{ \begin{array}{ll} 1.4 \left(\frac{z}{h}\right)^{2.5} + 0.45, & 0 \leq z/h \leq 0.76 \\ -4.8 \left(\frac{z}{h}\right) + 4.8, & 0.76 < z/h \leq 1 \end{array} \right\}. \quad (2.18)$$

2.4.4 Behavior of the stability parameter

To facilitate evaluation of the stability parameter (Ω), the product $C_{Dh}\bar{\eta}$ was chosen as a representative bulk drag coefficient for the submerged arrays. C_{Dh} is the value of C_{DA} at the top of the canopy (see Table 2.1) and accounts for the effects of Reynolds number and packing density on the drag coefficient. The parameter $\bar{\eta}$ represents the arithmetic average of $\eta(z)$ within the shear layer and accounts for free-end effects. Since $z_1/h < 0.76$ for all runs, from (2.18),

$$\begin{aligned}\bar{\eta} &= \frac{1}{1-\beta} \int_{\beta}^1 \eta(z/h) d(z/h) \\ &= \frac{0.63 - 0.4\beta^{3.5} - 0.45\beta}{1-\beta},\end{aligned}\tag{2.19}$$

where $\beta = z_1/h$.

The estimated values of Ω (8.7 ± 0.5), evaluated using (2.9) and $C_D = C_{Dh}\bar{\eta}$, are remarkably constant (Figure 2-8). Furthermore, Ω exhibits no dependence upon α , suggesting that this constancy extends beyond the experimental range of $0.29 < \alpha < 0.38$. The universal constancy of Ω validates the analysis presented in §2.2 and confirms that the growth of vegetated shear layers ceases once the production and dissipation of SKE are equal.

Interestingly, Ω is independent of both Reynolds numbers that characterize vegetated shear flows: that of the individual cylinders ($Re_d = U_h d/\nu$) and that of the mixing layer ($Re_{ml} = \Delta U t_{ml}/\nu$). Specifically, Ω is independent of whether Re_{ml} is less than, within, or greater than the observed range for transition in mixing layers ($\approx 6 \times 10^3 - 2 \times 10^4$). This is not unexpected, as the transition has a strong effect on small-scale scalar mixing, but not on shear layer growth (Moser and Rogers [41]). Also note that in several runs, $Re_d < 200$ (Table 2.1), violating a requirement of using (2.15) to predict C_D (Nepf [46]). However, the values of Ω exhibit little dependence on Re_d , and the use of (2.15) in this context appears appropriate for $Re_d \geq 60$.

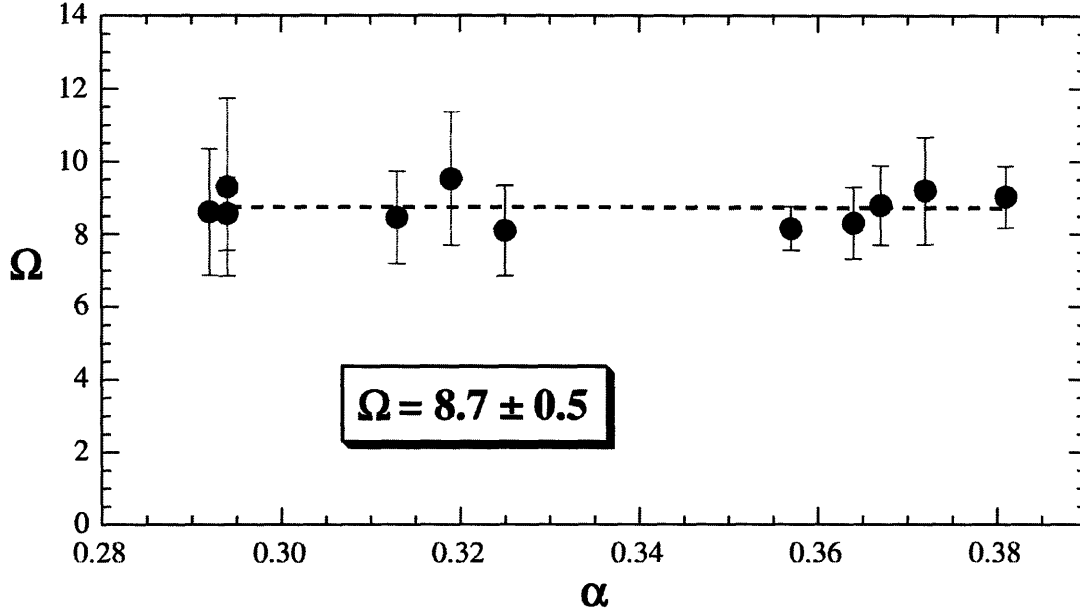


Figure 2-8: The invariability of the stability parameter Ω . The standard deviation (0.5) of the observed values of Ω around the mean (8.7) is very small. There is no dependence of Ω on α , as indicated by the dashed line of regression. The constancy of Ω confirms that shear layer growth ceases once the production and dissipation of SKE are equal. The vertical bars represent the standard uncertainty in the lateral mean of Ω .

2.5 Numerical model of vegetated shear flow

Having identified the stability constant (Ω) and a mixing length model for Reynolds stress closure, we now use these universal functions to predict the vertical velocity profile of vegetated shear flows. A one-dimensional numerical model of (2.1) was created to determine if experimental velocity profiles could be accurately predicted under the assumptions of constant Ω and mixing length (l_{ac} above the canopy and l_c within). The model requires as input the canopy parameters a , d and h , the slope S and the form of $\eta(z)$.

In the model, the flow was divided into two regions: the portion of the shear layer within the canopy (i.e. $z_1 \leq z \leq h$, Zone 1) and the portion of the shear layer above the canopy (i.e. $h < z \leq z_2$, Zone 2). Below z_1 , the velocity is assumed to be independent of depth and dictated solely by a balance of pressure and drag forces. The nature of the velocity profile above the shear layer was not explored here and

Table 2.2: Summary of modeling equations for the i -th point in Zone 1.

Parameter	Modeling Equation
Velocity profile	1. $\left(\frac{\partial U}{\partial z}\right)_i^2 = \left(\frac{\partial U}{\partial z}\right)_{i-1}^2 + \left[\frac{1}{l_c^2} \left(\frac{1}{2}C_{D,i-0.5}aU_{i-0.5}^2 - gS\right)\right] \Delta z$ 2. $U_i = U_{i-1} + \left(\frac{\partial U}{\partial z}\right)_{i-0.5} \Delta z$
Drag coefficient	$C_{D,i} = \eta_i C_{DA,i}^\dagger$
Mixing length	$l_c = 0.22(h - z_1)$, from (2.13)

$^\dagger \eta(z/h)$ is given in (2.18) and $C_{DA}(z)$ in (2.15).

will certainly depend upon the fraction of the depth that the region encompasses ($1 - (z_2/H)$). The model assumes a constant mixing length (l_c) within Zone 1, such that (2.1) becomes

$$\frac{\partial}{\partial z} \left[\left(\frac{\partial U}{\partial z} \right)^2 \right] = \frac{1}{l_c^2} \left(\frac{1}{2} C_{DA} a U^2 - gS \right) \quad [\text{Zone 1}], \quad (2.20)$$

which must be solved numerically. However, an analytical solution can be found in Zone 2. With a constant mixing length, $l_{ac} = 0.095 t_{ml}$, and an absence of drag, (2.1) becomes

$$\frac{\partial}{\partial z} \left[\left(\frac{\partial U}{\partial z} \right)^2 \right] = \frac{-gS}{(0.095 t_{ml})^2}, \quad (2.21)$$

which has the solution

$$U(z) = U_h + \frac{2\sqrt{gS}}{3(0.095 t_{ml})} \left\{ (z_2 - h)^{3/2} - (z_2 - z)^{3/2} \right\} \quad [\text{Zone 2}]. \quad (2.22)$$

The equations that form the basis of the numerical model of Zone 1 are shown in Table 2.2, where $\Delta z (= (h - z_1)/400)$ is the chosen distance between grid points. The subscript i specifies the grid point number. The use of $i - 0.5$ indicates that the value taken is the mean of values at points i and $i - 1$. The first equation in the table is a discretization of (2.20). As U , $\partial U/\partial z$ and C_D are all interdependent, the model was created in Microsoft Excel, which iterates the modeling equations to determine the solution ($U_i(z)$). The results of a model based on (2.20) and (2.22) will depend heavily upon where the model is initiated (z_1) and where the shear layer ends

(z_2). We thus require two independent relationships that permit the evaluation of these endpoints. The first relationship is obtained from the definition of the stability parameter in (2.9), with $\Omega = 8.7$ and $C_D = C_{Dh}\bar{\eta}$ as described above:

$$h - z_1 = \frac{1}{8.7C_{Dh}\bar{\eta}a} \left(\frac{(\Delta U)^2}{U_h^2 - U_1^2} \right). \quad (2.23)$$

To avoid the interdependence of all variables, it was also necessary to utilize a relationship between characteristics of the shear layer and of the vegetation. To this end, the dependence of the normalized shear ($\Delta U/U_h$) on solely the dimensionless plant density (ad) (shown in (2.11)) was also employed.

The model is initiated at the base of the shear layer (z_1), where $U = U_1$ and $\partial U/\partial z = 0$. Under the assumption of zero Reynolds stress below the shear layer, U_1 is predicted from a balance of pressure and drag forces in (2.1) (i.e. $U_1 = \sqrt{2gS/C_D(z_1)a}$). As $C_D(z_1)$ ($= \eta(z_1)C_{DA}(z_1)$) is itself a function of U_1 , a simple iteration is required. The most accurate predictions of U_1 were obtained with $\eta(z_1) = 0.38$, which lies within the range of values observed deep within the canopy (0.45 ± 0.15) in Figure 2-7. The model then requires the following iteration:

1. Firstly, initial guesses of z_1 and t_{ml} are made. Based on the results of this study, good initial values are $z_1 \approx h - 0.4a^{-1}$ and $t_{ml} \approx (h - z_1)/0.33$.
2. Then, with the initial conditions of $(U, \partial U/\partial z)_{z_1} = (U_1, 0)$, the equations described in Table 2.2 are used to evaluate $U(z)$ up to $z = h$.
3. With the value of U_h obtained in Step 2, and the guessed values of z_1 and t_{ml} from Step 1, the velocity profile above the canopy (up to $z = z_2 = z_1 + t_{ml}$) is determined using (2.22).
4. From the complete profile, the value of $\Delta U/U_h$ is evaluated. The value of t_{ml} is then varied, and Steps 2-4 repeated, until $\Delta U/U_h$ takes the value required by (2.11).
5. Based on the stability analysis, the required value of z_1 is calculated using (2.23). If the required value does not agree with the initial guess, we return to

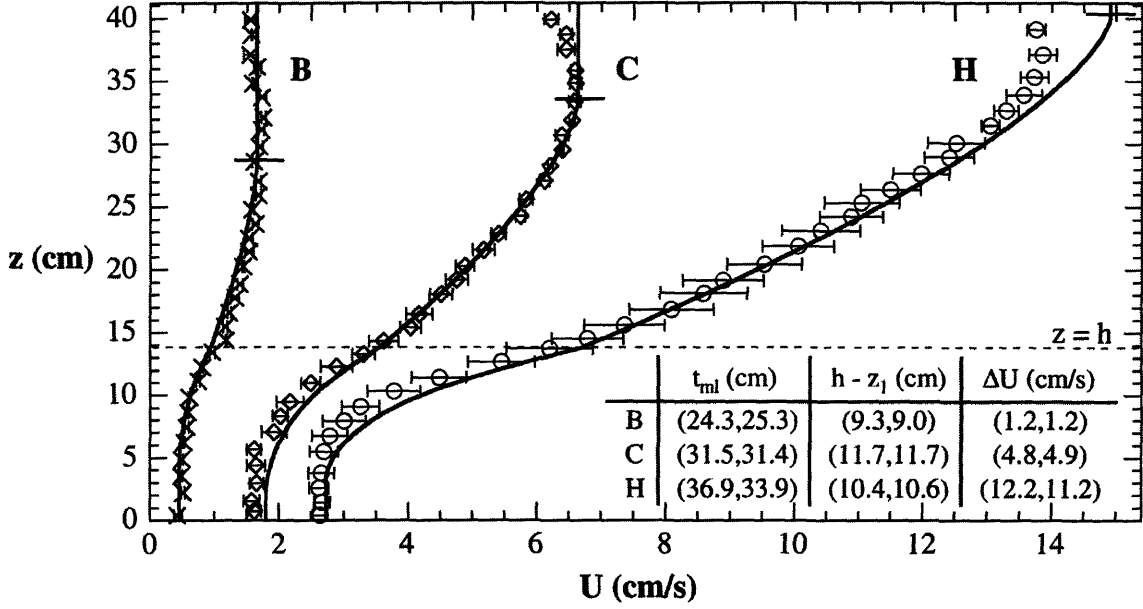


Figure 2-9: A comparison between observed (marker) and predicted (solid line) profiles of mean velocity for Runs B ($a = 2.5 \text{ m}^{-1}$), C (3.4 m^{-1}) and H (8 m^{-1}). The thin horizontal bars represent the lateral variability of the observed velocity. The thick horizontal lines indicate the predicted values of z_2 ; the model is not strictly valid above this point. The table compares the predicted and observed values (P,O) of t_{ml} , $h - z_1$ and ΔU . Over all runs, the model predicts the values of each of these three parameters to within an average of 7%.

Step 1 and take the required value as the next guess. Steps 1-5 are repeated until the required value of z_1 agrees with the guessed value. The final velocity profile then satisfies both conservation of momentum and the criterion defined by the stability parameter.

2.5.1 Comparison between the model and experimental data

The agreement between the observed velocity profiles and those predicted by the model is very good, as shown in Figure 2-9. The predicted values of t_{ml} , $h - z_1$ and ΔU all deviated from observed values by, on average, less than 7%. As a constant in-canopy mixing length was employed, the curvature of the velocity profile within the canopy cannot be modeled exactly. In addition, the velocity gradient has a discontinuity at $z = h$ because of the assumed discontinuity in mixing length. Note

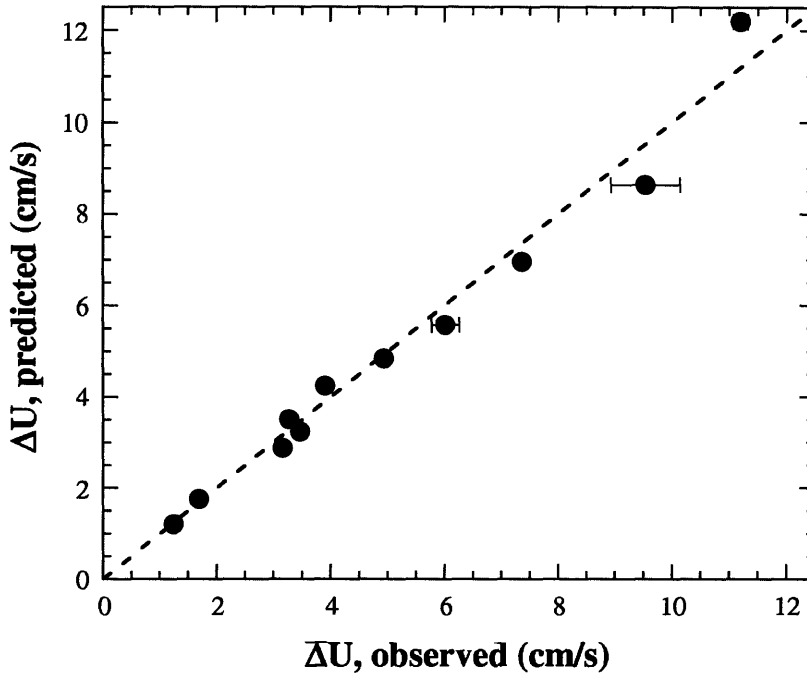


Figure 2-10: The comparison between observed values of ΔU and those predicted by the model. The dashed line indicates perfect agreement. The horizontal bars represent the lateral variability in the observed value of ΔU .

that the model is only used to predict $U(z)$ within the region $0 < z < z_2$. Above z_2 , the velocity begins to decrease as $\overline{u'w'}$ becomes positive (Figure 2-3). The exact nature of the velocity profile above this point could not be determined with the ADV and was not modeled. Finally, there is excellent agreement between the predicted and observed values of ΔU over a wide range of that parameter, as demonstrated in 2-10. Note that while $\Delta U/U_h$ is prescribed by (2.11), U_h is predicted independently, so the accuracy of predicted ΔU values is an independent check of model performance. The good agreement shown in Figure 2-10 indicates that the model is accurate across the gamut of experimental conditions.

The sensitivity of the model to changes in the value of U_1 is highlighted by Figure 2-11, which demonstrates how predicted velocity profiles for Run G vary with U_1 . The predicted values of t_{ml} and ΔU are quite sensitive to a 10% variation in U_1 , changing by roughly 9% and 15% respectively. The predicted value of $h - z_1$ is relatively insensitive, changing by less than 1%. That the accuracy of the model relies heavily

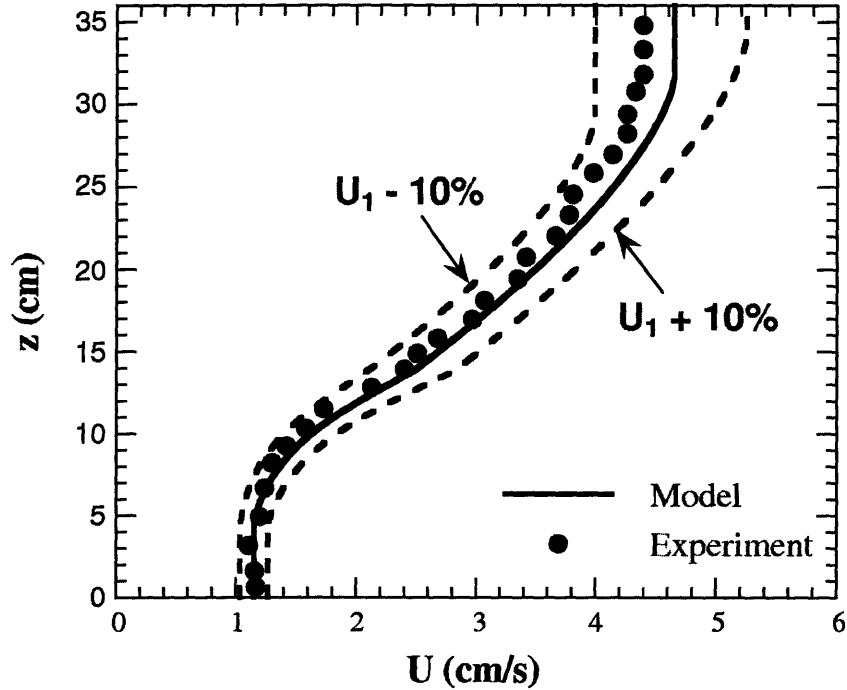


Figure 2-11: Demonstration of model sensitivity to the chosen value of U_1 . The figure shows the model prediction for Run G, using three values of U_1 : (i) the value predicted using $\eta(z_1) = 0.38$ (1.15 cm/s), (ii) a value 10% greater than that predicted (1.27 cm/s) and (iii) a value 10% less than that predicted (1.04 cm/s). The model predictions of t_{ml} and ΔU are sensitive to a 10% variation in U_1 , changing by roughly 9% and 15% respectively. The predicted value of shear layer penetration into the canopy, $h - z_1$, is much less sensitive, changing by only 1%.

upon the accurate prediction of U_1 reinforces the importance of quantifying the drag coefficients of submerged canopies.

2.5.2 Extension of the model to field conditions

Firstly, it is important to note that the analysis described in this paper applies only to completely unbounded vegetated shear layers. That is, shear layers that extend neither to the free surface nor to the bed. The agreement between model and experiment demonstrates that assumptions of constant mixing lengths (l_c , l_{ac}) and a universal stability parameter (Ω) lend themselves to accurate predictions of the velocity profile within and above dense aquatic canopies. However, to extend the model to the field, several pieces of information are required. For example, the relationship

between $\Delta U/U_h$ and ad in sparse canopies ($ad < 0.016$) must be ascertained. Potentially the biggest obstacle to field application of the model, however, is the lack of knowledge concerning $C_D(z)$. The profile used in this study, described by (2.18) and (2.15), is strictly valid only for cylinders with $h/d \approx 22$ within the experimental range of $60 < Re_d < 460$. Further research into the dependence of $C_D(z)$ upon the aspect ratio, packing density, Reynolds number and morphology of submerged canopies is much needed. In the limit of infinitely thin vegetation ($h/d \rightarrow \infty$) however, the assumption of a constant C_D (evaluated using (2.15)) may be appropriate. Furthermore, the experiments in this study used rigid dowels to simulate submerged, aquatic vegetation. In reality, such vegetation is often flexible and can exhibit pronounced coherent waving (*monami*) in a unidirectional current (Ackerman and Okubo [1]; Grizzle *et al.* [27]). The *monami* can significantly increase the penetration of turbulent stress into the canopy, as the waving reduces the drag exerted by the vegetation (Ghisalberti and Nepf [24]). A means of estimating temporal averages of $(C_D a)$ is therefore required before application of this model to waving canopies.

2.6 Conclusion

It was postulated that the growth of vegetated shear layers ceases once the production of shear-layer-scale turbulent kinetic energy is balanced by drag dissipation. This was confirmed by flume experiments, which showed that a scaled ratio of production to dissipation is a constant ($\Omega = 8.7 \pm 0.5$) for fully-developed vegetated shear layers. This stability constant was used to close a one-dimensional numerical model that predicts the vertical velocity profile of vegetated shear flows. The model also uses the assumption of a single mixing length above the vegetation and a single, reduced mixing length within it. The agreement between model and experiment is good, but field application of the model is limited by a lack of description of the drag coefficient in real canopies.

Chapter 3

Mass transport in vegetated shear flows¹

Abstract

Submerged aquatic vegetation has the potential to greatly improve water quality through the removal of nutrients, particulates and trace metals. The efficiency of this removal depends heavily upon the rate of vertical mixing, which dictates the timescale over which these constituents remain in the canopy. Continuous dye injection experiments were conducted in a flume with model vegetation to characterize vertical mass transport in vegetated shear flows. Through the absorbance-concentration relationship of the Beer-Lambert Law, digital imaging was used to provide high-resolution concentration profiles of the dye plumes. Vertical mass transport is dominated by the coherent vortices of the vegetated shear layers. This is highlighted by the strong periodicity of the transport and its simple characterization based on properties of the shear layer. For example, the vertical turbulent diffusivity is directly proportional to the shear and thickness of the layer. The turbulent diffusivity depends upon the size of the plume, such that the rate of plume growth is lower near the source. In the far-field, mass is mixed more than twice as rapidly as momentum. Finally, plume size is dictated predominantly by \hat{X} , a dimensionless distance that scales upon the number of vortex rotations experienced by the plume.

3.1 Introduction

Submerged vegetation is a critical component of many aquatic ecosystems. Aquatic canopies provide habitats for macrofauna (Edgar [15]) and can be responsible for

¹This chapter was submitted by M. Ghisalberti and H.M. Nepf to *Environmental Fluid Mechanics*.

significant nutrient, particulate and trace metal removal in wetlands (Kadlec and Knight [31], Silvan *et al.* [59]). The efficacy of these functions depends heavily upon the rate of exchange between the water within the canopy and the overlying water. Therefore, to fully describe the impact of submerged vegetation on water quality, we must be able to quantify the rate of vertical mixing. Through modification of the flow, vegetation significantly affects vertical transport relative to a bare bed, tending to increase vertical diffusivity above the canopy and to decrease it within (see, e.g., Finnigan [16], Ackerman [2]).

The vertical discontinuity of drag in flows with submerged vegetation creates a shear layer across the top of the canopy. As in a mixing layer, this shear layer contains an inflection point, rendering the flow inherently unstable to Kelvin-Helmholtz vortices (Raupach *et al.* [52], Ikeda and Kanazawa [29]). Vertical transport in a vegetated shear layer is dominated by these coherent vortex structures (Gao *et al.* [22], Ghisalberti and Nepf [24]). The vertical eddy viscosity (ν_{tz}) of the layer scales upon its thickness (t_{ml} , with reference to Figure 3-5) and the shear across it (ΔU), and peaks in the middle of the layer (Ghisalberti and Nepf [23]). As shown by Ghisalberti and Nepf [23], vortex growth ceases once the production of vortex-scale energy is exactly balanced by drag dissipation. Thus, in dense canopies, the vortex structures often do not extend fully to the bed, segregating the canopy into an upper region of rapid exchange and a lower region with more limited water renewal (Nepf and Vivoni [44]). These two regions differ significantly in their rates of turbulent diffusion. Below the shear layer, we assume that the flow resembles that through an emergent array of cylinders, with vertical transport dominated by wake turbulence. In an emergent array the vertical turbulent diffusivity, D_{tz} , scales upon the cylinder Reynolds number ($Re_d = Ud/v$, where U is the longitudinal velocity and d the cylinder diameter) and the areal fraction occupied by wakes (Figure 7 in Nepf *et al.* [45]). Consider a typical canopy with a plant fraction, P , of $O(1\%)$ in a mean flow of $O(10 \text{ cms}^{-1})$. Based on the observations of Nepf *et al.* [45], the vertical diffusivity below the shear layer is $O(0.1 \text{ cm}^2\text{s}^{-1})$. Assuming that the turbulent Schmidt number ($Sc_t = \nu_{tz}/D_{tz}$) is of order unity, the mean vertical diffusivity in the upper canopy (i.e. within the shear

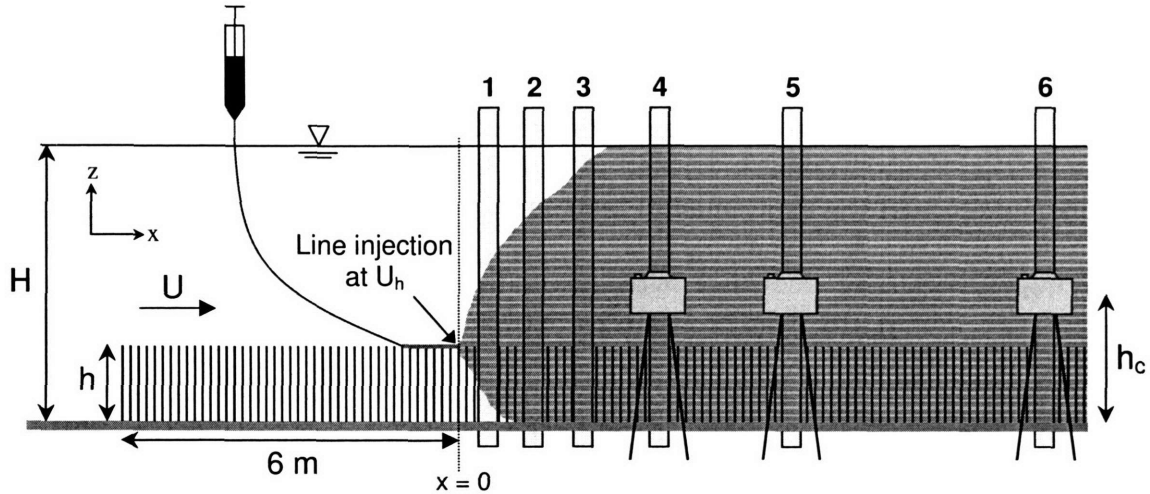


Figure 3-1: Side view of dye injection in the flume. Twelve needles spanning the width of the flume were affixed to the tops of dowels 6 m into the canopy; by this point, the flow was fully-developed. The injection velocity was kept at the local velocity (U_h) by a syringe pump. Vertical light sources were placed at 6 locations along the canopy ($x = 19, 54, 90, 150, 250$ and 380 cm), where digital footage of the dye plume was captured.

layer) is $O(1 \text{ cm}^2\text{s}^{-1})$ (Ghisalberti and Nepf [23]). The order of magnitude difference between the diffusivities in these two regions of the same canopy highlights the impact of the coherent vortices on vertical transport.

The goal of this paper is two-fold. Firstly, we seek to develop a simple, inexpensive experimental technique that allows simultaneous measurement of plume structure at several locations. Secondly, using this technique, we want to characterize vertical mass transport in vegetated shear flows, noting the differences to momentum transport.

3.2 Methodology

Laboratory experiments were conducted in a 24-m-long, glass-walled recirculating flume with a width (w_f) of 38 cm. The experimental setup is summarized in Figure 3-1. Flow scenarios of varying flowrate (Q) and plant density (a) replicate those used in Ghisalberti and Nepf [23]¹, a study conducted with the same flume and canopy, such that details of velocity structure can be drawn from that study. As in Ghisalberti and Nepf [23], a constant flow depth (H) of 46.7 cm was employed, with a canopy

¹This paper is identical to Chapter 2 of this thesis.

Table 3.1: Summary of experimental conditions and vegetated shear flow parameters. Runs B, J and K from Ghisalberti and Nepf [23] were not replicated, as the low velocities complicated the experimental technique.

Run	A	C	D	E	F	G	H	I
Q ($\times 10^{-2} \text{cm}^3 \text{s}^{-1}$)	48	74	48	143	94	48	143	94
ad	0.016	0.022	0.022	0.025	0.025	0.025	0.051	0.051
t_{ml} ($\pm 1.0 \text{cm}$)	32.8	31.4	30.7	35.4	33.5	28.8	33.9	32.7
ΔU (cm s^{-1})	3.2	4.9	3.5	9.5	6.0	3.3	11	7.4
U_h (cm s^{-1})	2.5	3.5	2.4	6.7	4.6	2.3	6.3	4.0
z_1 ($\pm 0.5 \text{cm}$)	1.4	2.2	2.6	2.5	2.9	3.3	3.2	4.2
Re_d [†]	91	110	70	240	170	78	170	110
D_e ($\text{cm}^2 \text{s}^{-1}$) [‡]	0.11	0.13	0.11	0.20	0.16	0.12	0.23	0.18
\overline{D} ($\text{cm}^2 \text{s}^{-1}$) [§]	1.9	2.9	1.9	6.2	3.9	1.8	7.3	4.5

[†] In contrast to Ghisalberti and Nepf [23], Re_d is evaluated here using the velocity below the shear layer.

[‡] D_e , the vertical diffusivity in an emergent stand with equal density and flow speed, was estimated from Figure 7 in Nepf *et al.* [45].

[§] The value in the far-field ($\bar{X} \gtrsim 8$).

height (h) of 13.9 cm. Model canopies consisted of circular wooden cylinders ($d = 0.64$ cm) arranged randomly in holes drilled into Plexiglas boards. The range of dimensionless plant densities ($ad = 0.016 - 0.051$) is representative of dense aquatic meadows (see, e.g., Chandler *et al.* [8]). The total canopy length was 10 m. Table 3.1 details the relevant flow parameters, with each run named as in Ghisalberti and Nepf [23]. In this table, z_1 is the location of the bottom of the shear layer (see Figure 3-5) and Re_d is evaluated using the velocity below this level (U_1). The parameter D_e represents the vertical diffusivity in an emergent array of dimensionless density ad and flow speed U_1 , as prescribed by Figure 7 of Nepf *et al.* [45]. Note that Nepf *et al.* [45] focuses on conditions of $Re_d > 200$, for which the wakes are fully turbulent. In this study, $50 < Re_d < 240$, such that the values of D_e given in Table 3.1 may be overpredictions. It is important to note that this analysis pertains only to canopies of sufficient density that the shear layer does not penetrate to the bed and canopy drag dominates bed drag. This is shown to be true for $C_D ah \gtrsim 0.1$ (as seen in the data of Dunn *et al.* [13] and Poggi *et al.* [51]), where C_D is the drag coefficient of the canopy.

3.2.1 Image analysis

Digital imaging provides an unintrusive method of generating high-resolution concentration data in the laboratory. Data can be gathered simultaneously at all points in a vertical profile, and at several longitudinal locations. To quantify mixing in vegetated flows using digital image analysis, a link between pixel intensity and dye concentration is required. The Beer-Lambert Law (BLL) provides this link, and has been used to determine concentration profiles in flows through porous media (see, e.g., Schincariol *et al.* [54], Gramling *et al.* [26]). The BLL states that when light is incident upon a sample of an absorbing species, the relationship between the incident intensity (I_o) and the transmitted intensity (I) is given by

$$\log \left(\frac{I_o}{I} \right) = \epsilon b C, \quad (3.1)$$

where ϵ is the absorptivity of the absorbing species, b the path length over which the light is attenuated and C the concentration of the absorbing species. If C is non-uniform along the path length, the concentration extracted from (3.1) will be the mean along the path.

The BLL was used to measure concentration downstream of a continuous dye injection from a line of ports spanning the flume. The flume was backlit by 120 cm, 32 W fluorescent lamps, with a blue gel food coloring (Country Kitchen, Inc.) used as the dye. The lamps were wrapped in amber cellophane to maximise the contrast between undyed and dyed fluid. Digital movies were captured by two digital cameras (a Sony DSC-S85 (DC1) and a Canon Powershot G3 (DC2)) and a digital video camcorder (Canon ZR45 (DC3)). From each digital movie, 640×480 bitmap images were acquired using Apple Quicktime (DC1, DC2) and ULead Video Studio (DC3). MATLAB's Image Processing Toolbox was used to convert images to grayscale and evaluate pixel intensity (0 to 255) to determine spatial fields of I (during dye injection) and I_o (before injection). The intensity of the lamps was uniform and constant, $\log I_o$ varying by approximately 0.2% in the innermost 50×1 cm of the tubes and by 0.1% between images.

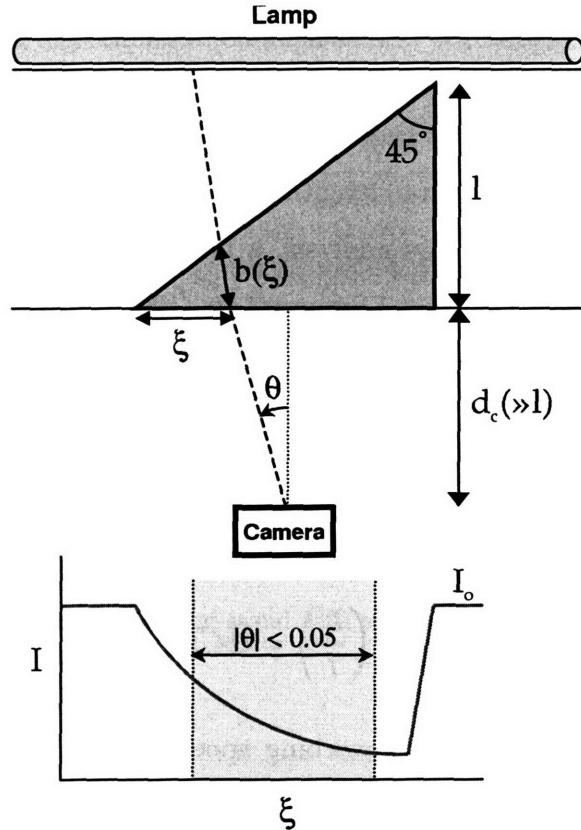


Figure 3-2: Plan view of the calibration used to determine the validity of the Beer-Lambert Law (3.1) in these experiments. Digital movies were captured of the backlit isosceles tank ($l = 36$ cm) filled with water and three dye solutions. The path length of light through the tank (b) varied with distance along the front of the tank (ξ , (3.2)). This allowed examination of the validity of (3.1) fully in the range $0.12 < bC < 4.0$ cmgL^{-1} . The variation of attenuated light intensity along the tank is shown in the lower graphic. To minimize uncertainty in b , only central pixels ($|\theta| < 0.05$) were examined.

To determine the validity of (3.1) in these experiments, a simple calibration was conducted using a right-angled isosceles acrylic tank ($l = 36$ cm, Figure 3-2). When placed in the flume, the path length through the triangle between the horizontal lamp and the camera varied along the length of the tank. Each camera was paired with a lamp and used to capture four digital movies of the backlit triangle: one while filled with water, and three while filled with dye solutions (0.017 , 0.045 and 0.136 gL^{-1}). The distance from the camera to the flume ($d_c = 210$ cm) was much greater than the width of the triangle. Using the definitions in Figure 3-2, the length of dye (b)

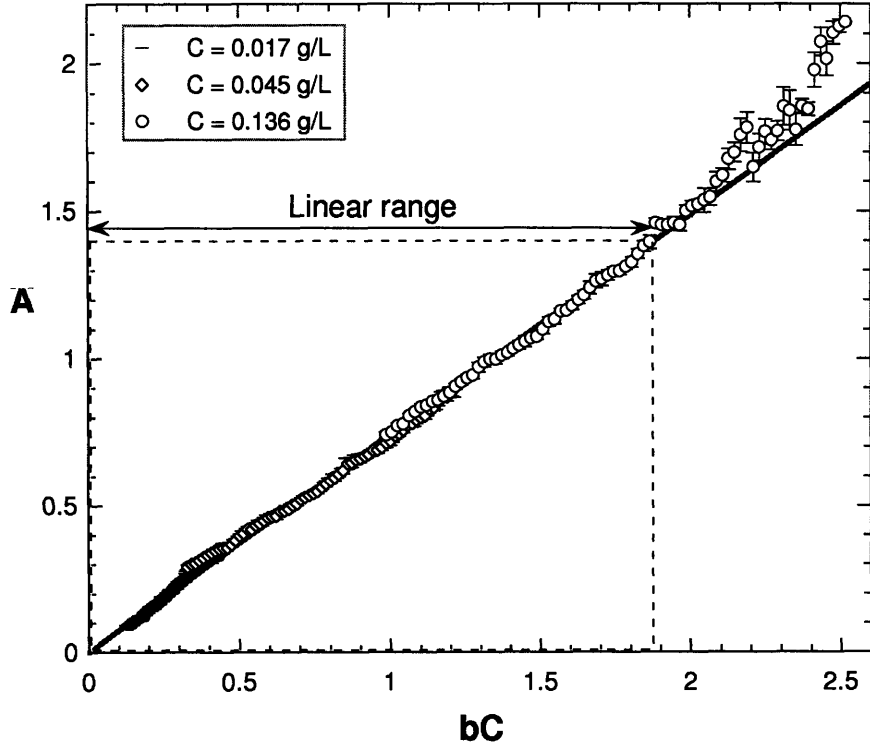


Figure 3-3: The relationship observed by DC2 between absorbance ($A = \log(I_0/I)$) and bC for three dye solutions in the triangular tank. The linear relationship prescribed by the Beer-Lambert Law is valid in the range $0 < bC < 1.9$. The vertical error bars represent the uncertainty in the mean due to spatial (over the height of the tank) and temporal (between images) variability.

between lamp and camera at pixel position ξ is given by

$$b \approx \frac{\xi}{\cos(\theta/n) + \sin(\theta/n)} \approx \frac{\xi}{\left(1 + \frac{(l/2) - \xi}{nd_c}\right)}, \quad (3.2)$$

where n is the relative refractive index of water. This approximation is valid in the limit of small θ , a restriction imposed to minimize uncertainty in b . Equation (3.2) was used to determine b for each pixel in the range $7.5 \text{ cm} < \xi < 28.5 \text{ cm}$ ($|\theta| \leq 0.05$). In each pixel, the intensities in the absence of dye (I_0) and in the presence of the three light-attenuating dye solutions (I) were evaluated. Figure 3-3 shows the calibration plot of absorbance ($A = \log(I/I_0)$) versus bC for camera DC2. The linear relationship described by the BLL is clearly evident in the range $0 \leq bC \leq 1.9 \text{ cmgL}^{-1}$ ($0 \leq A \leq 1.4$). Similarly, the BLL was shown to be valid for

DC1 and DC3 in the ranges $bC \leq 1.4 \text{ cmgL}^{-1}$ and $bC \leq 1.3 \text{ cmgL}^{-1}$ respectively. Note that ϵ does not have to be maintained exactly between experiments; rather, (3.1) will be used to determine relative concentrations, with absolute concentrations obtained through conservation of mass. This calibration merely imposes the range over which there is a linear relationship between concentration and absorbance for each camera.

3.2.2 Experiments

In these canopies, shear layer growth is arrested, and fully-developed flow conditions (i.e. $\partial/\partial x = 0$) established, within the first 5 m of the canopy (Ghisalberti and Nepf [23]). As our analysis is concerned with mass transport in fully-developed vegetated shear layers, dye was injected into the flume 6 m into the canopy. We will define this point as $x = 0$. Twelve 0.9-mm-diameter needles (separated by 3.5 cm) constituting a line injection were affixed to the top of dowels spanning the flume at $x = 0$. The needles were connected by 1/8" Polyurethane tubing to three 50 mL syringes. A syringe pump maintained the injection velocity at the local mean velocity, U_h . The volumetric injection rate, \dot{V}_i , varied between $0.17 - 0.50 \text{ mLs}^{-1}$. At six measurement locations ($x_i = [19 \text{ cm}, 54 \text{ cm}, 92 \text{ cm}, 150 \text{ cm}, 250 \text{ cm}, 380 \text{ cm}]$), dowels within a 4-cm-long slice across the channel were removed and redistributed along the canopy. This was done to allow a line of sight between each lamp (now vertically aligned) and its corresponding camera. The length of this slice is equivalent to $0.8 - 1.4$ times the inter-cylinder spacing, ΔS . As shown in Ikeda and Kanazawa [29], the removal of canopy elements over a short length ($7\Delta S$ in their study) has little impact upon the flow conditions.

The dye solutions used in these experiments had concentrations (C_i) of $120 - 250 \text{ gL}^{-1}$. The addition of isopropyl alcohol brought the solutions to neutral buoyancy, defined arbitrarily as having the buoyant velocity of the dye (w_b) less than 0.5% of the mean channel velocity. For each flow scenario, the three cameras were used to capture movies of the plume at measurement locations 1, 2 and 3. The flume was then re-filled, the dye injection repeated, and movies captured at measurement

locations 4, 5 and 6. To keep all images within the linear ranges described in §3.2.1, less concentrated dyes were used when capturing digital footage at positions 1, 2 and 3. Likewise, DC2, which had the most extensive linear range, was always used in the measurement location nearest to the source. The camera-lamp pairings and the camera settings were unchanged from the calibration. The duration of dye injection (t_d) varied between 3 and 8 minutes. This time was chosen carefully so as to be large enough that a steady state was reached at all locations ($t_d \gtrsim x_{l,\max}/U_1$) and small enough that no dye recirculated to the most upstream location. Note that Runs B, J and K from Ghisalberti and Nepf [23] have not been included in these experiments. In such low flows, the buoyant velocity of the dye and the time taken to reach steady-state made accurate analysis difficult.

In the determination of concentration at heights not equal to the height of the camera (h_c), the line between camera and lamp was not horizontal. The distance between the cameras and the flume ($d_c = 170 - 200$ cm) was kept much larger than the flume width to minimize the resultant parallax error in the measurements. For the same reason, the cameras were positioned at roughly mid-depth ($h_c = 19 - 23$ cm). At the outer edges of the flow, the path from lamp to camera traversed heights within the flume approximately 2 cm greater than and less than the (quoted) mean height.

Frames were captured from the digital movies at 1 Hz and converted to grayscale. The pixel size in the experiments varied between 0.8 – 1.4 mm; near the source, the size of the plume allowed us to zoom in on the region around $z = h$. Figure 3-4 shows a sample background image, an image with dye and the resultant C/C_{max} profile from Run E. Sixteen images preceding dye injection (Figure 3-4(a)) were used to determine $I_o(z)$; this quantity was evaluated by averaging the logarithm of light intensity spatially (over the innermost 1 cm of the lamp) and temporally (over the 16 images). During dye injection (Figure 3-4(b)), $I(z, t)$ was also evaluated as a spatial average over 1 cm. The BLL (3.1) was then used to evaluate $\epsilon C(z, t)$, accounting for the weak height dependence of the path length through the flume ($w_f \leq b < 1.01w_f$). Once a steady-state was reached in all pixels (i.e. $\partial(\epsilon C)/\partial t = 0$), values of $\epsilon C(z)$ were

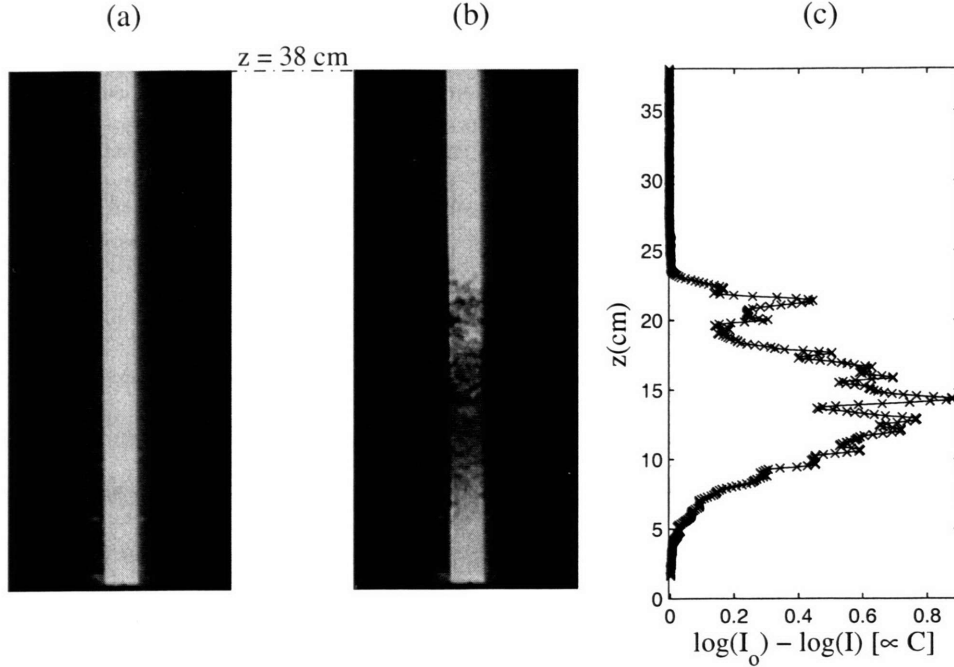


Figure 3-4: Sample evaluation of an instantaneous concentration profile in Run E (captured on DC2). The figures are: (a) A sample background image, used to determine $I_o(z)$, (b) a sample image with dye, used to determine $I(z)$, and (c) the resultant profile of $\log I_o - \log I$, which (ignoring the weak height-dependence of path length through the flume) is directly proportional to concentration (C). As required, $\max(\log I - \log I_o) \approx 0.9 < 1.4$, the linear range end-point (Figure 3-2). Once a steady-state was reached in all pixels, profiles of concentration were averaged over a minimum of 100 images.

temporally averaged over a minimum of 100 images. Values were then normalized by the maximum value in the profile to yield steady-state values of $C/C_{max}(z)$ (Figure 3-4(c)). As the camera settings were fixed during each experiment, ϵ was assumed invariant. Absolute concentrations ($C(z)$) were determined using the conservation of mass requirement that $\int_0^H UCdz = \dot{V}_i C_i / w_f$ (under the assumption that $Pe = Ux_l / D_{tx} \gg 1$).

3.3 Results

Figure 3-5 displays steady-state concentration profiles ($C(z)$) at all measurement locations in Run I. All concentration data have been normalized by the maximum

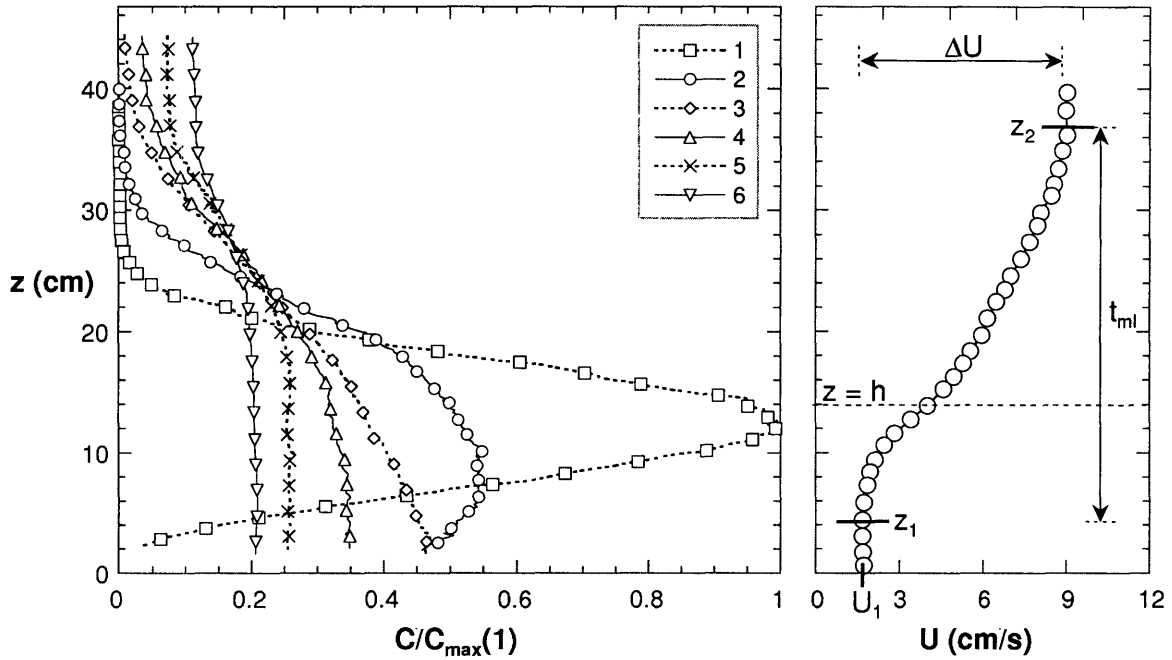


Figure 3-5: Steady-state concentration profiles and velocity profile (taken from Ghisalberti and Nepf [23]) of Run I. All concentration data have been normalized by the maximum value at measurement location 1. The velocity shear and, subsequently, the bed result in a concentration profile that is asymmetric about the injection point ($z = h$). The markers are used simply to identify each profile; the true vertical resolution of the concentration data is approximately 1 mm. The estimated uncertainty in each data point is roughly 10%.

value at measurement location 1. Over distance, the height of maximum concentration falls from the injection height (h) to the bed, initially due to the velocity shear and then due to the no-flux boundary at the bed. The data do not extend to $z = 0$ and $z = H$ because of the parallax error in the measurements; a linear extrapolation of concentration to the boundaries was applied when required.

Intrinsic to this method of image analysis is the lateral averaging of concentration. However, flows with submerged vegetation have significant lateral heterogeneity. In strong currents, flexible submerged vegetation exhibits a pronounced waving (*monami*) at the vortex frequency, f_v . This waving is clearly confined to lateral subchannels (Ghisalberti and Nepf [24]); in each subchannel, the waving (and hence vortex street) is out of phase with that in neighboring subchannels. This lateral heterogeneity is demonstrated in the photographs of Figure 3-6, taken during Run H. This figure

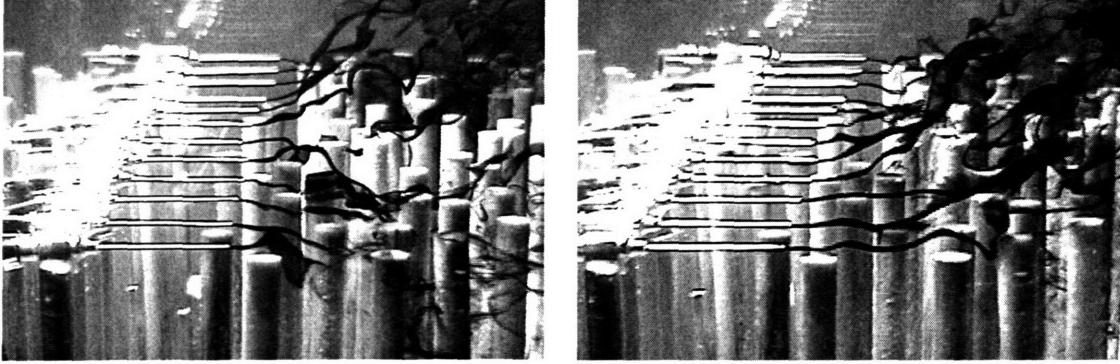


Figure 3-6: Evidence of the lateral heterogeneity in vegetated shear flows. The flow is divided laterally into (in this case, two) subchannels of the vortex width ($\approx t_{ml}/2$). In the left-hand picture, the dye in the vortex street nearer the camera is swept into the canopy simultaneously to the vortex street in the neighboring subchannel ejecting dye above the canopy. In the right-hand picture, taken half a vortex period ($\frac{1}{2f_v}$) later, the reverse is true.

clearly shows the presence of two subchannels. In the left-hand image, dye streaks in the subchannel nearer to the camera undergo a sweep into the canopy ($u' > 0, w' < 0$, using the standard Reynolds decomposition). Simultaneously, the dye streaks in the subchannel farther from the camera undergo an ejection ($u' < 0, w' > 0$). In the right-hand image, taken half a vortex-period ($\frac{1}{2f_v} \approx 7$ s) later, the situation is reversed. Since the plume in each subchannel experiences a periodic sequence of sweeps and ejections, the laterally-averaged profile provides a good estimate of the temporal average in each subchannel. It is important to note that the subchannel width appears to be a function of the vortex size, such that in shallower flows in the same flume, three subchannels have been observed (Ghisalberti and Nepf [24]).

The influence of the coherent vortices in vegetated flows is elucidated in Figure 3-7. Figure 3-7(a) captures a dye injection, distinct from the experiments described in §3.2.2, during Run H. The incorporation of the dye streak into a growing vortex at the front of the canopy (roughly 1.5 m in) is clearly evident. Such clarity of visualization of the vortical structure was only possible near the front of the densest canopy, where the rate of vortex rotation is highest. Figure 3-7(b) shows the smoothed power spectrum of the depth-averaged in-canopy concentration at measurement location 1 in Run E.

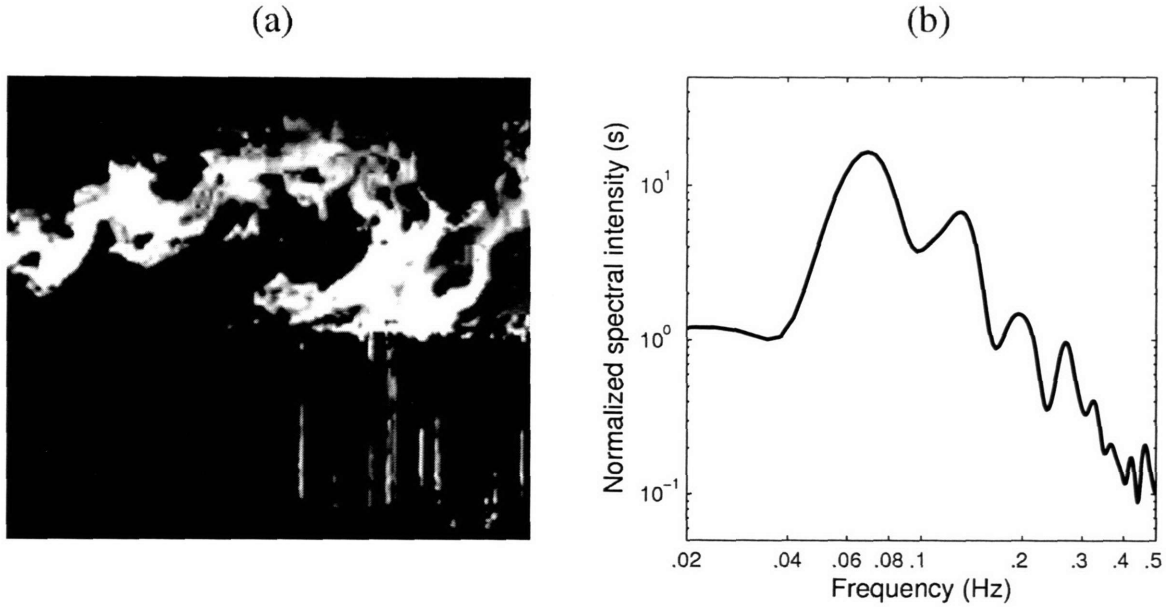


Figure 3-7: The importance of Kelvin-Helmholtz vortices in vertical transport in vegetated shear flows. (a) The negative image of a dye injection made at the front of the canopy in Run H. The dye rises (as fluid is redirected over the drag elements) before being incorporated into the growing vortex street approximately 1.5 m into the canopy. (b) The smoothed power spectrum of the depth-averaged in-canopy concentration at measurement location 1 in Run E. There are clear, pronounced peaks at the vortex frequency (f_v , 0.068 Hz) and $2f_v$.

There are clear peaks at both f_v (the vortex frequency, 0.068 Hz) and $2f_v$, as there are in spectra of momentum transport, $u'w'$ (Ghisalberti and Nepf [24]). The strong periodicity of in-canopy concentration is indicative of the dominance of the vortices in vertical transport. The presence of two subchannels in these flows, combined with the lateral averaging of concentration, augments the peak at $2f_v$. The average Strouhal number ($St = f_v\theta/\bar{U}$, where θ is the momentum thickness of the shear layer and \bar{U} is the average of the velocities at the top and bottom of the layer) is 0.037 ± 0.002 . This is slightly higher than the value observed for bent, flexible canopies (0.032 ± 0.002) but in agreement with the value observed when the same flexible canopy was erect under low flows (0.037 , Ghisalberti and Nepf [24]).

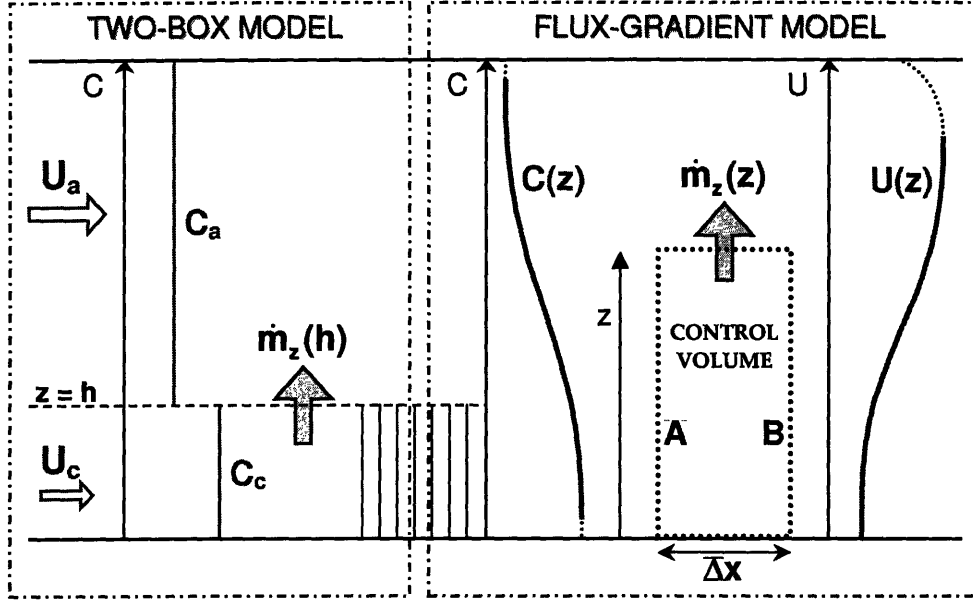


Figure 3-8: Definitive diagram of the two-box and flux-gradient models used to describe vertical transport. In the two-box model, concentration and velocity are considered uniform in both the upper ($h < z < H$) and lower boxes ($0 < z < h$). Extrapolation of the experimental concentration and velocity profiles was required at the outer edges of the flow. These extrapolations are represented with dotted lines.

3.3.1 Two-box model

To characterize vertical transport in vegetated shear flows, the validity of a two-box model was examined. As shown in Figure 3-8, we seek to quantify the mass flux ($\dot{m}_z(h)$) between the upper, unvegetated box ($h < z < H$) and the lower, vegetated box ($0 < z < h$). Velocity and concentration are considered uniform within each box (U_a and C_a in the upper box, U_c and C_c in the lower box). We assume a constant exchange coefficient (k , with units of LT^{-1}) such that $\dot{m}_z(h)$ is proportional to k and the difference in concentration between the boxes. That is, over a distance dx ,

$$\dot{m}_z(h) = k (w_f dx) (C_c - C_a). \quad (3.3)$$

While this exchange parameter doesn't take into account vertical variation in velocity and diffusivity, it is a useful tool when considering chemical and biological processes that occur fully within the canopy and not at all above it (e.g., nutrient uptake).

Using this two-box formulation, the exchange coefficient can be evaluated by track-

ing the longitudinal variation in the concentration of one of the boxes. Over the distance dx ,

$$dC_a = \frac{\dot{m}_z(h)}{(H-h)w_f dx U_a} = \frac{k dx}{(H-h)U_a} (C_c - C_a) \quad (3.4)$$

using (3.3) and assuming $Pe \gg 1$. Therefore,

$$\frac{dC_a}{dx} = \frac{k}{(H-h)U_a} (C_c - C_a). \quad (3.5)$$

Similarly,

$$\frac{dC_c}{dx} = -\frac{k}{hU_c} (C_c - C_a). \quad (3.6)$$

By defining $\Delta C = C_c - C_a$ as the difference in concentration between the two boxes, subtracting (3.5) from (3.6) gives

$$\frac{d\Delta C}{dx} = -k \left(\frac{1}{hU_c} + \frac{1}{(H-h)U_a} \right) \Delta C. \quad (3.7)$$

Integration of (3.7) yields

$$\Delta C(x) = \Delta C(0) \exp \left(-kx \left(\frac{1}{hU_c} + \frac{1}{(H-h)U_a} \right) \right). \quad (3.8)$$

By substitution of (3.8) into (3.6),

$$\frac{dC_c}{dx} = -\frac{k\Delta C(0)}{hU_c} \exp \left(-kx \left(\frac{1}{hU_c} + \frac{1}{(H-h)U_a} \right) \right). \quad (3.9)$$

Therefore,

$$C_c(x) = \frac{\Delta C(0)}{\left(1 + \frac{hU_c}{(H-h)U_a} \right)} \exp \left(-kx \left(\frac{1}{hU_c} + \frac{1}{(H-h)U_a} \right) \right) + C_c(\infty), \quad (3.10)$$

where $C_c(\infty)$ is the concentration achieved when the dye has become perfectly well-mixed over depth. That is,

$$C_c(\infty) = \frac{hU_c}{hU_c + (H-h)U_a}. \quad (3.11)$$

From (3.10) we define C^* , the normalized in-canopy concentration, as follows:

$$C^*(x) = \frac{C_c(x) - C_c(\infty)}{C_c(0) - C_c(\infty)} = \exp\left(-kx \left(\frac{1}{hU_c} + \frac{1}{(H-h)U_a}\right)\right). \quad (3.12)$$

That is, under the assumptions of uniform velocity and concentration within each box, C^* decays exponentially with distance along the canopy (from unity to zero). As the injection is at the interface between the two boxes,

$$C_c(0) = \dot{V}_i C_i / 2hw_f U_c. \quad (3.13)$$

To account for concentration and velocity gradients in the experiments, quantities within boxes are represented by vertically-averaged experimental values (i.e. $G_c = \frac{1}{h} \int_0^h G dz$; $G_a = \frac{1}{(H-h)} \int_h^H G dz$, where $G = [U, C]$). As described in Ghisalberti and Nepf [23], velocity measurements could not be taken within approximately 7 cm of the free surface. The experimental velocity profiles were extrapolated to the surface (see Figure 3-8) to best match near-surface profiles taken above vegetated shear layers [M. Ghisalberti, unpublished data, 1999]. Figure 3-9 shows the observed exponential decay of C^* over distance. Data with the same plant density (but different flow speeds) are grouped. The vertical bars represent the standard uncertainty in each point and thus reflect the variability within each group. This variability is small, with a mean of roughly 0.02 on the C^* scale. The legend of Figure 3-9 displays the mean in-group values of k^* , the fitting coefficient in the curve $C^*(x) = \exp(-k^*x)$. Clearly, the well-mixed condition is approached more rapidly, and k^* is higher, for denser canopies. Denser canopies generate vortices with a greater rotational speed (which scales upon ΔU), relative to the mean flow ($\approx U_h$) (Ghisalberti and Nepf [23]). The higher rates of rotation result in a more rapid flushing of the canopy over distance. The exponential relationship in (3.12) is clearly invalid near the source, where the assumption of a uniform in-canopy concentration breaks down. While the theoretical concentration at the source is given by (3.13), the true value is much lower ($\dot{V}_i C_i / 2hw_f U_h$) since, in reality, the injection is at the point ($z = h$) of the highest in-canopy velocity. The concentration profiles show that the in-canopy concentration becomes uniform

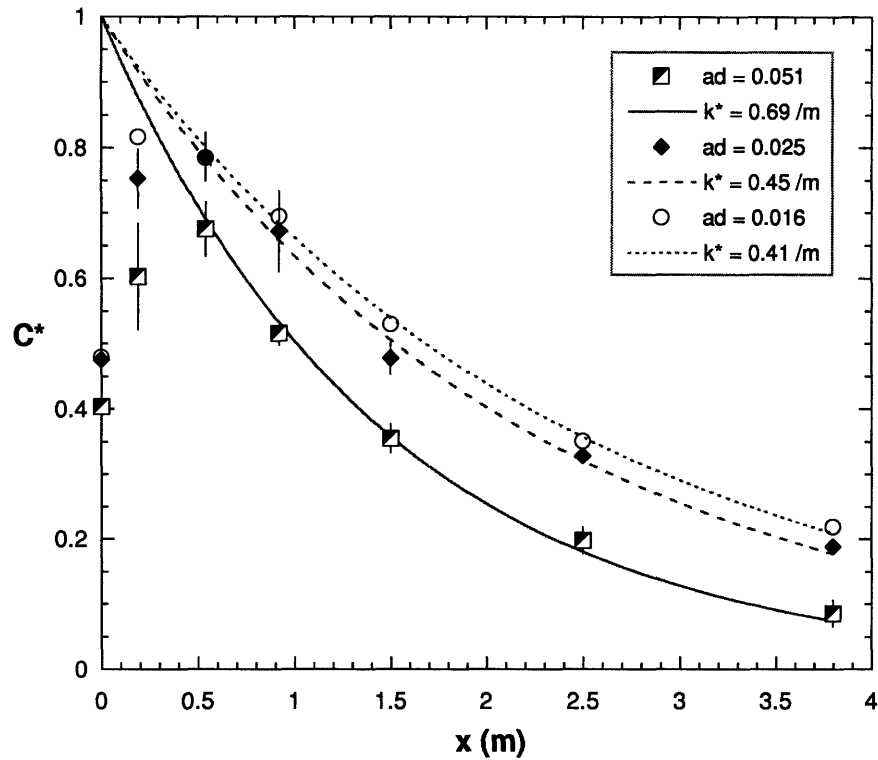


Figure 3-9: The exponential decay of normalized in-canopy concentration (C^*) over distance. Data with the same plant density (but different flow speeds) are grouped, with vertical bars representing the variability within each group. For clarity, the $ad = 0.022$ data (which falls alongside the $ad = 0.025$ data) has been omitted. Exchange between the canopy and overlying water occurs more rapidly over distance for dense canopies. This is highlighted by the mean in-group values of k^* , the fitting coefficient in the curve $C^*(x) = \exp(-k^*x)$. This exponential relationship is invalid near the source, where the assumption of a uniform in-canopy concentration breaks down.

(varying by less than 15% around the mean) by $x = 54$ cm (for $ad = 0.025, 0.051$) and $x = 92$ cm (for $ad = 0.016, 0.022$). The curve fit is only applied beyond this point where, despite the fact that the upper, unvegetated box isn't similarly well-mixed, C^* clearly decays exponentially. Although the curves of best fit were determined by prescribing the intercept (i.e. $C^*(0) = 1$), the exponential fits to the data alone had, on average, an intercept of almost exactly unity. This suggests that the deviation from a uniform in-canopy concentration in the near-field does not significantly affect the bulk exchange between the canopy and the overlying fluid.

We would expect the exchange coefficient (k) to simply scale upon the shear across

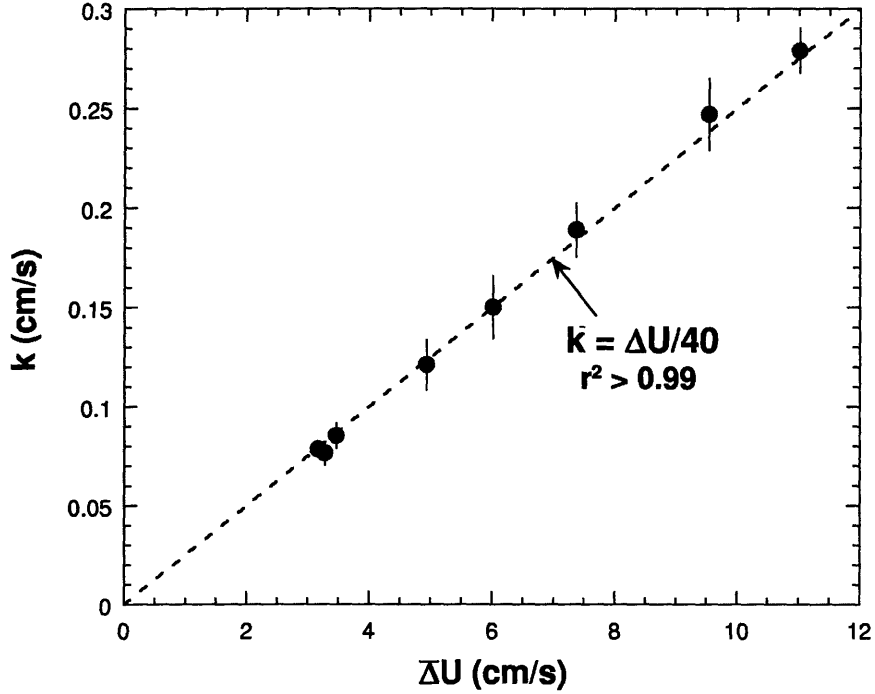


Figure 3-10: The direct proportionality between the exchange velocity, k , and the total shear, ΔU . The vertical bars represent the 90% confidence intervals of each point, based on the uncertainty of the exponential fit through each data set.

the layer (ΔU), as this dictates the vortical velocity of the structures. From (3.12),

$$k = \frac{k^* h U_c}{\left(1 + \frac{h U_c}{(H-h) U_a}\right)}. \quad (3.14)$$

As shown in Figure 3-10 (in which the data are no longer grouped), this expectation is very closely met ($k \approx \Delta U/40$). Therefore, for a given mean flow, the exchange coefficient will increase with canopy density.

3.3.2 Flux-gradient model

While a two-box model is convenient for describing vertical transport, it fails to encapsulate any vertical variability, revealing little of the structure of mass transport. Consequently, a profile of vertical turbulent diffusivity ($D_{tz}(z)$) throughout the shear layer was sought. Similarly to the eddy viscosity, the turbulent diffusivity is expected to scale upon the size of the vortices (t_{ml}) and their rotational speed (which in turn

scales upon ΔU). Although a flux-gradient model is not strictly valid in these flows (refer to Corrsin [11]), it provides a simple means of characterizing vertical transport.

The mass balance for the control volume shown in Figure 3-8 is

$$w_f \left(\int_0^z UC dz \right)_A = w_f \left(\int_0^z UC dz \right)_B - w_f \Delta x \left(D_{tz} \left\langle \frac{\partial C}{\partial z} \right\rangle_z \right). \quad (3.15)$$

The terms represent, respectively, the inward and outward advective fluxes and the vertical diffusive flux. The angular brackets denote a longitudinal average between A and B. Experimental values of $D_{tz}(z)$ were evaluated by considering (3.15) between adjacent measurement locations, i.e.

$$D_{tz}(z) = - \frac{\Delta \left(\int_0^z UC dz \right)}{\langle \partial C / \partial z \rangle_z \Delta x}. \quad (3.16)$$

We assume that the longitudinally-averaged gradient can be approximated by the mean of the gradients at the two measurement locations (i.e. $\langle \partial C / \partial z \rangle \approx (\partial C / \partial z|_A + \partial C / \partial z|_B) / 2$). This assumption is best adhered to in the slowly-varying far-field, so only measurement locations in the range $x_l \geq 92$ cm were used in the evaluation. Furthermore, the determination of D_{tz} was restricted to heights at which $\partial C / \partial z$ changed by less than a factor of 3 between adjacent measurement locations. The vertical profiles of $\partial C / \partial z$ were smoothed with a 2 cm moving window before finding the mean of the concentration gradients at adjacent locations. To minimize the uncertainty in D_{tz} , only heights with significant concentration gradients ($\partial C / \partial z > 0.05 \max(\partial C / \partial z)_{x=92\text{cm}}$) were considered. This meant that the diffusivity was not evaluated near the (no-flux) boundaries, where the vertical concentration gradient approaches zero.

Figure 3-11(a) shows the collapse of D_{tz} , when normalized by $\Delta U t_{ml}$, across the range of plant densities. Data of equal plant density have been grouped, with horizontal bars representing the standard uncertainty in each point. The vertical axis of Figure 3-11(a) ($z^* = (z - z_1) / t_{ml}$) represents the dimensionless height above the shear layer bottom. The collapse of the diffusivity data throughout the entire shear layer is good, confirming that the coherent vortices dominate transport throughout

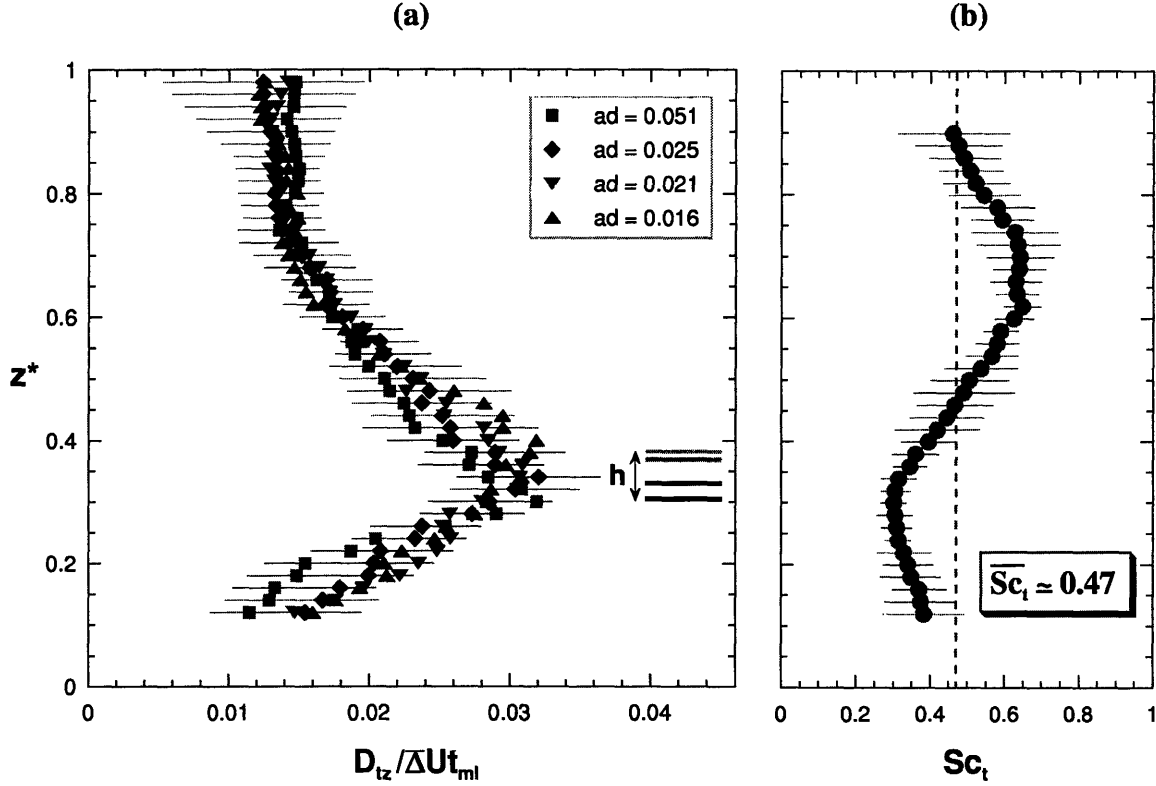


Figure 3-11: (a) The collapse of D_{tz} , when normalized by $\Delta U t_{ml}$, across the range of plant densities. Data of equal plant density have been grouped, with horizontal bars representing the inter-run variability in each point. The vertical axis ($z^* = (z - z_1) / t_{ml}$) represents the dimensionless height above the shear layer bottom. The thick grey bars show the average location of canopy height in z^* space for each plant density; the greater the density, the darker the bar. For each density, the turbulent diffusivity peaks near the top of the canopy. (b) The vertical profile of the turbulent Schmidt number ($Sc_t = \nu_{tz} / D_{tz}$) in the shear layer. Sc_t has an average value of approximately 0.47 in the shear layer and reaches a minimum just below the top of the canopy.

the layer. There is significant vertical variability in D_{tz} , which peaks at the top of the canopy ($D_{tz}(h) \approx 0.032 \Delta U t_{ml}$). In contrast, the eddy viscosity peaks in the middle of the shear layer, which lies above the canopy (Ghisalberti and Nepf [23]). Note that in the mass balance used to evaluate D_{tz} (3.15), an absence of vertical advective mass transport was assumed. The secondary circulation presumed to exist above the shear layer (Ghisalberti and Nepf [23]) may drive a small advective flux in the uppermost 20% of the shear layer. In this region, the calculated value of D_{tz} , which would incorporate this advective transport, does not decrease with height as the eddy viscosity

does. Rather, it takes an approximately uniform value ($D_{tz} \approx 0.013\Delta U t_{ml}$).

The relationship between the eddy viscosity and turbulent diffusivity is shown in Figure 3-11(b), which details the form of the turbulent Schmidt number ($Sc_t = \nu_{tz}/D_{tz}$). There is significant uncertainty in Sc_t in the uppermost 20% of the shear layer, due to both the spread of the D_{tz} data in this region and the possible incorporation of a vertical advective flux into this data. This uncertainty notwithstanding, the average observed turbulent Schmidt number in the range $0.1 < z^* < 0.9$ is approximately 0.47, with the minimum value occurring just below top of the canopy. This indicates that the transport of mass is more than twice as efficient as the transport of momentum in vegetated shear layers. The observed turbulent Schmidt number is lower than those in boundary layers (0.8 ± 0.1 , Launder [36]; Hassid [28]; Koeltzsch [32]) and planar mixing layers (≈ 0.54 , from data in Raupach *et al.* [52]). The difference between vegetated shear layers and unobstructed mixing layers may be explained by numerical results discussed in Fitzmaurice *et al.* [19]. Ensemble averages of the velocity and pressure fields around major sweep events in vegetated flows reveal that when the sweep approaches the canopy, the encounter with the region of high drag generates regions of high dynamic pressure. So, while the sweep event carries momentum and scalars downward via identical motions, the transfer of momentum may be offset by the pressure field induced by the motion at the canopy boundary.

3.3.3 Similarity of plume behavior

Within the shear layer, the coherent vortices dominate vertical transport. Thus, we anticipate that the timescales of plume advection (x/U_h) and vortex rotation ($t_{ml}/\Delta U$) govern the growth of a scalar plume. The ratio of these timescales defines a dimensionless distance,

$$\hat{X} = \frac{x\Delta U}{t_{ml}U_h}, \quad (3.17)$$

that scales upon the number of vortex rotations experienced by the plume. We expect that the concentration profiles will be similar across all runs at a given value of \hat{X} . That is, a given number of vortex rotations are expected to have a similar

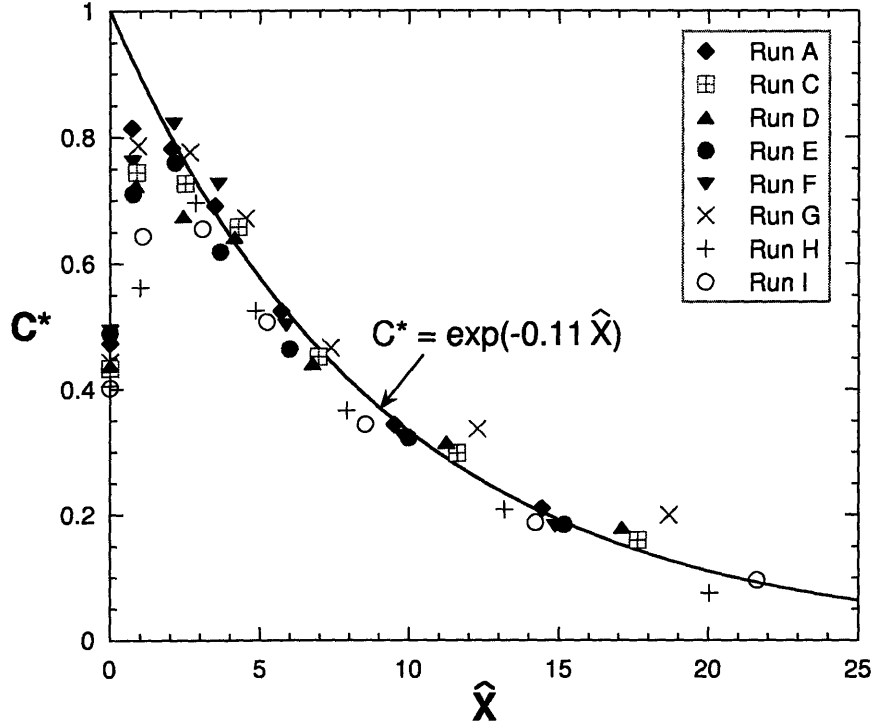


Figure 3-12: The collapse of the decay curves of in-canopy concentration when plotted against a dimensionless distance, \hat{X} . This suggests a strong similarity of plume structure in \hat{X} , which scales upon the number of vortex rotations experienced by the plume.

effect on scalar plumes, irrespective of the canopy density. For example, consider the exponential decay curves of in-canopy concentration as a function of x (Figure 3-9) and as a function of \hat{X} (Figure 3-12). Whilst the behavior of $C^*(x)$ is strongly dependent upon ad , the values of $C^*(\hat{X})$ collapse to a single curve. We therefore expect plume spread and structure, within the shear layer at least, to depend primarily on a single variable, \hat{X} .

3.4 Particle tracking model

Due to the difficulty of determining vertical diffusivity in the near-field, where the concentration profile changes rapidly, the longitudinal dependence of D_{tz} was not directly calculated. As diffusivity in oceans and lakes is known to increase with the size of dye patches (see, e.g., Okubo [48], Lawrence *et al.* [37]), it was thought

that D_{tz} would increase with distance from the dye source. Additionally, we sought to determine the accuracy of a simple model that assumes a diffusivity (\overline{D}) that is constant in the vertical above $z = z_1$. Below this point, vertical transport is assumed to be dominated by wake turbulence, with a diffusivity (D_e) given by Figure 7 in Nepf *et al.* [45] (Table 3.1). Accordingly, we employed a Lagrangian particle tracking model (LPTM, developed by Peter Israelsson, Massachusetts Institute of Technology) to evaluate the longitudinal dependence of \overline{D} .

The LPTM was employed as a two-dimensional (x and z) particle tracking model in which particles are advected by the mean velocity field ($U(z)$) and diffused vertically by a random walk process. Longitudinal diffusion is neglected with respect to advection; assuming that $D_{tx} \sim O(D_{tz})$, the lowest Peclet number in this system is $O(10)$. The model released 3000 particles/s at $x = 0$, $z = h$ and tracked their position for 1000 s over the domain $0 < x < 380$ cm. The cell size in the model was 2 cm (in x) \times 1 cm (z); the number of particles in each cell was divided by the cell area to yield an areal concentration (ML^{-2}). Once a steady-state was reached at each x_l , vertical concentration profiles (sampled at 0.1 Hz) were temporally averaged to provide the steady-state profile. In flows with inhomogeneous diffusivity, particle tracking models often suffer from the over-prediction of concentration in regions of low diffusivity (Weitbrecht *et al.* [64]). In this study, the order of magnitude between \overline{D} and D_e had the potential to result in an unrealistic build-up of concentration below $z = z_1$. However, this was not observed in the LPTM, which predicts a uniform steady-state concentration to within 1% as $x \rightarrow \infty$.

The LPTM was used to determine the values of \overline{D} that best replicated the experimental concentration profiles of each run (i.e. the value that maximized r^2 between the model result and experimental profile). For each measurement location (x_l), \overline{D} was assumed spatially invariant, both vertically and longitudinally in the range $0 < x < x_l$. That is, the best-fit value of \overline{D} best describes the rate of plume growth between the source and the measurement location. Based on the collapse of data in Figure 3-11(a), it was prescribed that $\overline{D} = \gamma \Delta U t_{ml}$ where γ is a constant. From the best-fit values of \overline{D} at each measurement location, $\gamma(\widehat{X})$ was determined for each run,

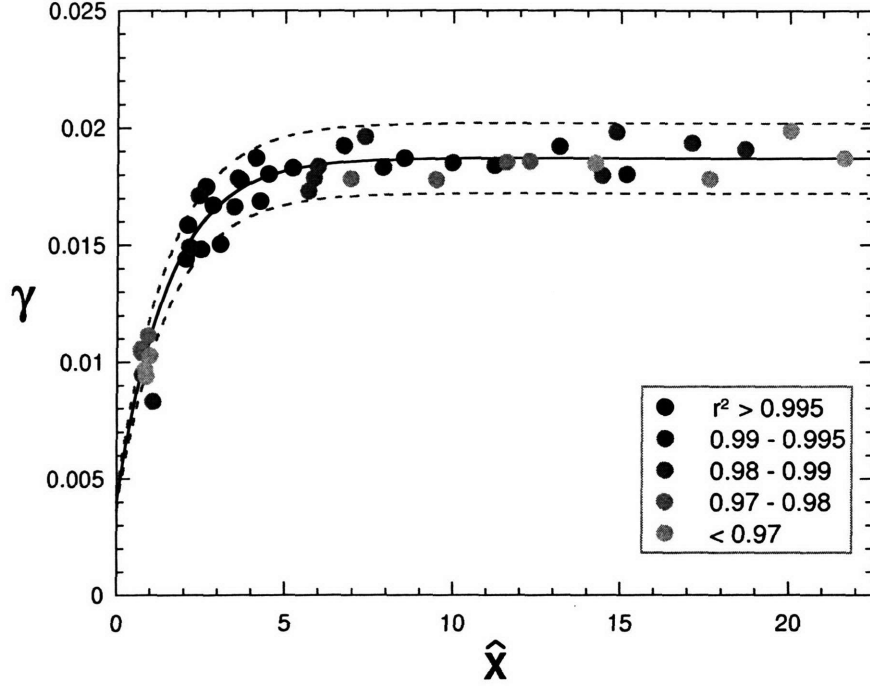


Figure 3-13: The longitudinal variation of normalized best-fit diffusivity, $\gamma = \overline{D}/\Delta U t_{ml}$. Near the source, the diffusivity is low compared to that in the far-field. The darkness of each point is proportional to the goodness of fit (r^2) between the experimental and model concentration profiles. A model that assumes a vertically uniform diffusivity above z_1 generally predicts the shape of the concentration profile well ($\overline{r^2} > 0.98$).

as shown in Figure 3-13. This figure clearly shows that the diffusivity near the source is much less than that in the far-field. However, the plume's 'memory' of the reduced near-field diffusivities is erased by $\hat{X} \approx 8$. The mean values of \overline{D} in the far-field (i.e. $\hat{X} \gtrsim 8$) for each run are detailed in Table 3.1. The rapid rate of mixing associated with the vortices is highlighted by the ratio of \overline{D} to D_e , which ranges from 15 – 32 in this study.

In a flow with vertically uniform velocity and diffusivity, it can be easily shown that the relationship between $\overline{D}(x)$ (the effective constant diffusivity between the source and position x) and $D(x)$ (the local diffusivity at x) is given by

$$D(x) = \frac{\partial}{\partial x} (\overline{D}x). \quad (3.18)$$

The velocity shear and step-profile of diffusivity in these flows were shown by model

runs not to impact this relationship. Application of (3.18) to the data in Figure 3-13 shows that the local diffusivity is constant ($0.019\Delta U t_{ml}$, $\pm 15\%$) beyond $\hat{X} \approx 2.5$. The experimental concentration profiles reveal that $\hat{X} \approx 2.5$ is almost exactly the location at which the plume has grown to encompass the entire shear layer. For example, Position 2 in Run E (Figure 3-14) is located at $\hat{X} = 2.2$; at this position, the plume extends almost completely to the top of the shear layer ($z_2 \approx 38$ cm). These observations lend weight to the concept of a diffusivity that is dependent upon the plume size. In the near-field ($\hat{X} < 2.5$), the plume is smaller than the mixing (vortex) structures and the diffusivity is low. Once the plume reaches the size of the vortices, the diffusivity is maintained at a constant, maximum value.

In Figure 3-13, the darkness of the markers is proportional to the goodness of fit (r^2) of the modeled concentration profile to that observed. To focus upon the accuracy of the assumption of a uniform diffusivity above $z = z_1$, the goodness of fit was evaluated in the range $z_1 < z < H$ (which comprised 42 – 45 data points). The mean value of r^2 was more than 0.98, indicating that a constant diffusivity above $z = z_1$ is a suitable approximation. This is further demonstrated in Figure 3-14, which compares the experimental and modeled concentration profiles of Run E. The shape of the profile is predicted well at all locations. Interestingly, the model overpredicts the concentration gradients below z_1 in the far-field. This suggests that at the same flow speed, the diffusivity below the shear layer is greater than that in equally dense emergent arrays. The apparently enhanced diffusivity in this region is due possibly to secondary vertical flow behind individual canopy elements in the small boundary layer near the bed (Nepf and Koch [43]). The measurements of Nepf *et al.* [45] were centered at mid-depth and therefore affected little by this vertical flow.

3.5 Conclusion

Through the absorbance-concentration relationship of the Beer-Lambert Law, digital imaging has been used to provide high-resolution concentration profiles of scalar plumes in vegetated flows. It has been clearly shown that the coherent vortices of

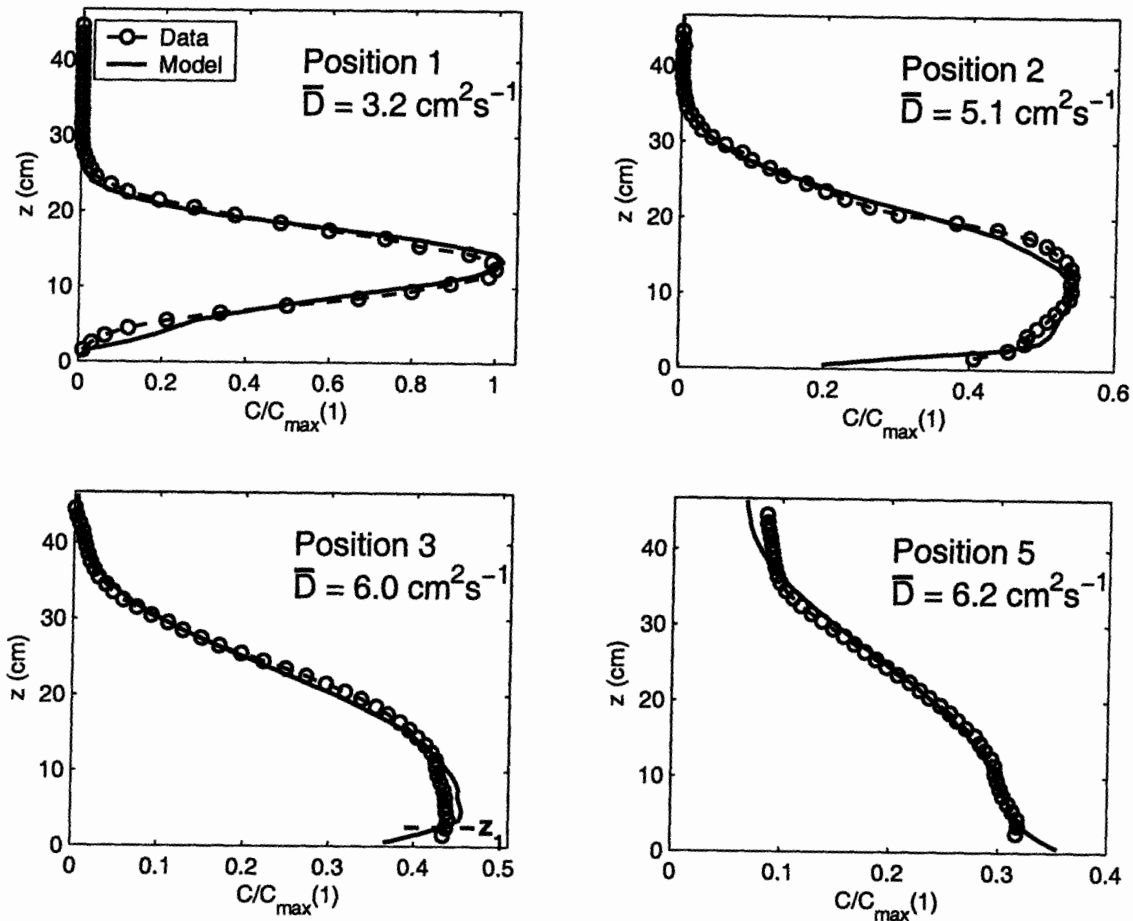


Figure 3-14: The good agreement between the experimental concentration profiles of Run E and those predicted by the LPTM. Both profiles have been normalized by the maximum observed concentration at Position 1. The experimental profiles exhibit smaller gradients below the shear layer ($z_1 < 2.5 \text{ cm}$) in the far-field, suggesting that the diffusivity is actually greater than D_e ($0.20 \text{ cm}^2 \text{ s}^{-1}$) in this zone.

a vegetated shear layer dominate vertical transport, such that transport is easily characterized by properties of the shear layer. Firstly, using a two-box model, the exchange velocity between the canopy and overlying water is shown to scale upon the total shear ($k \sim \Delta U$). Secondly, using a flux-gradient model, the vertical turbulent diffusivity scales upon the shear and size of the layer ($D_{tz} \sim \Delta U t_{ml}$). Our results suggest that plume size is dictated predominantly by \hat{X} , a dimensionless distance that scales upon the number of vortex rotations experienced by the plume. The turbulent diffusivity depends upon the size of the plume (and thus \hat{X}), such that the rate of plume growth is lower near the source. In the far-field ($\hat{X} \gtrsim 8$), mass is mixed more than twice as rapidly as momentum. Finally, images of dye injection demonstrate the lateral variability of the vortex structure, which causes transport to be instantaneously nonuniform in the lateral direction.

Chapter 4

The impact of vegetation on transport in open channels

To fully describe the impact of submerged vegetation on the flow and transport in an open channel, a direct comparison between vegetated and unvegetated shear flows is required. Consider two uniform, infinitely-wide channels, both with a flow depth (H) of 46.7 cm. The bed of one channel is unvegetated, whilst the other contains a vegetation canopy that is 13.9 cm tall and occupies a volumetric fraction (P) of 4% (i.e. the canopy of Run H (Table 2.1)). In this section, I contrast the vertical profiles of mean velocity (U) and vertical diffusivity (D_{tz}) as well as the coefficients of longitudinal dispersion (K_x) in the two channels. Conditions in the unvegetated channel will be varied to match, separately, the depth-averaged velocity ($\langle U \rangle = 8.8$ cm/s) and surface slope ($S = -dH/dx = 1.0 \times 10^{-4}$) of the vegetated channel.

4.1 Vertical profiles of velocity and diffusivity

The flow in an archetypal unvegetated channel is that of a turbulent boundary layer. Such a flow has been comprehensively studied, such that the vertical profiles of velocity and turbulent diffusivity, required elements in the evaluation of K_x , are well

known. Firstly, in the logarithmic region of a turbulent boundary layer

$$U(z) = \frac{u_*}{\kappa} \ln \left(\frac{z}{k_s} \right) + u_* C \left(\frac{u_* k_s}{\nu} \right), \quad (4.1)$$

where C is a constant equal to 8.5 for fully rough turbulent flow (i.e. for $u_* k_s / \nu > 70$, Nezu and Nakagawa [47], p. 27). In (4.1), κ ($= 0.41$) is the von Karman constant, k_s is the equivalent sand grain (Nikuradse) roughness and u_* ($= \sqrt{gHS}$) is the friction velocity. The Nikuradse roughness in this channel is given a typical value of 0.5 cm. By integration of (4.1), the mean channel velocity is given by

$$\langle U \rangle = \frac{1}{H} \int_0^H U(z) dz = \frac{u_*}{\kappa} \left(\ln \left(\frac{H}{k_s} \right) - 1 \right) + u_* C. \quad (4.2)$$

Secondly, in this logarithmic region, the vertical eddy viscosity has the form

$$\nu_{tz} = \kappa u_* z \left(1 - \frac{z}{H} \right) \quad (4.3)$$

(Fischer *et al.* [17], p. 106). In a boundary layer, not only is the vertical mass diffusivity not equal to the vertical eddy viscosity, but the turbulent Schmidt number ($Sc_t = \nu_{tz} / D_{tz}$) exhibits considerable vertical variability. This ratio takes its maximum value (close to unity) at $z/H \approx 0.3$, and tends towards zero as the bed is approached (Koeltzsch [32]). However, to broadly compare diffusivity in vegetated and unvegetated channels, I will assume that Sc_t uniformly takes its mean value of 0.8, which (to within 25%) is valid for $0.1 < z/H < 0.9$. Under this assumption,

$$D_{tz} \approx 0.5 u_* z \left(1 - \frac{z}{H} \right) \quad (4.4)$$

in the unvegetated channel. In this analysis, I have assumed that the logarithmic layer extends throughout the entire flow depth; real profiles of $U(z)$ and $\nu_{tz}(z)$ deviate very slightly from the expressions in (4.1) and (4.3) (refer to Nezu and Nakagawa [47], pp. 27, 66).

The profiles of velocity and vertical diffusivity in the two archetypal channels are

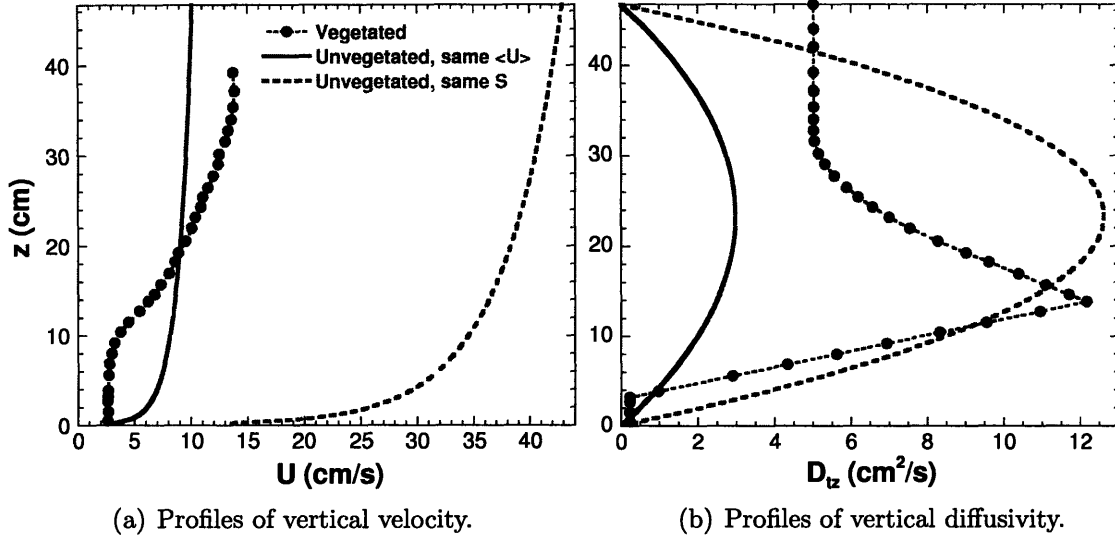


Figure 4-1: Comparison of the profiles of velocity and vertical diffusivity in the two archetypal channels. In the unvegetated channel, two conditions have been simulated. In the first, the mean velocity, $\langle U \rangle$, of the vegetated channel is matched. In the second, the slope, S , is matched. As the free surface is approached, the diffusivity above the vegetated shear layer is expected to decrease. However, as the form of D_{tz} is unknown in this region, a constant value (equal to that seen in the uppermost 20% of the shear layer) is assumed for simplicity.

compared in Figure 4-1. The flow conditions in the vegetated channel are exactly that of Run H. In the wake zone of the vegetated channel (i.e. $z < z_1$), the diffusivity (D_w) is assumed to be the same as that in an equally dense emergent cylinder array (D_e from Table 3.1). In the shear layer, the best-fit profile of the vertical diffusivity data ($D_{tz} = f(\Delta U t_{ml}, z^*)$) was taken from Figure 3-11. Above the shear layer, the diffusivity is assumed to be constant, taking the value seen in the uppermost 20% of the shear layer (i.e. $D_{tz} = 0.013 \Delta U t_{ml}$). The free surface will undoubtedly begin to influence turbulent length scales and diffusivity as it is approached. However, the interplay between the free surface and the secondary circulation presumed to exist above vegetated shear layers (§2.3) is unknown. For simplicity, therefore, I will assume that the diffusivity above the shear layer (D_a) is uniform. In fact, the region above the shear layer contributes little to dispersion in the experimental flows; a 20% change in D_a causes only a 0.2 – 2% change in K_x . As seen in Figure 4-1(a), the baffling effect of submerged vegetation is such that the mean flow in the unvegetated channel

(with matched slope) is more than four times that in its vegetated counterpart. In Figure 4-1(b), the efficiency of vertical transport by the coherent vortex structures is highlighted. For the same mean flow, the vertical diffusivity in the mixing layer of the vegetated channel is roughly three times that in the boundary layer of the unvegetated channel.

4.2 Longitudinal dispersion

The coefficient of longitudinal dispersion (K_x) in a flow dominated by vertical shear is given by

$$K_x = -\frac{1}{H} \int_0^H u'' \int_0^z \frac{1}{D_{tz}} \int_0^z u'' dz dz dz \quad (4.5)$$

(Fischer *et al.* [17], p. 91), where u'' represents the spatial deviation from the mean channel velocity. In this section, I evaluate the dispersion coefficients of the experimental flows, deduce some simple scaling relationships for dispersion in vegetated shear flows and contrast dispersion in vegetated and unvegetated channels.

4.2.1 Unvegetated channels

Under the assumption that $Sc_t = 1$ (i.e. $\nu_{tz} = D_{tz}$), substitution of (4.1) and (4.3) into (4.5) yields Elder's famous result of $K_x = 5.93u_*H$ (Fischer *et al.* [17], p. 92). However, as shown by Chatwin [9], Elder's method suffers from two limitations. Firstly, the eddy diffusivity in a turbulent boundary layer is, on average, approximately 20% greater than the eddy viscosity (Koeltzsch [32]). Secondly, omission of the effect of the viscous sublayer on dispersion results in roughly a 20% underprediction of K_x (Chatwin [9]). These two effects approximately cancel each other such that it is reasonable to say that in an infinitely wide channel,

$$K_x \approx 6u_*H. \quad (4.6)$$

This value is comparable to dispersion coefficients observed in very wide ($w_f/H \sim O(10)$), rough-bottomed laboratory channels (Fischer [18]).

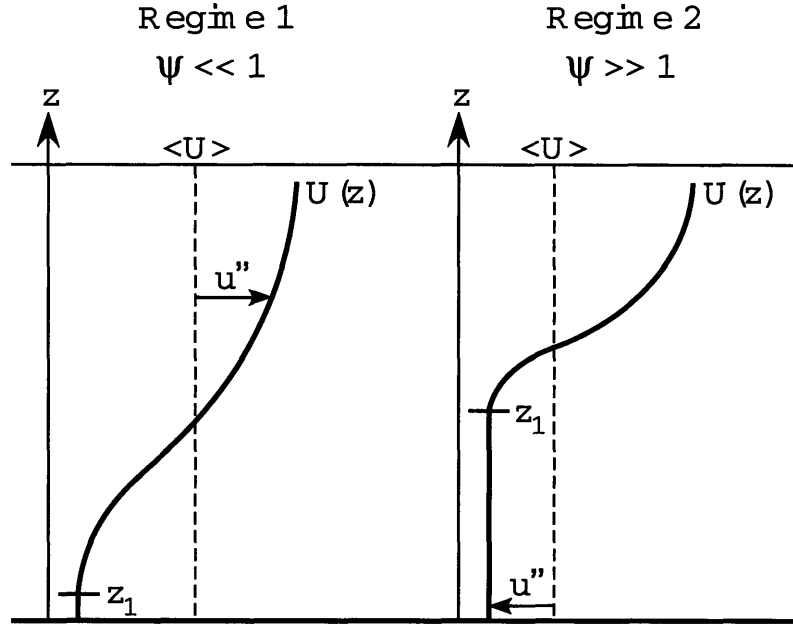


Figure 4-2: The two limiting regimes of longitudinal dispersion in vegetated shear flows. In Regime 1, dispersion is dictated by the shear layer. In Regime 2, detention within the wake zone ($z < z_1$) dominates dispersion.

4.2.2 Vegetated channels

I propose that there are two limiting regimes of longitudinal dispersion in vegetated shear flows. In the first regime, dispersion is dominated by velocity gradients across the shear layer (Figure 4-2). In the second regime, dispersion is dominated by detention in the wake zone, a region with high u'' and low diffusivity. In Regime 1, $u'' \sim \Delta U$ and $D_{tz} \sim \Delta U t_{ml}$ such that from (4.5),

$$K_{x1} \sim \frac{\Delta U H^2}{t_{ml}}. \quad (4.7)$$

In Regime 2, the triple integral in (4.5) is significant only in the range $0 \leq z \leq z_1$. In this zone, $u'' = \langle U \rangle - U_1$ and $D_{tz} = D_w$. Thus, evaluation of (4.5) in the limit of the second regime exactly yields

$$K_{x2} = \frac{z_1^3 (\langle U \rangle - U_1)^2}{3D_w H}. \quad (4.8)$$

The transition between these two regimes will depend upon the scaled ratio of their dispersion coefficients,

$$\psi = \left(\frac{z_1}{H}\right)^3 \left[\frac{\Delta U t_{ml}}{D_w}\right] \left\{\frac{\langle U \rangle - U_1}{\Delta U}\right\}^2 \sim \frac{K_{x2}}{K_{x1}}. \quad (4.9)$$

The third bracketed term in (4.9) is a shape factor of the velocity profile, similar to that in the expression for the stability parameter, Ω (2.9). For flows in which $t_{ml} \gg z_1$, this factor will be approximately 1/4. Under the assumption that the scaling coefficient in (4.7) is of $O(1)$, the second dispersion regime will dominate if $\psi \gg O(1)$. Conversely, if $\psi \ll O(1)$, shear layer dispersion will dominate. Note that this analysis is valid only for flows in which the shear layer and wake zone comprise the majority of the flow depth; in these experiments, $0.6 \lesssim z_2/H \lesssim 0.8$.

For the eleven flow scenarios detailed in Table 2.1, the velocity profile, $U(z)$, and the profile of vertical diffusivity, $D_{tz}(z)$, were employed to evaluate K_x from (4.5). The best-fit profile of the vertical diffusivity data in Figure 3-11 was used for each run, as it was in Figure 4-1(b). As in Elder's analysis, I do not consider the viscous sublayer (nor the small, modified boundary layer) near the bed. The calculated values of K_x are shown in Figure 4-3 as a function of ψ . The values of K_x are normalized by $\Delta U H^2/t_{ml}$, according to the scaling of the dispersion coefficient in the first regime (4.7). The collapse of this data is good, and shows that

$$\lim_{\psi \rightarrow 0} K_x \approx 0.5 \frac{\Delta U H^2}{t_{ml}} (\pm 15\%). \quad (4.10)$$

This approximation holds true for $\psi \lesssim 0.1$. The spread of the data ($\pm 15\%$) at low ψ equates roughly with the uncertainty in the values of K_x , estimated by considering the lateral nonuniformity of the velocity profile (see, e.g., Figure 2-3) and the spread of the vertical diffusivity data (Figure 3-11). Above $\psi \approx 0.1$, detention in the wake zone appears to augment dispersion.

To examine the behavior of K_x as a function of ψ , the values of both D_w and z_1 were manipulated numerically in Run H. In the manipulation of the latter, the location of the bed was artificially shifted downwards/upwards to increase/decrease

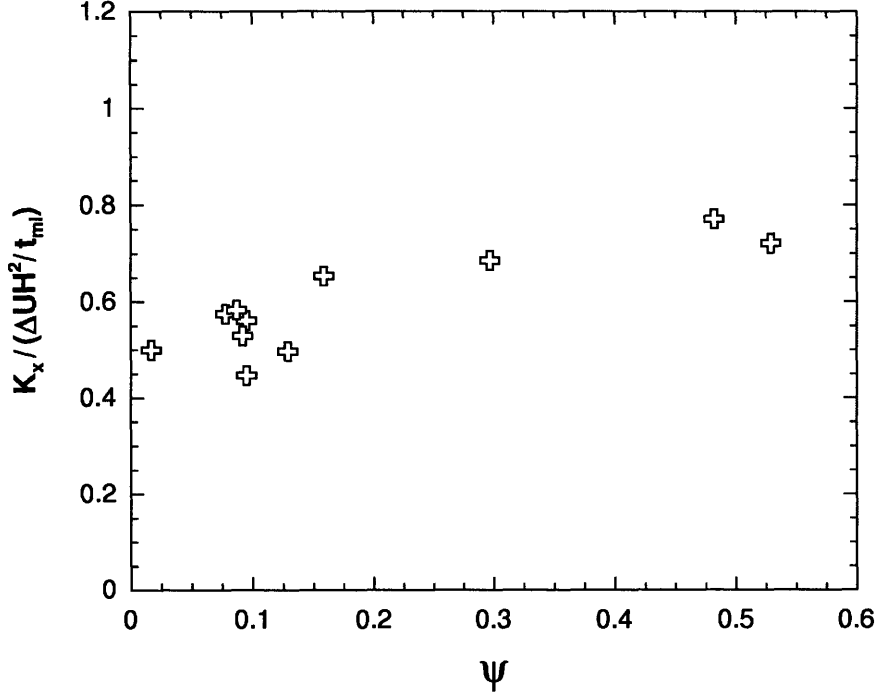


Figure 4-3: The values of the dispersion coefficient (K_x), calculated by considering vertical shear only, as a function of ψ for the eleven experimental runs. The dispersion coefficient is normalized by $\Delta UH^2/t_{ml}$, the appropriate scaling in the first dispersion regime. The collapse of the data as $\psi \rightarrow 0$ is good, validating this scaling relationship. The estimated uncertainty in the values of K_x is roughly 15%.

wake zone depth. Figure 4-4 shows the resultant curves of $K_x^*(\psi) = K_x/(\Delta UH^2/t_{ml})$ (the appropriate normalization in the first regime) and $K_x^{**}(\psi) = K_x/(z_1^3(\langle U \rangle - U_1)^2/D_w H)$ (the appropriate normalization in the second regime). In this figure, the solid markers represent the manipulation of D_w , while the unfilled markers represent the manipulation of z_1 . The limit of the second dispersion regime is approached to within 15% by $\psi \approx 10$. Within the range $0.1 < \psi < 10$, therefore, both the shear layer and wake zone detention contribute to longitudinal dispersion. Furthermore, Figure 4-4 demonstrates that K_x is a unique function of ψ , as the behaviour of $K_x(\psi)$ is independent of whether D_w or z_1 is varied.

For these experimental flows, $\psi_{\max} \approx 0.5$, meaning that detention in the wake zone is not expected to dominate dispersion. However, real vegetated shear flows may have $\psi \sim O(10)$ such that the limit of the second dispersion regime is approached. This is likely to be the case for flows with a low degree of submergence (H/h), in which

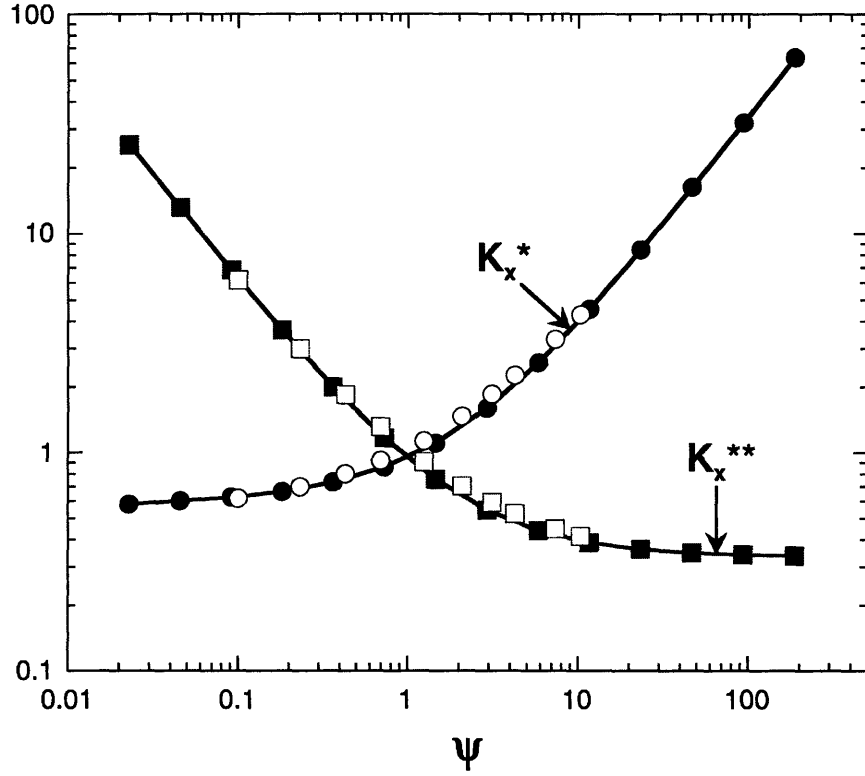


Figure 4-4: The behavior of $K_x^*(\psi) = K_x/(\Delta U H^2/t_{ml})$ and $K_x^{**}(\psi) = K_x/(z_1^3(\langle U \rangle - U_1)^2/D_w H)$ in Run H as D_w (solid markers) and z_1 (unfilled markers) are varied numerically. The agreement between the solid and unfilled markers indicates that K_x is a unique function of ψ . Over the range $0.1 < \psi < 10$, both the shear layer and the wake zone contribute to dispersion.

the free surface may restrict the size of the shear layer. For example, consider the estuarine eelgrass meadow studied by Grizzle *et al.* [27]. Assuming a typical value of eelgrass meadow density ($P = 2\%$, Chandler *et al.* [8]) and that $D_w = D_e$ below the shear layer, I estimate from the presented velocity profile that ψ is as high as 40 – 50 an hour after low tide (Figure 1B in that paper). Note that as $H/h \rightarrow 1$, the shear across the top of the canopy ceases to be the dominant feature of the flow and dispersion is driven by stem-scale heterogeneity. For $Re_d \sim O(100)$, this wake-driven dispersion is of the order of $U_1 d$ (White and Nepf [65]), typically several orders of magnitude lower than the dispersion coefficients in Regimes 1 and 2.

As discussed previously, the conventional scaling of longitudinal dispersion in unvegetated channels is on the flow depth and friction velocity ($K_x/u_* H \approx 6$, (4.6)).

Indeed, the dispersion coefficients in these experiments are of a comparable magnitude when normalized in this fashion ($3.1 \leq K_x/u_*H \leq 7.6$). This analysis demonstrates, however, that this is not the appropriate scaling of K_x in vegetated channels. To verify this, let us consider the limit of the first dispersion regime (i.e. negligible trapping in the wake zone). For a traditional scaling of $K_x \sim u_*H$ to be robust, there must be an approximately constant relationship between u_*H and $\Delta U H^2/t_{ml}$ (the true scaling of dispersion in the first regime of vegetated shear flows). That is, the ratio

$$\chi = \frac{u_* t_{ml}}{\Delta U H} \quad (4.11)$$

should be relatively independent of canopy and flow variables. Although $u_*/\Delta U$ is remarkably constant (0.21 ± 0.02), the ratio t_{ml}/H is not necessarily so. This ratio can range from unity down to (at least) 0.5, the lowest value observed in these experiments, while still maintaining the inflectional shear layer as the dominant dynamic feature of the flow. Significant trapping in the wake zone will cause the u_*H scaling to become even less robust. Thus, there cannot be a general comparison of dispersion in vegetated and unvegetated channels. For our archetypal channels, the values of K_x are $470 \text{ cm}^2\text{s}^{-1}$ (vegetated), $610 \text{ cm}^2\text{s}^{-1}$ (unvegetated, same S) and $140 \text{ cm}^2\text{s}^{-1}$ (unvegetated, same $\langle U \rangle$). Despite the baffled flow of the vegetated channel relative to the unvegetated channel of the same slope, the strong shear generated by the canopy elevates the dispersion to a level comparable to that in the bare channel.

It is important to note that this dispersion analysis considers only the vertical velocity shear. Even in an infinitely wide channel, the lateral heterogeneity of vegetated shear flows on the scales of both the vortex (as demonstrated in §3.3) and the stem wake may augment longitudinal dispersion. Further experiments are required to determine the contribution of this inherent lateral shear to dispersion. Furthermore, it has been shown that Elder's result is not quantitatively applicable to real streams. Lateral nonuniformities such as bends and dead zones can dramatically increase dispersion (Fischer [18]). The relative impacts of nonuniformities in vegetated and unvegetated channels remains unexplored.

4.3 Conclusion

Submerged vegetation has a pronounced impact on the structure of mixing in open channels. The traditional u_*H scaling of both the vertical turbulent diffusivity and longitudinal dispersion is shown to be invalid in vegetated channels, as these processes depend heavily upon characteristics of the vegetated shear layer. The extent of vortex penetration into the canopy is critically important, as it divides the canopy into an upper zone with rapid, vortex-driven vertical transport and a lower zone where mixing occurs on the much smaller scale of the stem wakes. In shear flows over sufficiently dense canopies, the depth of this lower zone will dictate both the timescale for vertical mixing and the rate of longitudinal dispersion.

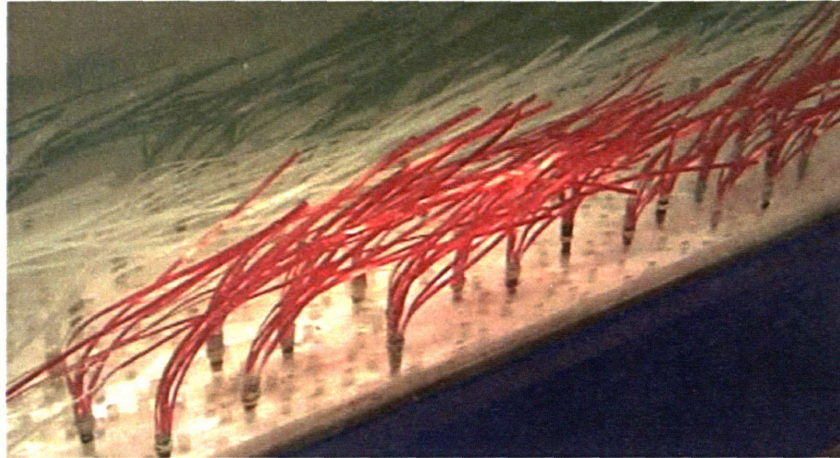
Chapter 5

The effect of plant flexibility on vertical transport

In response to steady currents, flexible submerged aquatic vegetation may exhibit a progressive, synchronous, large-amplitude waving (termed *monami* by Ackerman and Okubo [1]). The *monami* is a response to the strong oscillations in streamwise velocity associated with the passage of the coherent vortex structures of the vegetated shear layer (Ghisalberti and Nepf [24]). The *monami* is triggered when the flow velocity increases above a threshold value. This threshold increases with decreasing flow depth and increasing plant rigidity (Ghisalberti [25]). To determine the impact of plant flexibility on vegetated shear flows, several experiments were conducted with a flexible canopy in the laboratory flume.

5.1 Experimental methods

The experimental configuration from Chapter 2 (see Figure 2-2), including the constant flow depth of 46.7 cm, was retained for these experiments, with a flexible model canopy substituted for the rigid dowels (Figure 5-1(a)). The flexible model vegetation was designed to mimic eelgrass (*Zostera marina*). Each model plant consisted of a stem region and six thin blades, based on the typical morphology of Massachusetts Bay eelgrass (Chandler *et al.* [8]). Wooden dowels (0.63 cm in diameter, 1.5 cm in



(a) The flexible model canopy, colored after the experiments to highlight the lateral subchannels in the flow.



(b) The experimental configuration used to simultaneously measure the flow velocity and plant motion. The heights of three colored blades on one plant were monitored through the capture of digital video and subsequent image analysis. The ADV probe was positioned approximately 3 cm upstream from the front of the plant. The corresponding time in the velocity record (505 s in this case) was clearly visible in each frame.

Figure 5-1: The flexible model vegetation of this study.

height) were used to mimic the eelgrass stem. Model blades were cut from low-density polyethylene film ($\rho_s = 920 \text{ kgm}^{-3}$) with a modulus of elasticity, E , of $3.0 \times 10^8 \text{ Pa}$. The height of the blades was 20.3 cm, their width (w_b) 3.8 mm, and their thickness (t) 0.20 mm. This blade thickness was specifically chosen to ensure that the waving of the model plants accurately mimicked the motion of real seagrass. As described in Ghisalberti [25], the motion of the plants is dictated by the ratio of blade buoyancy to blade rigidity. A scaled form of this ratio is given by the parameter

$$\lambda = \frac{(\rho_w - \rho_s) h^3}{Et^2}. \quad (5.1)$$

From my observations in Ghisalberti [25], model vegetation exhibits the most realistic motion when $\lambda \approx 0.055 \text{ s}^2\text{m}^{-1}$, the value taken by these model plants. The total canopy length was 6.5 m and the density of the meadow was fixed at 230 plants/ m^2 . Assuming that each blade orients itself normal to the flow, the (theoretical) density of the canopy was $a = 0.052 \text{ cm}^{-1}$. The average undeflected height of the plants was $20.5 \pm 1.0 \text{ cm}$, the variability arising from differing degrees of vertical extension of each blade. Note that this nonuniformity, which mimics the variability of real seagrass meadows, is desired. The spatial and temporal variability in the height of a flexible canopy, through both this nonuniformity and the *monami*, distinguishes flexible canopies from the ideal, rigid model canopies examined in Chapter 2.

Similarly to the rigid canopy experiments, vertical profiles of ten-minute velocity (u, v, w) records were taken by four 3-D acoustic Doppler velocimeters (ADV) in each of six flow scenarios. Velocity statistics from the four probes, which were separated laterally by 6 cm, were averaged to obtain the spatial mean, as discussed in §2.2. As in the experiments of Chapter 2, all velocity profiles were measured at $x = 6.0 \text{ m}$, by which point fully-developed conditions had been established. To allow probe access, a 12-cm-long ($= 1.8\Delta S$) slice of plants was removed across the channel. Digital video camera footage was used to determine the maximum plant height (h_{max}) and *monami* amplitude (A_w) for all runs. The waving amplitude, estimated from the footage as the average vertical excursion of blades during a *monami* cycle, was as large as $0.28h_{max}$,

Table 5.1: Key parameters of the six experimental flows with flexible vegetation.

Run	F1	F2	F3	F4	F5	F6
Q ($\times 10^{-2}$ cm ³ s ⁻¹)	28	47	66	87	114	148
ΔU (cms ⁻¹)	2.9	4.6	6.2	7.8	9.7	12.3
$\Delta U/U_{h_{max}}$	1.7	1.6	1.7	1.8	1.7	1.6
U_1 (cms ⁻¹)	0.31	0.55	0.72	0.95	1.4	2.2
h_{max} (± 0.2 cm)	21.5	21.3	20.0	18.6	17.0	15.5
A_w (cm, $\pm 25\%$) [†]	-	-	2.7	3.5	4.1	4.4

[†] Dashes indicate the absence of an observable *monami* at low flow speeds.

as reported in Table 5.1.

To begin to characterize the impact of plant flexibility on the flow, the oscillatory nature of both the velocity field and the plant height must be considered. Time series of $\overline{u'w'}$ in vegetated flows show strong sweeps and weak ejections that are brief and strongly periodic (Figure 1-1). That is, the regions of active vertical transport within the vortex are quite localized. Therefore, during moments of rapid transport, the canopy geometry may be significantly different to its temporally averaged condition. As a preliminary investigation of this coupled oscillation, the flow velocity and plant motion were measured simultaneously. Three blades on one plant, placed in the middle of the flume in the flow conditions of Run F6 (Table 5.1), were colored red, green and blue (respectively). A digital video camera captured the motion of each of these three blades, as shown in Figure 5-1(b). While the plant motion was filmed, 15-minute velocity records (at heights separated by 2 cm) were taken by a Sontek MicroADV aligned laterally with the plant but displaced 3 cm upstream. Synchronization of the video footage and velocity records was achieved by placing the monitor of the computer used to record the ADV data directly across the flume from the camera. The timing of the velocity record was thereby made visible to the video camera (Figure 5-1(b)). Frames were taken from the digital footage at 1 Hz. Velocity data in a half-second window (i.e. ± 0.25 s) around the time of each frame were averaged to provide the instantaneous flow conditions. The height of each blade was detected manually using MATLAB's Image Processing Toolbox. Note that MATLAB's edge detection algorithm was initially configured to determine blade height but mistakenly

identified the blades in roughly 2-5% of the frames, distorting the results.

5.2 Mixing layer analogy

The results of these experiments suggest that flow over flexible, waving vegetation more closely resembles a mixing layer than flow over rigid vegetation. To demonstrate this, Figure 5-2 compares the profiles of mean velocity and Reynolds stress in (i) a mixing layer, (ii) shear flow over a rigid canopy, (iii) shear flow over a still, flexible canopy and (iv) shear flow over a waving, flexible canopy. The vertical colored bars in this figure represent the average height ranges of each canopy, considering both the *monami* and inherent spatial nonuniformity of the flexible canopy. To facilitate comparison, all variables have been normalized as follows:

$$z^* = \frac{z - z_1}{t_{ml}}, U^* = \frac{U - \bar{U}}{\Delta U}, RS^* = \frac{\overline{u'w'}}{\Delta U^2}, \quad (5.2)$$

where $\bar{U} = 0.5(U_1 + U_2)$. The classical hyperbolic tangent velocity profile of a mixing layer has the form

$$U^* = 0.5 \tanh(3.85(z^* - 0.5)) \quad (5.3)$$

(Ghisalberti and Nepf [24]), where the ratio of the mixing layer thickness (t_{ml}) to the momentum thickness (θ) is assumed to be 7.7 (the mean value for the rigid canopy profiles in Chapter 2). The Reynolds stress profile in a mixing layer is taken from Rogers and Moser [53]. The rigid canopy data represent an average of the flow statistics of Runs H, I and J (Table 2.1, $a = 8.0 \text{ m}^{-1}$, $\Delta U/U_h \approx 1.8$). Likewise, the profiles for flow over a still, flexible canopy are taken from Runs F1 and F2 (Table 5.1, $a = 5.2 \text{ m}^{-1}$, $\Delta U/U_h \approx 1.6$) and the waving canopy data from Runs F3, F4, F5 and F6 ($a = 5.2 \text{ m}^{-1}$, $\Delta U/U_h \approx 1.7$). The velocity profiles of the three vegetated shear layers display a similar level of asymmetry, with the zero-crossing of U^* occurring at $z^* \approx 0.4$ in all cases. However, for a given shear, the layer-averaged momentum transport (i.e. $\int_0^1 [-\overline{u'w'}/(\Delta U)^2] dz^*$) depends heavily upon the temporal and spatial variability of the canopy height. With increasing canopy height variability, the layer-

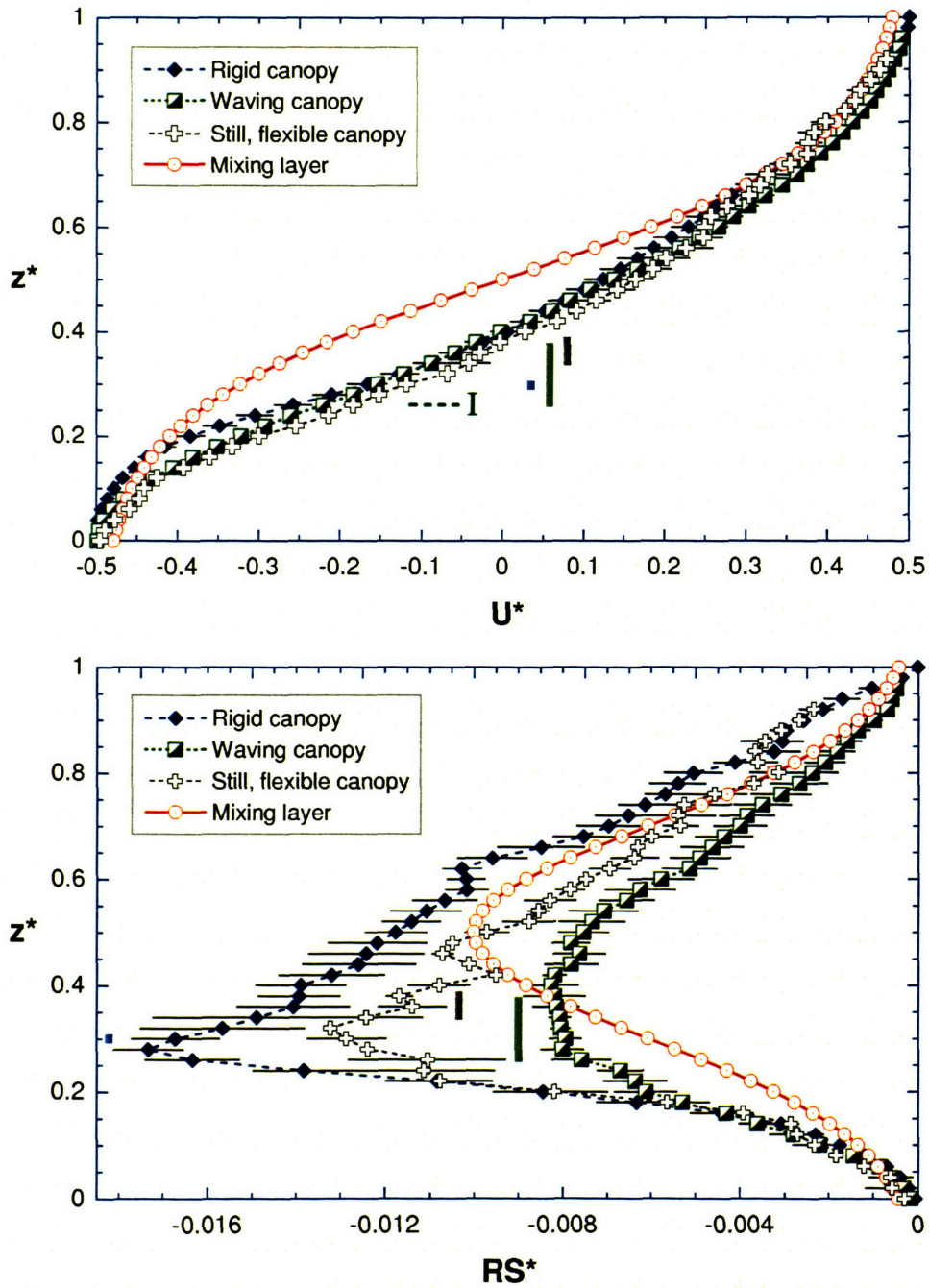


Figure 5-2: Profiles of mean velocity and Reynolds stress in (i) a mixing layer (Rogers and Moser [53]), (ii) shear flow over a rigid canopy (Runs H, I and J in Table 2.1), (iii) shear flow over a still, flexible canopy (Runs F1 and F2) and (iv) shear flow over a waving canopy (Runs F3, F4, F5 and F6). All variables have been normalized as in (5.2). The colored vertical bars represent the average height ranges of each canopy. The inflection point (I) for the flows over the rigid and waving canopies lies just below the top of the vegetation. The horizontal bars represent the variability between runs.

averaged transport increases from 0.0045 for the waving canopy to 0.0063 for the still, flexible canopy to 0.0077 for the rigid canopy. In mixing layers, this parameter takes a value (≈ 0.005) similar to that seen in the experimental flows over a waving canopy. In contrast to the rigidly obstructed shear layers (for which the canopy top is located at $z^* = 0.3$), the shear layers generated by a waving canopy have a region of approximately constant stress that spans the zone over which the canopy height oscillates ($z^* \approx 0.26 - 0.38$). That is, as the variability in the canopy height increases, both the normalized momentum transport and the sharpness of the stress peak near the top of the canopy decrease.

In the passage frequency of the vortices, unobstructed mixing layers ($St = 0.032$) and shear layers generated by waving vegetation ($St \approx 0.032$) further distinguish themselves from rigidly obstructed shear layers ($St \approx 0.037$). The importance of plant flexibility is also suggested by the difference in the observed ratios of turbulent velocities in rigidly ($u_{rms}/w_{rms} = 1.4$) and flexibly obstructed shear layers (1.7). This dependence upon plant flexibility may relate to the anisotropic dissipation of vortex energy by rigid canopies. Due to the geometry of the rigid canopies, it is expected that horizontal turbulent fluctuations are dissipated more effectively than vertical fluctuations. The deflected flexible canopy offers significantly more frontal area to vertical flow, thereby decreasing w_{rms} relative to u_{rms} . This isotropy, or lack thereof, impacts the observed Strouhal number. The nominal (observed) Strouhal number ($St = f_v \theta / \bar{U}$, where θ is the momentum thickness of the shear layer) is simply a scaled version of the more pertinent form ($St' = f_v \Lambda / U_v = 1$) that relates the frequency of vortex passage (f_v) to their convective speed (U_v) and longitudinal spacing (Λ). The relationship between these two forms of the Strouhal number is given by

$$St = \frac{f_v \theta}{\bar{U}} = St' \phi \left(\frac{\theta}{t_{ml}} \right) \left(\frac{U_v}{\bar{U}} \right). \quad (5.4)$$

Here, ϕ represents the aspect ratio of the vortex street ($\phi = t_{ml} / \Lambda$), where t_{ml} roughly describes the height of the vortices. To simplify (5.4), I will assume that the ratio of the momentum thickness to the shear layer thickness is a constant. This assumption

is supported by the fact that θ/t_{ml} appears to be independent of canopy density or flexibility, taking a value of 0.13 ± 0.01 across all rigid canopy runs in Chapter 2 and the three vegetated velocity profiles in Figure 5-2. Furthermore, for the model canopy of Ghisalberti and Nepf [24], the relationship between the vortex velocity and the mean shear layer velocity is a function of the ratio of the mixing layer thickness to the plant height (i.e. $U_v/\bar{U} = f(t_{ml}/h) \approx 1 + [t_{ml}/9h]$). With these simplifications, (5.4) becomes

$$St \approx 0.13\phi f(t_{ml}/h). \quad (5.5)$$

This relationship is consistent with the observation of higher values of St in rigidly obstructed shear layers. By dissipating (relatively) less vertical turbulent energy, rigid canopies generate vortices with a greater aspect ratio, and thus a greater nominal Strouhal number. Consider Runs H (rigid) and F5 (flexible), for which $(t_{ml}/h) \approx 2.4$. From (5.5), the aspect ratio of the vortex street is approximately 0.22 in Run H and 0.19 in Run F5, demonstrating the elongated geometry of the vortices in vegetated shear flows.

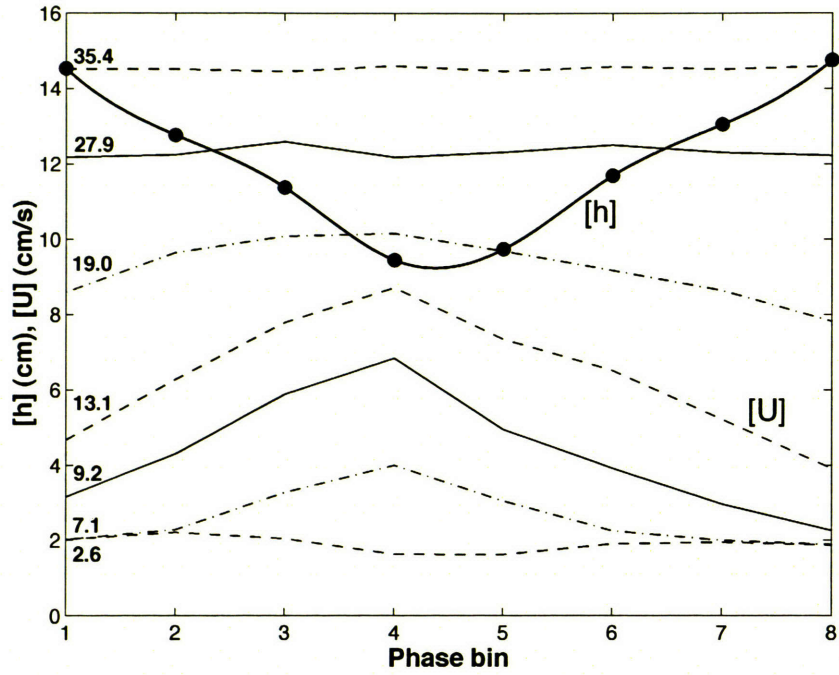
5.3 Correlation between the flow field and plant motion

When placed in the flow, the three colored blades of the test plant (Figure 5-1(b)) splayed out, with an estimated lateral separation of roughly 7 cm between adjacent tips. As a result of this splay and the lateral subchannels that are generated in the flow, the motions of the blades were not perfectly correlated. The heights of the outer blades (blue, green) correlated mildly with the height of the inner, red blade ($r^2 = 0.51$ and 0.39 , respectively) but not at all with each other ($r^2 = 0.10$). Midway during the experiment, the blades aligned themselves so as to be one above the other during five velocity records. During this period, these correlations increased dramatically to 0.84, 0.83 and 0.97, respectively, further highlighting the lateral nonuniformity in the flow. In this analysis, the plant height is taken as the mean of the heights of the three

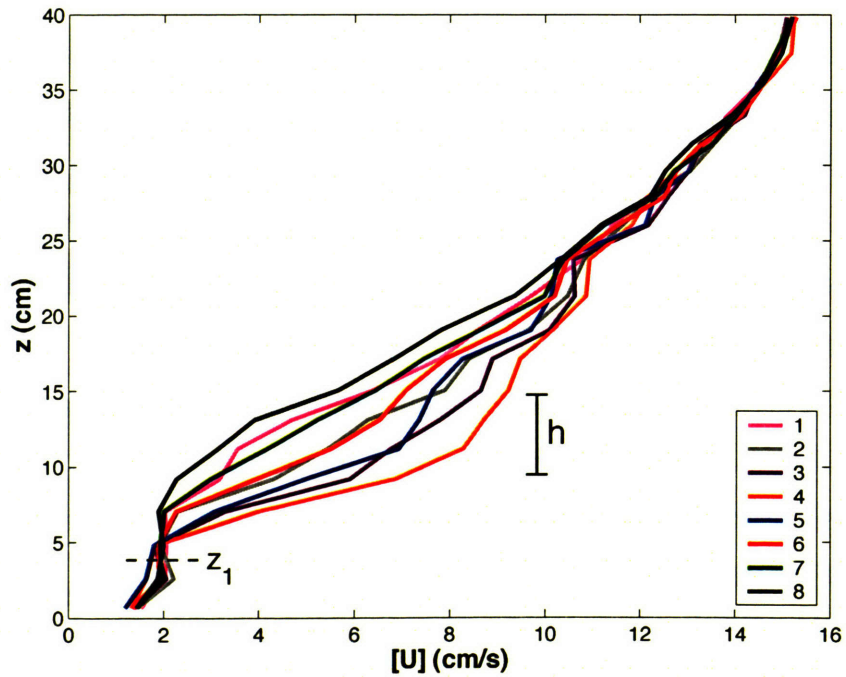
individual blades.

To best evaluate the oscillatory relationship between the flow field ($u(t), v(t), w(t)$) and the height of the colored plant ($h(t)$), the collected data was divided into eight phase bins. Each data point in $h(t)$ was classified according to its magnitude and the direction of plant motion (i.e. upwards or downwards). Then, each data point (along with the corresponding velocity information) was binned according to, firstly, the direction of plant motion and, secondly, the plant height. That is, there were four bins of descending plant height (from the maximum of 14.8 cm to the minimum of 9.4 cm) followed by four bins of ascending height. Each bin contained exactly the same number of data points. This sequence of phase bins represents one *monami* cycle, beginning from the time of maximum canopy elevation. The mean *monami* period was approximately 16 s, such that each phase bin represents approximately 2 s of this cycle. As the ADV and plant were not colocated, a lag existed between the recording of the flow field and the plant's response to that field. Firstly, Taylor's "frozen turbulence" hypothesis was invoked between the probe and the plant. Secondly, the lag was taken as 1.7 s, equal to the separation between the probe and the tips of the blades in their mean position (14 cm) divided by \bar{U} for Run F6 (8.3 cm s^{-1}). When synchronizing the video footage and ADV data, this lag was subtracted from the time of the velocity record observed in each frame. The uncertainty in the lag, due to the horizontal excursion of the blade tips, was estimated at 0.5 s, which corresponds to one-quarter of a phase bin.

The coupled oscillation of the vertical velocity profile, $[U](z)$ (where the square brackets are used to denote the intra-bin mean), and the plant height, $[h]$, is demonstrated in Figure 5-3. In Figure 5-3(a), the inverse correlation between streamwise velocity and plant height is shown. The plant took time to respond to rapidly changing flow, such that $[h]$ lags slightly behind $[U_h]$. Allowing for a plant response time of approximately 1 s yields the maximum correlation between $[h]$ and $[U_h]$. As shown in Figure 5-3(b), there is a clear, wave-like oscillation of the velocity profile. However, this oscillation does not extend throughout the shear layer, rather it is confined to a region ($5 < z < 24 \text{ cm}$) around the top of the canopy. The excursion of this oscillation



(a) The oscillation of bin-averaged values of the plant height and stream-wise velocity during the *monami* cycle. The labels indicate the height of each streamwise velocity record.



(b) The oscillation of the velocity profile, which is significant only in a confined region around the top of the canopy. The legend denotes the phase bin of each profile.

Figure 5-3: The oscillation of the velocity profile and plant height during the *monami* cycle.

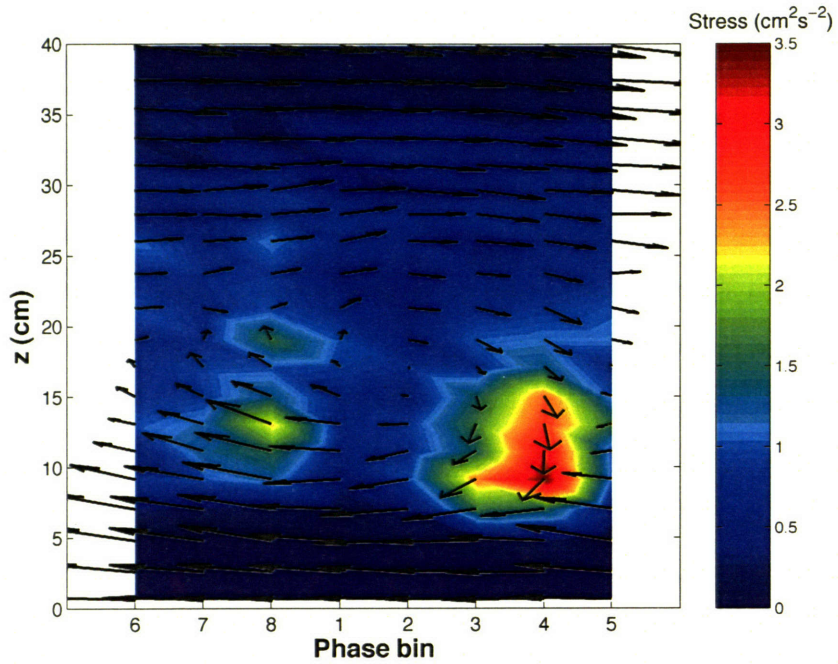
is pronounced; the velocity at $z = 9.4$ cm (the minimum plant height) varies by a factor of three through the cycle ($[U]_{\min} = 2.4 \text{ cms}^{-1}$, $[U]_{\max} = 7.0 \text{ cms}^{-1}$). Because plant height and flow velocity are inversely correlated, however, the variability in the instantaneous velocity at the top of the plant is much lower ($[U_h] = 5.2 - 7.0 \text{ cms}^{-1}$).

The fluctuation of the two-dimensional flow field ($[U], [W]$) as a function of phase bin is highlighted in Figures 5-4(a) and 5-4(b). The former is in the reference frame of \bar{U} and highlights the vortical motion in the flow, whose significance is limited to the same region as the oscillation of the velocity profile. In the latter, the mean velocity profile ($U(z), W(z)$) has been subtracted to highlight deviations from local mean velocities. In both figures, the vertical velocity has been exaggerated by a factor of 10 (since $\Delta U \gg w_{rms}$). The bin-averaged Reynolds stress is plotted in false color and shows the cycle of a strong sweep at the front of the vortex followed by a weak ejection at the rear of the vortex. That is, the most active periods of transport occur when the plant is at its minimum and maximum heights (bins 4 and 8, respectively).

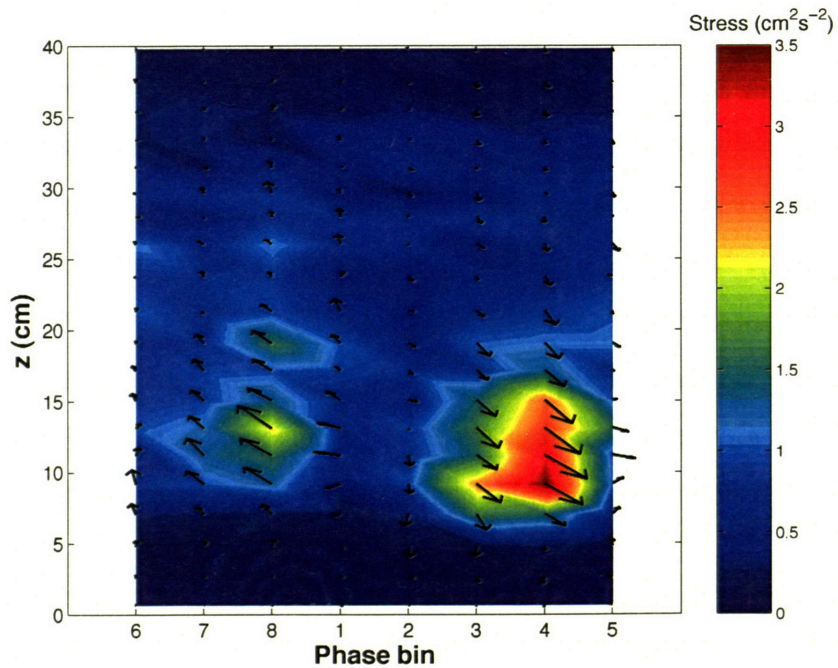
To predict vortex penetration into a flexible canopy, a detailed understanding of the dissipative effect of a waving canopy is essential. To that end, a numerical model that couples the flow and plant motion (such as in Ikeda *et al.* [30]) is required. In the derivation of the stability parameter (Ω) for rigid canopies, it was assumed that the area exposed to vertical flow was negligible with respect to that exposed to horizontal flow (refer to (2.3)). In waving canopies, this assumption is invalid, such that Ω does not take the constant value seen in rigid canopies (8.7), irrespective of how the canopy height is defined. Of specific interest, therefore, is the distribution of horizontal and vertical frontal area over the *monami* cycle. Furthermore, a greater understanding of the bulk drag coefficient of canopies that oscillate synchronously with the flow is much needed.

5.4 Conclusion

The vortex street in a vegetated shear layer creates a pronounced oscillation in the velocity profile, which in turn drives the coherent waving of flexible canopies. Relative



(a) The structure of the flow field in the reference frame of \bar{U} , the mean of the maximum and minimum shear layer velocities. The vortical motion, whose significance is limited to the same region as the velocity oscillation, is clearly demonstrated.



(b) Deviation of the bin-averaged flow field from the temporally-averaged mean profiles ($U(z), W(z)$). The strong sweep at the front of the vortex is followed by a weak ejection at the rear.

Figure 5-4: The fluctuation of the two-dimensional flow field as a function of phase bin. The bin-averaged Reynolds stress is plotted in false color.

to flows over rigid vegetation, this oscillation in canopy geometry has the effect of decreasing the turbulent stress at the top of the obstruction. To fully describe vortex penetration into a waving canopy, a model that couples the motion of the fluid and the canopy is required. As a preliminary description of this codependence, each vortex is shown to consist of a strong sweep at its front (during which the canopy is most deflected), followed by a weak ejection at its rear (when the canopy height is at a maximum).

Appendix A

Profiles of mean velocity and Reynolds stress

This appendix presents the vertical profiles of mean velocity and Reynolds stress for all runs with both rigid (Chapter 2) and flexible (Chapter 5) canopies. The velocity profiles (Figures A-1 and A-3) are nondimensionalized by subtracting the velocity at the bottom of the shear layer (U_1) and normalizing by the total shear (ΔU). Likewise, the Reynolds stress profiles (Figures A-2 and A-4) are normalized by the square of the total shear. Absolute values of U and $\overline{u'w'}$ can be extracted using the values of ΔU and U_1 tabulated in Table A.1. In all figures, the horizontal bars represent the observed lateral variability.

Table A.1: Values of ΔU and U_1 for all runs with rigid (A-K) and flexible (F1-F6) canopies.

Run	ΔU (cms ⁻¹)	U_1 (cms ⁻¹)	Run	ΔU (cms ⁻¹)	U_1 (cms ⁻¹)
A	3.2	1.3	J	3.9	0.77
B	1.3	0.50	K	1.7	0.27
C	4.9	1.7			
D	3.5	1.1	F1	2.9	0.31
E	9.5	3.5	F2	4.6	0.55
F	6.0	2.4	F3	6.2	0.72
G	3.3	1.1	F4	7.8	0.95
H	11	2.7	F5	9.7	1.4
I	7.4	1.7	F6	12	2.2

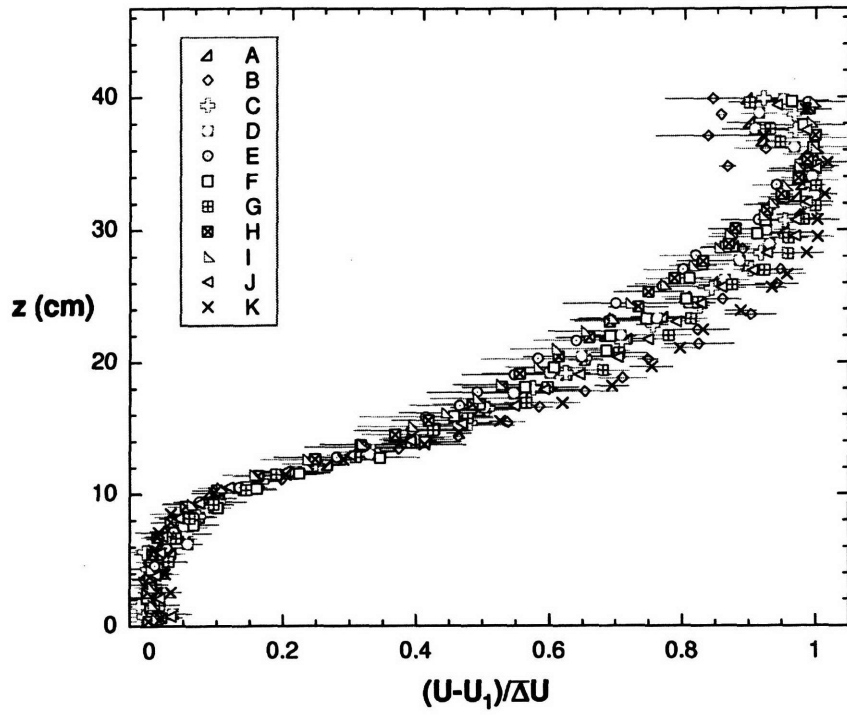


Figure A-1: Vertical profiles of mean velocity with rigid canopies.

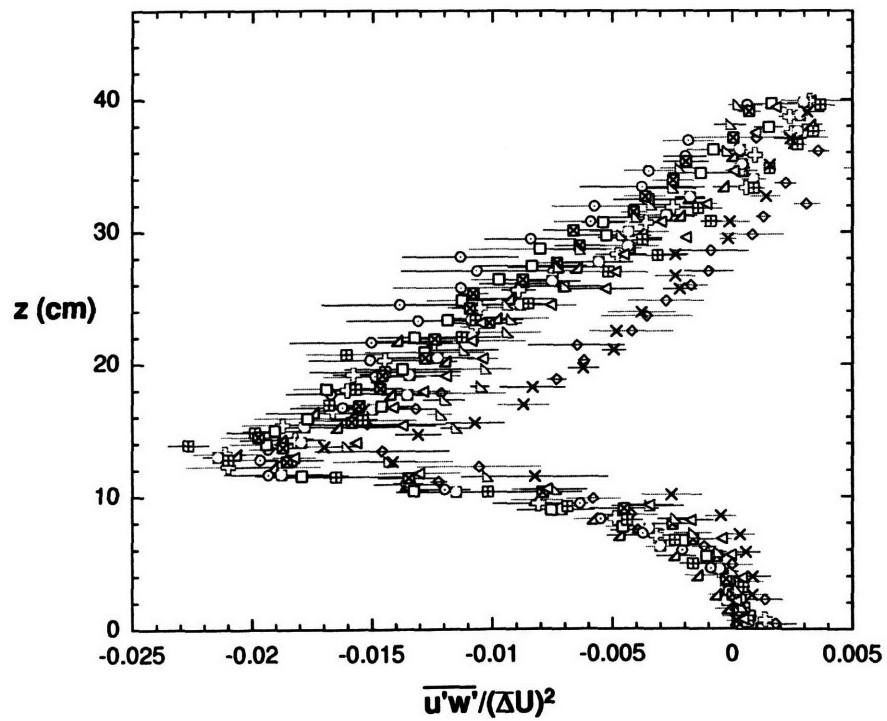


Figure A-2: Vertical profiles of Reynolds stress with rigid canopies.

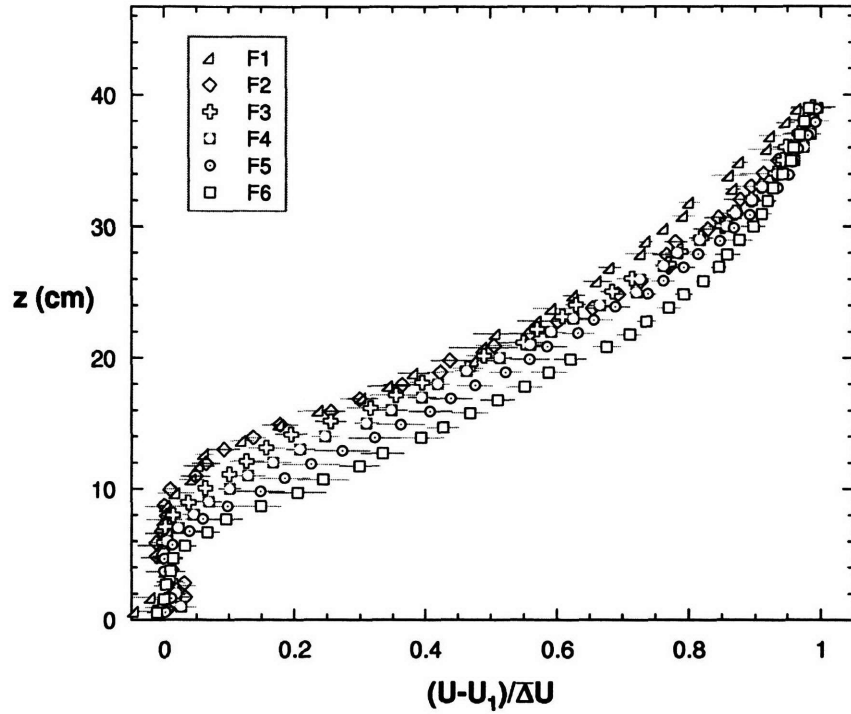


Figure A-3: Vertical profiles of mean velocity with flexible canopies.

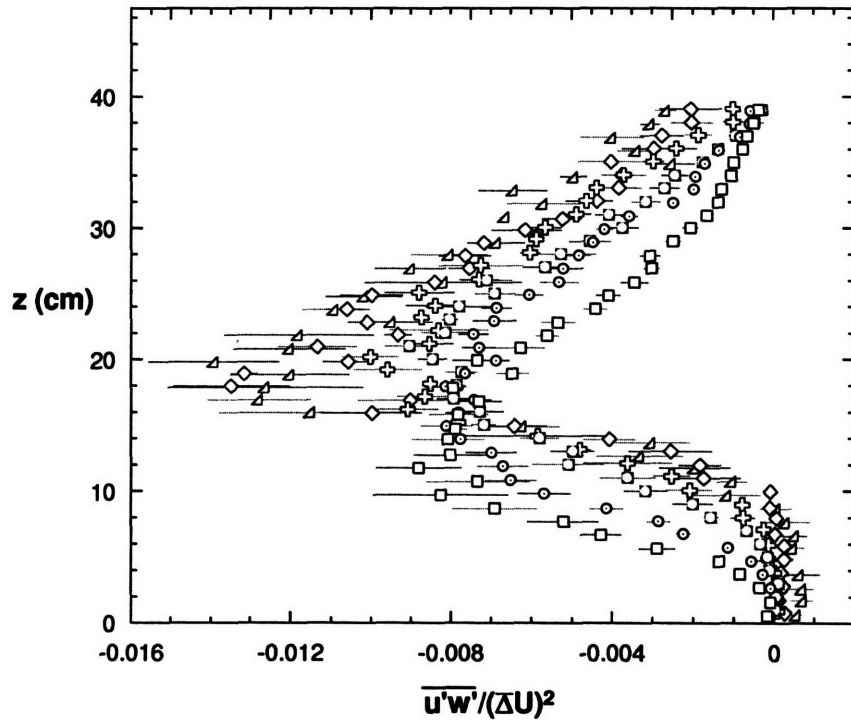


Figure A-4: Vertical profiles of Reynolds stress with flexible canopies.

Appendix B

The drag coefficient of submerged arrays as compared to individual cylinders

Figure B-1 compares the form of $\eta(z)$ for the model arrays (Figure 2-7) with those for (i) a single cylinder with an aspect ratio similar to that used in this study ($h/d = 19$, Fox and West [20]), (ii) a single cylinder with a much smaller aspect ratio ($h/d = 2$, Sin and So [60]) and (iii) the downstream cylinder of a pair in tandem ($h/d = 8$, Luo *et al.* [40]). The parameter η (refer to (2.17)) describes the effects of the free end on the drag coefficient of submerged cylinders. Specifically, η represents the ratio of the observed drag coefficient to that of an infinitely long single cylinder (for (i) and (ii)) or emergent array (for (iii) and the model arrays) at the same Reynolds number (Re_d). It is important to note that the inter-cylinder spacing used by Luo *et al.* [40] is similar to that of the model arrays of this study. In an array, $a = d/(\Delta S)^2$, where ΔS is the mean spacing between cylinders. Therefore, a spacing of $5d$ (as used by the authors) corresponds to $ad = 0.04$, which lies within the range of this study. Using this representative value of ad , and given Re_d , C_{DA} for the downstream cylinder was estimated from (2.15). As shown in Figure B-1, none of the three η profiles from the literature closely resemble that of the experimental arrays. However, there is moderate agreement with the downstream cylinder of a pair in tandem; indeed, as shown, we

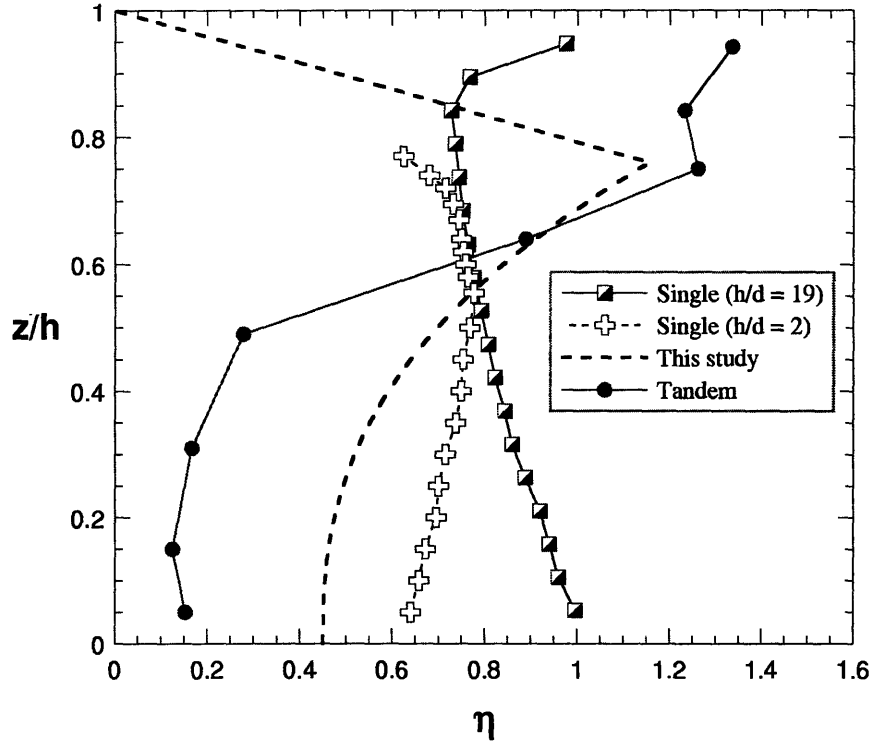


Figure B-1: The comparison between the vertical profile of η in the experimental arrays and those for (i) a single cylinder with $h/d = 19$ (Fox and West [20]), (ii) a single cylinder with $h/d = 2$ (Sin and So [60]) and (iii) the downstream cylinder of a pair in tandem with $\Delta S = 5d$ (Luo *et al.* [40]).

expect greater drag suppression on a cylinder that is immediately downstream of its nearest neighbor (unlike in a random array). As in the model arrays, η for the paired cylinder increases away from the bed, taking values greater than unity above $z/h \approx 0.7$. However, a dramatic reduction in η near the free end is not observed, this phenomenon occurring only for the cylinder with a low aspect ratio. That the array, but not the paired cylinder, exhibits strong drag suppression near the free end is indicative of the complexity of the interaction between free-end effects and the wakes of upstream cylinders.

Appendix C

Extension of hydrodynamic model outside the experimental range

In the numerical hydrodynamic model presented in §2.5, a key modeling equation is the dependence of the normalized shear ($\Delta U/U_h$) on the dimensionless plant density (ad). Although the relationship between these two parameters in this study is best described by (2.11), this expression is expected to be invalid outside the experimental range of $0.016 < ad < 0.081$. Specifically, it is expected that $\Delta U/U_h \rightarrow 0$ as $ad \rightarrow 0$, for as long as an inflectional velocity profile is maintained. This is confirmed through the analysis of data from the comparatively sparse canopies of Dunn *et al.* [13] and Poggi *et al.* [51], as shown in Figure C-1. This figure includes data for vegetated shear layers that do not penetrate to the bed (unbounded) as well as for those that do (bounded). In all cases, however, the canopy generates an inflectional velocity profile. Figure C-1 demonstrates the power relationship that exists between $\Delta U/U_h$ and ad .

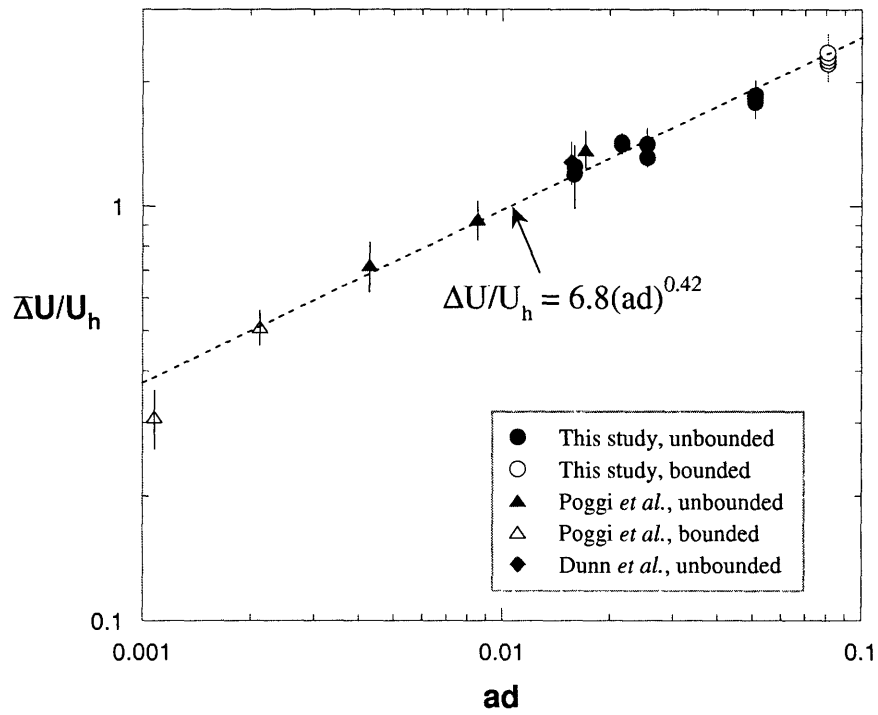


Figure C-1: The power dependence of $\Delta U/U_h$ on ad . Vertical bars represent the uncertainty in $\Delta U/U_h$, due to either lateral variability or the extrapolation of velocity profiles in the literature (Dunn *et al.* [13], Poggi *et al.* [51]).

Appendix D

Behavior of the Strouhal number along the canopy

As discussed in §3.3, the nominal Strouhal number of the vortices ($St = f_v \theta / \bar{U}$) in a fully-developed vegetated shear layer varies slightly depending on whether the canopy is rigid ($St \approx 0.037$) or flexible ($St \approx 0.032$). Furthermore, neither the vortex frequency (f_v) nor the Strouhal number remain constant as the shear layer develops along the canopy. This is shown in Figure D-1, which charts St and f_v along the flexible canopy described in §5.1 (with $H = 44$ cm and $Q = 13800$ cm³s⁻¹). At each location, the mean passage frequency of the vortices was determined through observation of the *monami*. The vortex frequency decreases along the canopy as the structures grow through either entrainment of the surrounding fluid or merging. Although vortex growth drives shear layer growth (i.e. an increase in θ), the Strouhal number also decreases along the canopy. This is consistent with the evolution of coherent structures in a shallow-water shear layer (Brian White, MIT, *pers. comm.*, 2004).

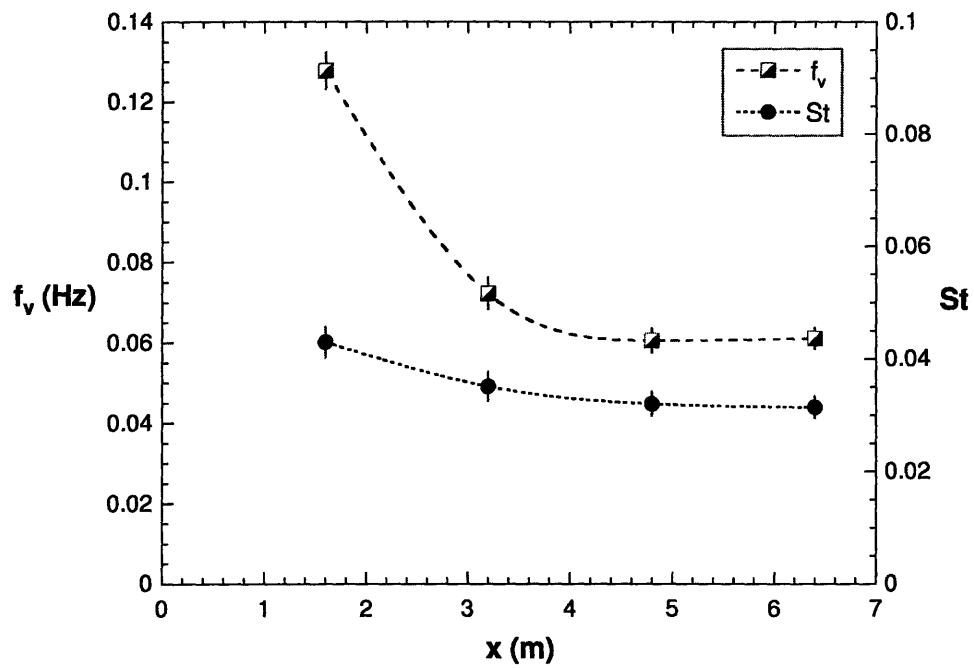


Figure D-1: The decrease in the Strouhal number (St) and vortex frequency (f_v) along the flexible canopy.

Appendix E

Concentration profiles

This appendix presents the vertical profiles of concentration at each measurement location for each run (Figures E-1–E-6). To allow comparison of the data across all flow scenarios, the concentration is normalized by the ratio of the mass injection rate (\dot{m}_i) to the flowrate (Q). As $Pe \gg 1$, \dot{m}_i is equal to the total streamwise advective mass flux at each location ($= w_f \int_0^H UCdz$), such that

$$C^* = \frac{QC}{\dot{m}_i} = \frac{C \int_0^H Udz}{\int_0^H UCdz}. \quad (\text{E.1})$$

The biggest source of uncertainty in the profiles of $C^*(z)$ arises from my estimation of steady-state conditions from a finite number of snapshots of the plume over a finite number of vortex cycles. While this uncertainty is intangible, it is worth noting that each piece of digital footage taken in these experiments captured an estimated 12–15 vortex cycles.

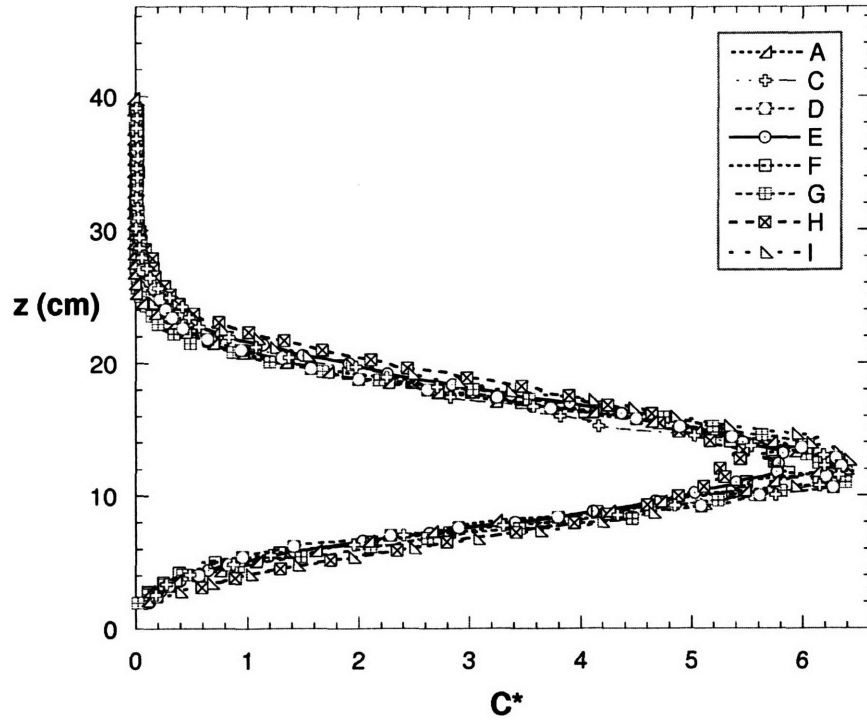


Figure E-1: Vertical profiles of C^* at measurement location 1.

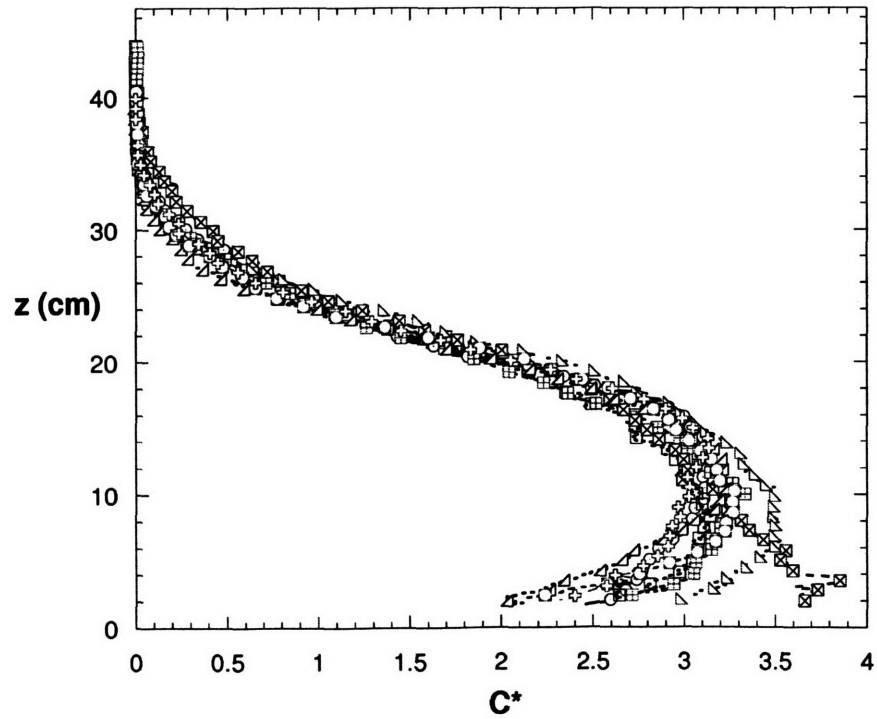


Figure E-2: Vertical profiles of C^* at measurement location 2.

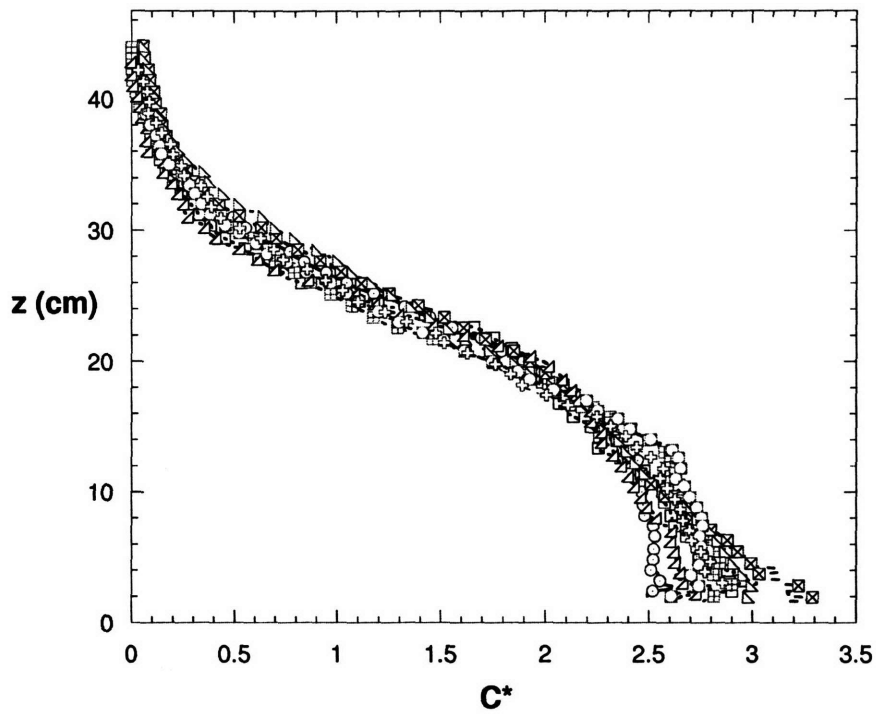


Figure E-3: Vertical profiles of C^* at measurement location 3.

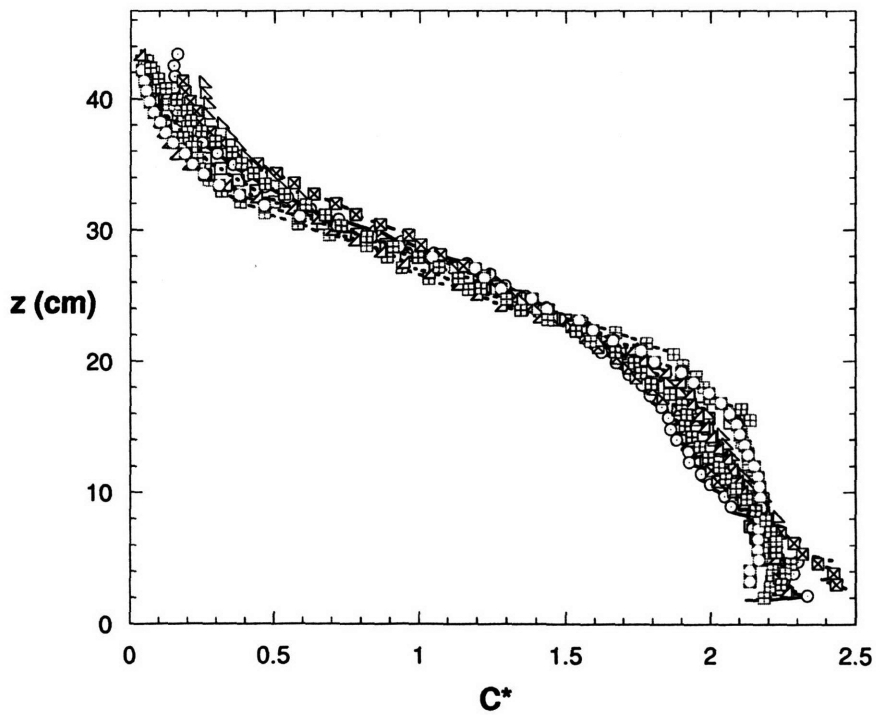


Figure E-4: Vertical profiles of C^* at measurement location 4.

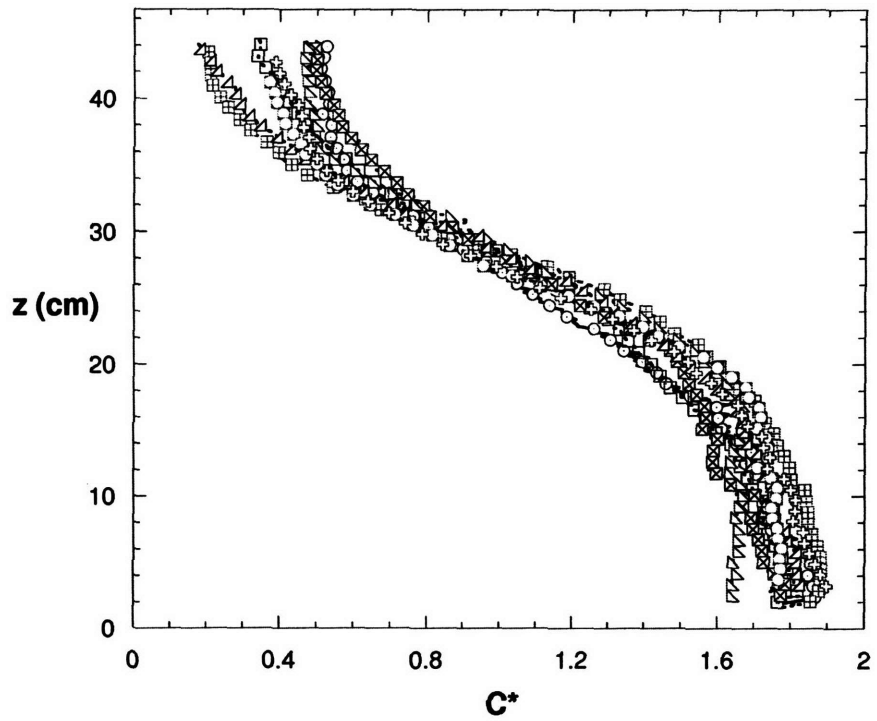


Figure E-5: Vertical profiles of C^* at measurement location 5.

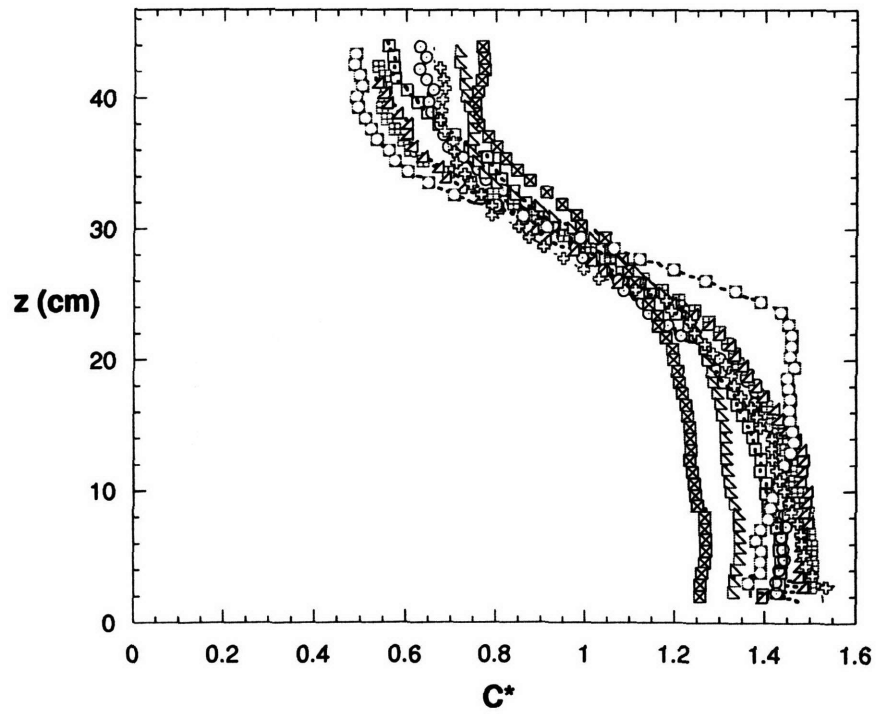


Figure E-6: Vertical profiles of C^* at measurement location 6.

Bibliography

- [1] J.D. Ackerman and A. Okubo. Reduced mixing in a marine macrophyte canopy. *Funct. Ecol.*, 7:305–309, 1993.
- [2] J.D. Ackerman. Diffusivity in a marine macrophyte canopy: Implications for submarine pollination and dispersal. *Am. J. Bot.*, 89(7):1119–1127, 2002.
- [3] A. Bokaian and F. Geoola. Wake-induced galloping of two interfering circular cylinders. *J. Fluid Mech.*, 146:383–415, 1984.
- [4] G.L. Brown and A. Roshko. On density effects and large structure in turbulent mixing layers. *J. Fluid Mech.*, 64:775–816, 1974.
- [5] Y. Brunet, J.J. Finnigan, and M.R. Raupach. A wind tunnel study of air flow in waving wheat: Single-point velocity statistics. *Bound.-Layer Meteorol.*, 70:95–132, 1994.
- [6] R.W. Burke and K.D. Stolzenbach. Free surface flow through salt marsh grass. Technical report, MIT Sea Grant, Cambridge, MA, 1983.
- [7] C.A. Butman. Larval settlement of soft-sediment invertebrates: The spatial scales of pattern explained by active habitat selection and the emerging role of hydrodynamical processes. *Oceanogr. Mar. Biol. Annu. Rev.*, 25:113–165, 1987.
- [8] M. Chandler, P. Colarusso, and R. Buschsbaum. A study of eelgrass beds in Boston Harbor and northern Massachusetts bays. Technical report, U.S. Environ. Prot. Agency, Narragansett, RI, 1996.

- [9] P.C. Chatwin. On the interpretation of some longitudinal dispersion experiments. *J. Fluid Mech.*, 48(4):689–702, 1971.
- [10] V.H. Chu and S. Babarutsi. Confinement and bed-friction effects in shallow turbulent mixing layers. *J. Hydraul. Eng.*, 114(10):1257–1274, 1988.
- [11] S. Corrsin. Limitations of gradient transport models in random walks and in turbulence. *Adv. Geophys.*, 18A:25–60, 1974.
- [12] D. Duggins, J. Eckman, and A. Sewell. Ecology of understory kelp environments. II. Effects of kelps on recruitment of benthic invertebrates. *J. Exp. Mar. Biol. Ecol.*, 143:27–45, 1990.
- [13] C. Dunn, F. Lopez, and M. Garcia. Mean flow and turbulence in a laboratory channel with simulated vegetation. Technical report, Dept. of Civil Engineering, University of Illinois at Urbana-Champaign, Urbana, IL, 1996.
- [14] J. Eckman. Hydrodynamic processes affecting benthic recruitment. *Limnol. Oceanogr.*, 28:241–257, 1983.
- [15] G.J. Edgar. The influence of plant structure on the species richness, biomass and secondary production of macrofaunal assemblages associated with Western Australian seagrass beds. *J. Exp. Mar. Biol. Ecol.*, 137:215–240, 1990.
- [16] J. Finnigan. Turbulence in plant canopies. *Annu. Rev. Fluid Mech.*, 32(1):519–571, 2000.
- [17] H.B. Fischer, E.J. List, R.C.Y. Koh, J. Imberger, and N.H. Brooks. *Mixing in inland and coastal waters*. Academic Press, San Diego, CA, 1979.
- [18] H.B. Fischer. Longitudinal dispersion and turbulent mixing in open-channel flow. *Annu. Rev. Fluid Mech.*, 5:59–78, 1973.
- [19] L. Fitzmaurice, R.H. Shaw, K.T. Paw U, and E.G. Patton. Three-dimensional scalar microfront systems in a large-eddy simulation of vegetation canopy flow. *Bound.-Layer Meteorol.*, 112:107–127, 2004.

- [20] T.A. Fox and G.S. West. Fluid-induced loading of cantilevered circular cylinders in a low-turbulence uniform flow. Part 1: Mean loading with aspect ratios in the range 4 to 30. *J. Fluid. Struct.*, 7:1–14, 1993.
- [21] M.C. Gambi, A.R.M. Nowell, and P.A. Jumars. Flume observations on flow dynamics in *Zostera marina* (eelgrass) beds. *Mar. Ecol. Prog. Ser.*, 61:159–169, 1990.
- [22] W. Gao, R.H. Shaw, and K.T. Paw U. Observation of organized structure in turbulent flow within and above a forest canopy. *Bound.-Layer Meteorol.*, 47:349–377, 1989.
- [23] M. Ghisalberti and H.M. Nepf. The limited growth of vegetated shear layers. *Water. Resour. Res.*, 40, W07502, doi:10.1029/2003WR002776, 2004.
- [24] M. Ghisalberti and H.M. Nepf. Mixing layers and coherent structures in vegetated aquatic flows. *J. Geophys. Res.*, 107(C2):3–1–3–11, 2002.
- [25] M. Ghisalberti. Coherent structures and mixing layers in vegetated aquatic flows. Master’s thesis, Department of Civil and Environmental Engineering, Massachusetts Institute of Technology, 2000.
- [26] C.M. Gramling, C.F. Harvey, and L.C. Meigs. Reactive transport in porous media: A comparison of model prediction with laboratory visualization. *Environ. Sci. Technol.*, 36:2508–2514, 2002.
- [27] R. Grizzle, F. Short, C. Newell, H. Hoven, and L. Kindblom. Hydrodynamically induced synchronous waving of seagrasses: ‘monami’ and its possible effects on larval mussel settlement. *J. Exp. Mar. Biol. Ecol.*, 206:165–177, 1996.
- [28] S. Hassid. Turbulent Schmidt number for diffusion models in the neutral boundary layer. *Atmos. Environ.*, 17(3):523–527, 1983.
- [29] S. Ikeda and M. Kanazawa. Three-dimensional organized vortices above flexible water plants. *J. Hydraul. Eng.*, 122(11):634–640, 1996.

- [30] S. Ikeda, T. Yamada, and Y. Toda. Numerical study on turbulent flow and honami in and above flexible plant canopy. *Int. J. Heat Fluid Flow*, 22:252–258, 2001.
- [31] R.H. Kadlec and R.L. Knight. *Treatment wetlands*. Lewis Publishers, Boca Raton, FL, 1996.
- [32] K. Koeltzsch. The height dependence of the turbulent Schmidt number within the boundary layer. *Atmos. Environ.*, 34:1147–1151, 2000.
- [33] M.M. Koochesfahani and P.E. Dimotakis. Mixing and chemical reactions in a turbulent liquid mixing layer. *J. Fluid Mech.*, 170:83–112, 1986.
- [34] N. Kouwen and T.E. Unny. Flexible roughness in open channels. *J. Hydraul. Div. ASCE*, 99(5):713–728, 1973.
- [35] N. Kouwen, T.E. Unny, and H.M. Hill. Flow retardance in vegetated channels. *J. Irrig. Drain. Div. ASCE*, 95(2):329–342, 1969.
- [36] B.E. Launder. Heat and mass transport. In P. Bradshaw, editor, *Topics in Applied Physics*, volume 12, pages 231–287. Springer-Verlag, 1976.
- [37] G.A. Lawrence, K.I. Ashley, N. Yonemitsu, and J.R. Ellis. Natural dispersion in a small lake. *Limnol. Oceanogr.*, 40(8):1519–1526, 1995.
- [38] F. Lopez and M. Garcia. Open-channel flow through simulated vegetation: Turbulence modeling and sediment transport. Technical report, U.S. Army Corps of Engineers, Washington, D.C., 1997.
- [39] F. Lopez and M. Garcia. Mean flow and turbulence structure of open-channel flow through non-emergent vegetation. *J. Hydraul. Eng.*, 127(5):392–402, 2001.
- [40] S.C. Luo, T.L. Gan, and Y.T. Chew. Uniform flow past one (or two in tandem) finite length circular cylinder(s). *J. Wind. Eng. Ind. Aerodyn.*, 59:69–93, 1996.
- [41] R.D. Moser and M.M. Rogers. Mixing transition and the cascade to small scales in a plane mixing layer. *Phys. Fluids A*, 3(5):1128–1134, 1991.

- [42] V.S. Neary. Numerical solution of fully developed flow with vegetative resistance. *J. Eng. Mech.*, 129(5):558–563, 2003.
- [43] H.M. Nepf and E.W. Koch. Vertical secondary flows in submersed plant-like arrays. *Limnol. Oceanogr.*, 44(4):1072–1080, 1999.
- [44] H.M. Nepf and E.R. Vivoni. Flow structure in depth-limited, vegetated flow. *J. Geophys. Res.*, 105(C12):28547–28557, 2000.
- [45] H.M. Nepf, J.A. Sullivan, and R.A. Zavistoski. A model for diffusion within emergent vegetation. *Limnol. Oceanogr.*, 42(8):1735–1745, 1997.
- [46] H.M. Nepf. Drag, turbulence, and diffusion in flow through emergent vegetation. *Water. Resour. Res.*, 35(2):479–489, 1999.
- [47] I. Nezu and H. Nakagawa. *Turbulence in open-channel flows*. A.A. Balkema, Rotterdam, the Netherlands, 1993.
- [48] A. Okubo. Ocean diffusion diagrams. *Deep-Sea Res.*, 18:789–802, 1971.
- [49] M.R. Palmer, H.M. Nepf, T.J.R. Petterson, and J.D. Ackerman. Observations of particle capture on a cylindrical collector: Implications for particle accumulation and removal in aquatic systems. *Limnol. Oceanogr.*, 49:76–85, 2004.
- [50] R.C. Phillips and E.G. Menez. Seagrasses. *Smithson. Contrib. Mar. Sci.*, 34:1–104, 1988.
- [51] D. Poggi, A. Porporato, L. Ridolfi, J.D. Albertson, and G.G. Katul. The effect of vegetation density on canopy sub-layer turbulence. *Bound.-Layer Meteorol.*, 111:565–587, 2004.
- [52] M.R. Raupach, J.J. Finnigan, and Y. Brunet. Coherent eddies and turbulence in vegetation canopies: the mixing-layer analogy. *Bound.-Layer Meteorol.*, 78:351–382, 1996.
- [53] M.M. Rogers and R.D. Moser. Direct simulation of a self-similar turbulent mixing layer. *Phys. Fluids*, 6(2), 1994.

- [54] R.A. Schincariol, E.E. Herderick, and F.W. Schwartz. On the application of image analysis to determine concentration distributions in laboratory experiments. *Journal of Contaminant Hydrology*, 12:197–215, 1993.
- [55] R.H. Shaw and I. Seginer. The dissipation of turbulence in plant canopies. In *Proceedings of the 7th Symposium of the American Meteorological Society on Turbulence and Diffusion*, pages 200–203, Boulder, CO, November 1985.
- [56] Z. Shi, J.S. Pethick, and K. Pye. Flow structure in and above the various heights of a saltmarsh canopy: A laboratory flume study. *J. Coast. Res.*, 11:1204–1209, 1995.
- [57] F.T. Short and C.A. Short. The seagrass filter: Purification of estuarine and coastal waters. In V.S. Kennedy, editor, *The Estuary as a Filter*, pages 395–413. Academic Press, Orlando, FL, 1984.
- [58] F.T. Short, W.C. Dennison, and D.G. Capone. Phosphorus-limited growth of the tropical seagrass *Syringodium filiforme* in carbonate sediments. *Mar. Ecol. Prog. Ser.*, 62:169–174, 1990.
- [59] N. Silvan, H. Vasander, and J. Laine. Vegetation is the main factor in nutrient retention in a constructed wetland buffer. *Plant Soil*, 258:179–187, 2004.
- [60] V.K. Sin and R.M.C. So. Local force measurements on finite-span cylinders in a cross-flow. *J. Fluids Eng. Trans. ASME*, 109:136–143, 1987.
- [61] D. Taylor, S. Nixon, S. Granger, and B. Buckley. Nutrient limitation and the eutrophication of coastal lagoons. *Mar. Ecol. Prog. Ser.*, 127:235–244, 1995.
- [62] A.S. Thom. Momentum absorption by vegetation. *Q. J. R. Meteorol. Soc.*, 97:414–428, 1971.
- [63] G. Voulgaris and J.H. Trowbridge. Evaluation of the acoustic Doppler velocimeter (ADV) for turbulence measurements. *J. Atmos. Ocean. Technol.*, 15:272–289, 1998.

- [64] V. Weitbrecht, W. Uijttewaal, and G.H. Jirka. 2-D particle tracking to determine transport characteristics in rivers with dead zones. In G.H. Jirka and W.S.J. Uijttewaal, editors, *Shallow Flows*, pages 477–484. A.A. Balkema Publishers, The Netherlands, 2004.
- [65] B.L. White and H.M. Nepf. Scalar transport in random cylinder arrays at moderate Reynolds number. *J. Fluid Mech.*, 487:43–79, 2003.
- [66] B.L. White, M. Ghisalberti, and H.M. Nepf. Shear layers in partially vegetated channels: Analogy to shallow water shear layers. In G.H. Jirka and W.S.J. Uijttewaal, editors, *Shallow Flows*, pages 267–273. A.A. Balkema Publishers, The Netherlands, 2004.
- [67] F.M. White. *Viscous Fluid Flow*. McGraw-Hill, New York, NY, 1974.
- [68] J.D. Wilson. A second-order closure model for flow through vegetation. *Bound.-Layer Meteorol.*, 42:371–392, 1988.
- [69] Y. Zhuang and B.D. Amiro. Pressure fluctuations during coherent motions and their effects on the budgets of turbulent kinetic energy and momentum flux within a forest canopy. *J. Appl. Meteorol.*, 33:704–711, 1994.
- [70] A. Zukauskas. Heat transfer from tubes in crossflow. *Adv. Heat Transf.*, 18:87–159, 1987.

